Université de Franche-Comté
École doctorale Carnot Pasteur

InSTEC
La Havana - Cuba

Thèse de Doctorat

présentée par

Carlos García Fernández

pour obtenir le grade de
Docteur de l'Université de Franche-Comté en Physique
et celui de
Doctor en Ciencias Físicas -Cuba

Modeling optical properties of combustion soot emitted in the Troposphere

Thèse en co-tutelle internationale dirigée par
Sylvain Picaud et Jesús Rubayo Soneira

soutenue le 26 novembre 2015

Jury :

Président :	Jean-Baptiste Renard	Directeur de Recherche CNRS, Orléans
Rapporteurs :	Luc Henrard	Professeur, Université de Namur
	Jérôme Yon	Maître de Conférences HDR, INSA de Rouen
Examinateurs :	Michel Devel	Professeur - ENSMM Besançon
	Sylvain Picaud	Directeur de Recherche CNRS, Besançon
	Jesus Rubayo Soneira	Professeur, InSTEC, La Havana
Invité	Jean-Claude Rayez	Professeur émérite, Université de Bordeaux

Contents

Acknowledgements

List of Figures

List of Tables

Abbreviations

Symbols

1 Introduction **1**
1.1 Some important areas of research in Atmospheric Chemistry . . . 2
1.1.1 Previous studies in Besançon . . . 3

2 Environmental context **7**
2.1 Impact of Aerosol on climate . . . 7
2.2 Carbonaceous aerosol . . . 11
2.2.1 Impact of air transport . . . 13
2.2.2 Soot particle formation . . . 15
2.2.3 Morphology . . . 16
2.2.4 Chemical composition . . . 21
2.2.5 Reactivity . . . 23
2.2.6 Optical properties . . . 27

3 Elements of Computational Quantum Chemistry **41**
3.1 General problem . . . 42

3.1.1 The Variation Method . . . 45
3.2 Ab initio methods . . . 47
3.2.1 General presentation . . . 47
3.2.2 The Restricted and Unrestricted Hartree-Fock Models 50
3.3 DFT . . . 52
3.3.1 Functionals . . . 54
3.4 Basis set . . . 56
3.5 Conclusion . . . 57

4 First-Principle Study of the Interaction between NO, Cl, and HCl and Large Carbonaceous Clusters Modeling the Soot Surface 61
4.1 General problem . . . 62
4.2 Computational details . . . 64
4.3 Results for the adsorption of NO on carbonaceous surfaces . . 66
4.3.1 Adsorption of NO on the Face of Perfect Carbonaceous Clusters . . . 66
4.3.2 Interaction of NO with the Edge of Carbonaceous Clusters. . . . 70
4.3.3 Discussion . . . 76
4.4 Results for the adsorption of chlorinated species on carbonaceous surfaces . . . 77
4.4.1 Adsorption of HCl on the face of a perfect carbonaceous cluster . . . 77
4.4.2 Reaction of HCl on a defective carbonaceous cluster and of Cl on a perfect carbonaceous cluster . . . 79
4.4.3 Reaction of HCl on carbonaceous cluster with a single vacancy site . . . 82
4.5 Conclusions . . . 84

5 Optical Properties of soot 91
5.1 Atmospheric interest . . . 92
5.2 Model . . . 94
5.2.1 Principle of the PDI model . . . 94
5.2.2 parametrization of carbon polarizabilities in the PDI model . . . 96
5.3 Results for fullerenes . . . 99
5.3.1 Parameters and validation . . . 99
5.3.2 Fullerenes of increasing radius . . . 101
5.4 Results for soot nanoparticles . . . 104
5.4.1 Soot nanoparticle models . . . 104
5.4.2 Mass absorption coefficient of soot nanoparticles . . . 107

5.4.3 Comparison with analytical approaches 110
5.4.4 Influence of the internal structure 112
5.5 Absorption and extinction curves of PAHs in the interstellar medium 115
5.6 Conclusions 120

6 Conclusions and perspectives **129**

A Appendix A **135**

B Appendix B **137**

Acknowledgements

I thank my supervisors, Sylvain Picaud and Jesús Rubayo Soneira for the support, the knowledge and the professional guidance given during this 3 years.

I am particularly grateful to professors Michel Devel, Marie-Therese Rayez and Jean-Claude Rayez for their efforts to give me a solid background in computational quantum chemistry. Without you, this thesis work would not have been possible. I am also very grateful to MT Rayez and JC Rayez for their hospitality during my stays in Bordeaux.

I am also thankful to Carole Héritier and Eliane Soudagne for their assistance.

I am thankful to the French Government and to the Conseil Regional de Franche-Comté for the financial support of my shared PhD studies.

And of course, I want to thank my family and my friends who have been the main motivation to achieve this result.

List of Figures

2.1 Earth's energy balance scheme [2]. 8
2.2 Estimated values of radiative forcing for major compounds supposed to participate in climate change [7]. 10
2.3 Direct and indirect effects of aerosols [7]. 11
2.4 radiative forcing of the air traffic emissions in 1992 and forecasts for 2050 [1]. 13
2.5 Schematic representation of a soot particle structure [47]. . . 15
2.6 Different stages of the soot particles formation [46]. Left, the precursor formation process, particularly PAHs; right, particle formation and agglomeration as function of time. 16
2.7 HRTEM images illustrating the nanostructure of ultra-fine soot particles [62]. Left: soot from a 4% engine power level; right: soot from an 85% engine power level. 18
2.8 Soot particles viewed in a TEM [63]. 18
2.9 soot aggregate emitted from a SaM146 engine.size distribution of primary particles emitted from a SaM146 engine [16]. 19
2.10 Mobility size distributions of particles generated from the CAST burner under different combustion conditions. The legend shows measured EC/TC ratios for these particles [67]. 20
2.11 TEM pictures of combustion particles generated under (a) C/O ratio = 0.22 and (b) C/O ratio = 0.6 [67]. 21
2.12 Raman spectrum of a soot nanoparticle [63]. 22
2.13 Carbon sp^2/sp^3 ratio of JP-8 derived soot at 4, 65, and 85% engine power levels [61]. 22
2.14 Calculating radiative transfer [19]. 27
2.15 Complex refractive index for different carbonaceous material [19]. 29

3.1 Quantum chemistry framework. 43
3.2 HFR main approximation 51
3.3 Example of Gaussian basis nomenclature. 58

4.1 Structure of the various C_nH_m carbonaceous clusters considered in the present work. 65
4.2 Optimized structures calculated for the adsorption of NO on the face of a $C_{54}H_{18}$ cluster using the 6-31G basis set and the (a) ωB97X–D or (b) LSDA functional. Both top and side views of the system are shown. N, O, C, and H atoms are represented by blue, red,gray, and white balls, respectively. . 68
4.3 Optimized structures calculated with the DFT method for the chemisorption of NO on the edge of the defective $C_{54}H_{17}$ clusters using the 6-31G basis set and the ωB97X-D functional. Binding through either a C-N (a) or a C-O (b) bond is shown. N, O, C, and H atoms are represented by blue, red, gray, and white balls, respectively. The two different adsorption sites considered in the calculations see text are indicated by numbers 1 and 2 in the left panel. 71
4.4 (a) Singly occupied MO π^* and (b) doubly occupied MO π^* of NO (the red ball is the oxygen atom). Both MOs have been obtained directly from a simple AM1 calculation 73
4.5 Optimized structures calculated for the adsorption of HCl on the face of a $C_{24}H_{12}$ cluster using the 6-311G^{++}(d,p) basis set and (a) the BHandHLYP and (b) the ωB97X–D functional 77
4.6 Mulliken analysis of the charge distributions for the a) $C_{24}H_{12}$ b) HCl and c) $C_{24}H_{12}$HCl using the 6-311G^{++}(d,p) basis set and the ωB97X–D functional 79
4.7 Optimized structures calculated with the BHandHLYP functional and the 6-311G^{++}(d,p) basis set for the chemisorption of HCl on the edge of the defective $C_{24}H_{11}$ cluster or Cl on $C_{24}H_{12}$. The two stable structures obtained for the product $C_{24}H_{12}$Cl are shown. 81
4.8 Optimized structure calculated with the BHandHLYP functional and the 6-311G^{++}(d,p) basis set for the chemisorption of HCl on a monovacancy created on a carbonaceous cluster (here, the product of the reaction HCl + $C_{79}H_{22}$ is shown) . . 84

5.1 Comparison between the experimental Loss function Im$(-1/\epsilon)$ (black curve) for a cristal of (a) C_{60} and (b) C_{70} [46] and the theoretical curves computed with three different sets of optical constants derived from graphite data; red, green and blue curves correspond to parametrizations from Ref.[40, 41, 42] and Ref.[43] (for optical and for EELS data), respectively. . . 101

5.2 Comparison between the photoabsorption cross section calculated for a C_{60} fullerene (red curve) and that reported by [50] (blue curve). Calculations have been performed by using the graphite optical constants given by Draine *et al.*[40, 41, 42]. 102
5.3 Computed mass absorption cross section (MAC) for the icosahedral C_{60},C_{240},C_{540},C_{960} and the triacontahedral C_{180}, C_{320},C_{1280} fullerenes. 103
5.4 Computed mass absorption cross section (MAC, in m^2/g) obtained when using isotropic (green curve) and anisotropic (red curve) atomic polarizabilities for (a) C_{60} and (b) C_{1280} fullerenes. 104
5.5 (a) Simplified representation of a soot aggregate made of agglomerated primary nanoparticles with, on the right hand side of the figure, a picture of the the S_{units} nanoparticle containing 2147 C atoms that is used to model a primary nanoparticle of soot in the present approach. Additional models for these primary particles, based on the S_{holes} nanoparticles, are also shown at the bottom of the figure where (b), (c) and (d) correspond to S_{holes} nanoparticles containing 2133, 2206 and 3774 C atoms, respectively. See text for the definition of the S_{units} and S_{holes} nanoparticles. 106
5.6 (a) MAC curves (in m^2/g) computed for various carbonaceous nanoparticles as a function of the wavelength (in nm). Blue, green, red and black curves correspond to S_{units} and S_{holes} with 2133, 2207, and 3774 carbon atoms, respectively. (b) Influence of the chemical composition on the S_{holes} (2133 C atoms) MAC curve : red and orange curves correspond to consideration of anisotropic (solid line) and isotropic (crosses) carbon polarizabilities in the calculations, respectively. 107
5.7 Comparison between the MAC curves (in m^2/g) computed as a function of wavelength (in nm) by using either analytical (full curves) or PDI approach (dotted curves) for various carbonaceous nanoparticles : (a) Buckyonion $C240@C540@C960@C1500$ corresponding to S_{holes} containing either 2207 or 2133 atoms (pink curves) and buckyonion $C540@C960@C1500@C2160$ corresponding to S_{holes} containing 3774 atoms (light blue curves). (b) S_{holes} containing 2207 and 2133 atoms (green and red curves, respectively), (b) S_{holes} containing 3774 atoms (black curve), and (d) S_{units} containing 2147 atoms (blue curve). . . 111

5.8 (a) Structure of the S_{holes} soot nanoparticle containing 1970 C atoms and including a small piece of graphite at its center (represented in red for clarity); (b) Example of a small piece of graphite that can been included at the center of the soot particles for the calculations of the MAC curves; (c) Example of randomly distributed small dehydrogenated Polycyclic Aromatic Hydrocarbons that can been included at the center of the soot particles for the calculations of the MAC curves. . 113
5.9 Comparison between the MAC curves (in m^2/g) computed as a function of wavelength (in nm) for two carbonaceous nanoparticles with (crosses) and without (solid lines) a small piece of graphite added at their center. Blue and red curves correspond to S_{holes} particles with 1843 and 3774 carbon atoms, respectively. 114
5.10 Extinction efficiencies of the dehydrogenated molecules [59]. . 116
5.11 Extinction efficiencies of the dehydrogenated molecules 117
5.12 Computed absorption cross section (C_{abs} 10^{-22} m^2) obtained when using a PDI method (red curve) vs the results provided by Malloci et all obtained with TD-DFT.[58] 118
5.13 Relative abundance of different hydrogenation states for three PAHs as a function of their position in an interstellar cloud: comparaison between data coming from TD-DFT and DDA/PDI calculations. 119

List of Tables

5.1 Morphological details of the soot nanoparticles considered in the calculations and the corresponding computed MAC values for 3 different wavelengths. R_{in} corresponds to the radius of the internal cavity defined by the inner layer of the nanoparticle whereas R_{out} represents the radius of the nanoparticle, defined by its outer layer. Note that C_{iso}/C represent the proportion of C atoms represented by isotropic polarizabilities *vs.* the total number of C atoms in the nanoparticle. . . . 107

5.2 Morphological details of the soot nanoparticles considered in the calculations and the corresponding computed MAC values for 3 different wavelengths. R_{in} corresponds to the radius of the internal cavity defined by the inner layer of the nanoparticle whereas R_{out} represents the radius of the nanoparticle, defined by its outer layer Note that C_{iso}/C represent the proportion of C atoms represented by isotropic polarizabilities *vs.* the total number of C atoms in the nanoparticle. 114

A.1 Required data to analyze the two reactions mentioned above and for the similar reactions involving benzene insteade of coronene (ROHF: Restricted open shell Hartree-Fock;ROHF 1/2 electron: ROHF minus the self repulsion of the two half electrons on the highest molecular orbital). 135

Abbreviations

IPCC	Intergovernmental Panel on Climate Change
BC	Black carbon
OC	Organic carbon
BrC	Brown carbon
EC	Elemental carbon
UV	Ultraviolet
IR	Infrared
PAH	Polycyclic aromatic hydrocarbons
HULIS	Humic-like substances
HIM	Helium-ion microscopy
HRTEM	High resolution transmission electron microscopy
TEM	Transmission electron microscopy
XREDS	X-ray energy dispersive spectrometry
XPS	X-ray photoelectron spectroscopy
PES	Potential energy surface
DDA	discrete dipole approximation
FDTD	Finite difference time domain
PDI	Point dipole interaction
DFT	Density functional theory
TISE	Time-Independent Schrödinger Equation
HF	Hartree-Fock
MO	Molecular orbital
LDA	Local density approximation

Symbols

μm	10^{-6}m
nm	10^{-9}m
$\mathring{A}$	10^{-10}m
$\hat{H}$	Hamiltonian operator
λ	wavelength
ϵ	electric permittivity

Chapter 1

Introduction

During the last decades growing attention has been paid to the atmosphere and atmospheric science. In the early 70s, work of Molina, Rowland, Crutzen and many others drew people's attention to environment related problems. They pointed out that human activities can have disastrous consequences on the growth of the ozone hole, and therefore on our environment. It was evidenced that a change in the human attitude to the Earth is inevitable to maintain the balance of the biosphere. The first great success of the endeavours for the protection of the atmosphere was the approval of the Montreal Protocol, which was the first international environmental treaty that banned the production of industrial chemicals reducing the ozone layer. In 1995 it was the first time the Nobel Committee recognised research into man-made impacts on the environment: The Nobel Prize of Crutzen, Molina and Rowland in chemistry showed clearly that atmospheric science should have accentuated importance in the 21st century.

Atmospheric chemistry is mainly an experimental science that generally aims at understanding the basic mechanisms in the atmosphere. Atmospheric processes, however, are difficult to study experimentally. The possibilities are quite limited because the experiments should be performed under controlled atmospheric conditions and the measurement of different chemical species should be carried out at the same time. Theoretical methods and particularly simulation techniques can thus complement and support the experimental understanding. Numerical methods have already been used successfully in numerous cases to reduce extremely complicated reaction mechanisms by finding the key processes and species. Theoretical methods enable to create models by identifying the major features and elements of the process studied. Successful predictions made by the model can support its validity. With computer simulation techniques, one can go further because it is possible to perform "experimental simulations" based on theoretical

models that can reveal a lot of details hidden from the experimentalists or not easily accessible to experiments. Atomistic simulations allow one to observe the microscopic details of the process studied and, which is at least as much or more important, make it possible to compute ensemble averages on the model system with the least possible approximation. The fact that many of the largest supercomputers in the world are dedicated to atomistic simulations in connection with drug development and protein research is a proof of the strategic importance of this area.

1.1 Some important areas of research in Atmospheric Chemistry

As much of atmospheric chemistry research deals with the reactivity in the gas phase, knowledge of reaction mechanisms has greatly increased in recent years. In particular, the analysis of the degradation of volatile organic compounds (VOCs) in the troposphere was a hot topic for many research teams. Review articles of Warmeck [1], Finlayson-Pitts and Pitts [2] and Saunders et al. [3] are an excellent summary on this topic.

However, it is now established that heterogeneous processes also contribute to the chemical evolution of many species [4] and the influence of solid and liquid particles on physical-chemistry properties of the atmosphere is the subject of many recent studies.

Among these particles, there are:

- mineral dust like silicates from the weathering of rocks, desert expanses, volcanic debris, cement industrial emissions, plaster work, urban construction, etc;

- ice particles constituting the high clouds, the liquid water droplets in clouds of lower altitude;

- organic aerosols that result predominantly from pyrolytic processes (industrial emissions, automobiles and domestic garbage incineration, fires in forests, etc ...). These organic aerosol may be primary particles resulting from aggregation of complex organic molecules of low volatility or secondary aerosols consisting of organic molecules from complex chemical and photochemical processes [5]. Carboxylic acids are among the main constituents of these secondary organic aerosol [6];

- soot is another type of solid particles resulting from incomplete combustion process in diesel engines or aircraft engines. In a general way, the constitution of soot may be likened to more or less graphitized carbon core that may be coated by organic layers[7, 8]. This organic layer may consist of several families of hydrocarbons: linear or cyclic alkanes and polycyclic aromatic hydrocarbons (PAHs), often accompanied by their nitrated and oxygenated derivates [9, 10, 11, 12, 13].

1.1.1 Previous studies in Besançon

Theoretical research work on the soot nanoparticles subject started in Besançon in 2004, as part of a collaboration with researchers of the Pablo de Olavide university, Seville. The main goal of this study was to model the influence of a hydrophilic group on the water/ graphite surface interaction by combining quantum chemical calculations [14] and classical molecular dynamics [15].

Due to the importance and interest of soot nanoparticles in the scientific community, the group of Besançon developed in the following years a set of modeling activities in four main directions :

i) the first research axis is devoted to modeling the chemical characteristics of soot particles as well as their impact on the adsorption of water molecules. The goal was to understand how a carbon particle can behave like a highly hydrophilic substrate whereas the graphitic carbon is well known to be rather hydrophobic. The methods used here are mainly those of quantum chemistry. While previous studies [14], [16] considered only perfect graphitic surfaces, Oubal et al. [18] were recently interested in modeling surfaces containing carbon vacancies (i.e., missing carbon atom in the structure of the graphitic layer) to better quantify the impact of such defects on the hydrophilic properties of these surfaces. This axis was part of the PhD works of B. Collignon (2003-2006)[9] and M. Oubal (2008-2011) [18].

ii) a second axis of research is devoted to the characterization, at the molecular level, of the interaction between soot and polycyclic aromatic hydrocarbons (PAHs) molecules. As the use of a quantum approach for such a large system (PAHs + soot particle) looked forbidden, the Besançon's team developed a simplified method (SE-D method), based on a semi-empirical potential to represent the electrostatic part of the interaction, to which is added an indispensable dispersion contribution to obtain a realistic description of the PAHs / soot interactions. This work was done in close collaboration with the ISM in Bordeaux (mainly JC and MT Rayez), in the framework of the theses of B. Collignon (2003-2006)[9] and G. Hantal (2007-2010)[20].

iii) the third axis of research is focused on modeling the effect of soot morphology on their hydrophilicity. This work was done mainly in collaboration with P. Jedlovzsky (University of Eger, Hungary) and was the subject of the theses of F. Moulin (2004-2007)[19] and G. Hantal (2007-2010) [20]. It is based both on a calculation code specifically designed to build carbon onion-like structures, such as those observed experimentally in soot particles [Delhaye, 2007] and the use of the Monte Carlo method in the grand canonical ensemble to simulate the influence of these structures on the trapping of water molecules.

iv) finally, a fourth axis is devoted to the calculation of the optical properties of primary soot nanoparticles considering their atomic characteristics. This work aims at linking the observable optical properties of soot to their intrinsic properties such as chemical composition, porosity, roughness. This work is done in collaboration with M. Devel of the Femto-ST Institute (Besançon) and has been initiated during the PhD of F. Moulin (2004-2007)[19].

My own work is clearly a continuation of the previous works done in Besançon. It is thus partly devoted to the modeling of the electromagnetic properties of soot nanoparticles on the basis of the preliminary works of F. Moulin, M.R. Vanacharla, and R. Langlet. My work initially aimed at focusing on the optical properties of soot particles modified by adsorption of atmospheric species. It thus includes a part devoted to quantum chemistry, in order to characterize the adsorption properties of some relevant atmospheric gases and the subsequent modifications of the soot surface. However, as it will be explained in the manuscript, calculating the optical properties of such modified carbonaceous particles is facing the problem of the knowledge of the atomic polarizabilities and of their dependence with frequency (dynamic polarizabilities) for atoms other than the carbon atoms. Although we have explored some ways for overcoming this problem (not detailed in this manuscript), the work done here is finally focusing on pure carbon particles, only. The simulation of the electromagnetic properties of these particles have been done in the framework of a close collaboration with Michel Devel, who has written the "polarscat" code that I have used for the present calculations. This code is based on a modification of the usual implementation of the DDA method, to take into account the atomic structure of the particles considered in the calculations. My work is also partly devoted to the characterization of the ageing of soot nanoparticles by means of quantum calculations, devoted here to the adsorption of chlorinated species. Moreover, it is mandatory to mention that my PhD work has been done in the framework of a shared supervision between S. Picaud at Besançon and J. Rubayo-Soneira at La Havana. As a consequence, I spent only part of the three PhD years at UTINAM (24 months), the other 12 months being devoted to my teaching duties at InSTEC (Cuba).

Bibliography

[1] P. Warmeck, Chemistry of the natural atmosphere, International Geophysics Series Vol 41, Academic, New York, 1988.

[2] B.J. Finlayson-Pitts, J.N. Pitts Jr., Chemistry of the Upper and Lower atmosphere, Academic, San Diego, 2000.

[3] S. Saunders, M. Jenkin, R. Derwent, M. Pilling, Atmos. Chem. Phys. 3 (2003) 161.

[4] J.N. Crowley, M. Ammann, R.A. Cox, R.G. Hynes, M.E. Jenkin, A. Mellouki, M.J. Rossi, J. Troe, T.J. Wallington, Atmos. Chem. Phys. 10 (2010) 9059.

[5] S.P. Sander et al., JPL publication 10-6, Jet Propulsion Laboratory, Pasadena, 2011

[6] H. Satsumabayashi, H. Kurita, Y. Yokouchi, H. Ueda, Atmos. Environ.(1990), 24,1443.

[7] Z. Krivacsy, Z. Sarvari, D. Temesi, S. Nyeki, S. Kleefeld, S.G. Jennings, Atmos. Environ. 35 (2001) 6231

[8] J. Viidanoja, M. Sillanpaa, J. Laakia, V. Kerminen, R. Hillano, P. Aarno, T. Kosentalo, Atmos. Environ. 36 (2002) 1943.

[9] C. J. Halsall, P.J. Coleman, K.C. Jones, Environ. Sci. Technol. 28 (1994) 2380.

[10] E. Leotz-Gartziandia, These, Universite Paris VII, 1998.

[11] E. Leotz-Gartziandia, V. Tatry, P. Carlier, Polycyclic Aromatic Compounds,20 (2000) 245.

[12] M. Odabasi, N. Vardar, A. Sofuoglu, Y. Tasdemir, T.M. Holsen, The Science of the Total Environment, 227 (1999) 57

[13] Y. Liu, L. Zhu, X. Shen, Environ. Sci. Technol. 35 (2001) 840

[14] S. Hamad, J.A. Mejias, S. Lago, S. Picaud and P.N.M. Hoang, J. Phys. Chem. B, 108 (2004) 5405

[15] S. Picaud, P.N.M. Hoang, S. Hamad, J.A. Mejias, and S. Lago, J. Phys. Chem., B 108 (2008) 5410.

[16] B. Collignon, P.N.M. Hoang, S. Picaud, D. Liotard, M.T. Rayez, J.C. Rayez, J. Mol. Struct. Theochem., 772 (2006) 1

[17] B. Collignon, Modélisation à l'échelle moléculaire des suies émises par les avions et de leur interaction avec les molécules environnantes. PhD Thesis, Universite de Franche-Comte, 2006

[18] M.Oubal, Etude théorique de la réactivité des particules de suie émises par les avions. PhD Thesis, Universite de Franche-Comte, 2011

[19] F. Moulin, Modélisation morphologique des suies émises par les avions. PhD Thesis, Universite de Franche-Comte, 2007

[20] G. Hantal, Modélisation de l'adsorption sur des particules solides dans l'atmosphère. PhD Thesis, Universite de Franche-Comte, 2010

Chapter 2

Environmental context

Atmospheric aerosols consist of solid bodies suspended in air. These solid bodies have a radius changing from a few nanometers to hundreds of micrometers. Among them, soot particles are of the major representatives of fine atmospheric aerosols that are considered to have a radius less than 1 μm. Such fine aerosols originate almost exclusively from condensation of precursor gases. Besides soot particles, organic and sulfate aerosol (H_2 SO_4 H_2O) particles are also important components. First, aerosols manifest themselves basically in scattering solar radiation, which causes the reduction of visibility. Another impact is the perturbation of climate, which arises by changing the albedo of the atmosphere. The impacts arising from scattering/absorbing solar radiation are usually reflected in the so called 'radiative forcing' effect.

2.1 Impact of Aerosol on climate

It now seems certain that human activities contribute significantly to climate change. Indeed, in recent years, meteorological data and calculations clearly show that human activity is the main factor of the global warming observed on the surface of the Earth and oceans since the end of the 19^{th} century. The estimate of this warming is $(0.6 \pm 0.2)^\circ$ C for the twentieth century (Third Report of the IPCC 2001 [1, 2]).

Regarding our future, the climate community appears virtually unanimous about the continuation of this warming trend. However, given the complexity of climate systems and the lack of knowledge in some areas of physical chemistry of the atmosphere, uncertainties remain high with regard to the magnitude of the global warming. Thus, a more precise quantification of the

human activities effects on climate appears more necessary than ever. For example, the emission of an increasing amount of aerosols in the atmosphere can lead to major changes in our climate, especially increasing the global average temperature of the Earth's surface.

Globally, the climate is determined by the Earths energy balance or radiation balance [3]. On average, the Earth + atmosphere system loses energy by radiation into space almost equally as it receives energy from the sun, which leads to the conservation of the Earth's surface temperature. Therefore, reflection, absorption and emission properties of Earth play a crucial role in the energy balance.

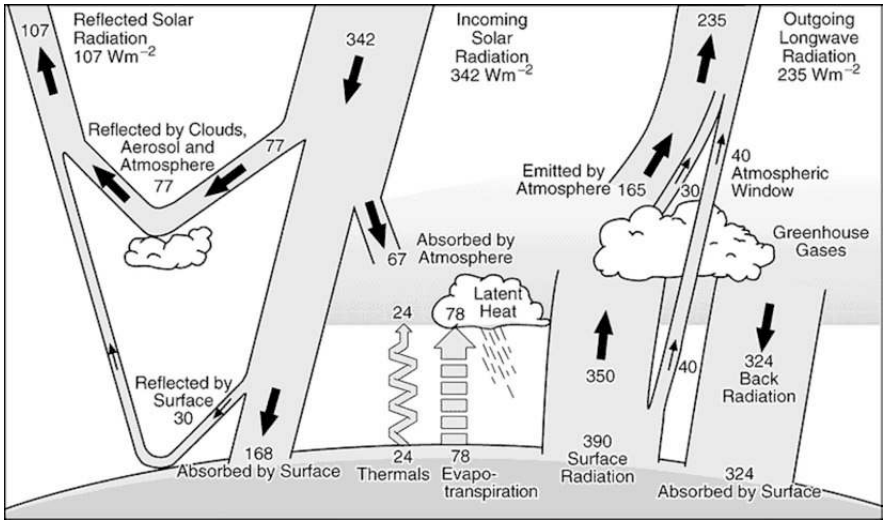


Figure 2.1: Earth's energy balance scheme [2].

In general (see Fig 2.1), the solar energy flow received by the Earth System + atmosphere (on top of the atmosphere) has an averaged value of 342 $W.m^{-2}$. Part of this energy is directly reflected by the atmosphere (77 $W.m^{-2}$), particularly by clouds and aerosols, and the Earth's surface (30 $W.m^{-2}$). This fraction of solar energy that is directly reflected back into space by the Earth is the albedo (ratio of the solar energy reflected on the incident solar energy) from Earth and it represents about 30% of the received energy. In adition, about 67 $W.m^{-2}$ are directly absorbed by the atmosphere, especially in the ultraviolet range. For example, stratospheric ozone absorbs about 3 % of the solar energy flow. The remaining fraction of solar energy (about 168 $W.m^{-2}$) is absorbed by the Earth's surface.

In return, Earth's surface emits radiation whose total energy corresponds to a flux of about 492 $W.m^{-2}$. As an important part (390 $W.m^{-2}$) is in the infrared range (above 10 μm), the corresponding wavelengths are absorbed

by the gases in the atmosphere (in particular H_2O, CO_2, CH_4 ...) which then emit radiation in all directions. Then, part of this energy re-emitted by the Earth is trapped as heat in the atmosphere, some is reflected back to the space and the remaining part is retransmitted to the ground. This latter contribution represents a flow of energy of about 324 $W.m^{-2}$. At the end, losses and energy gains offset each other, at the Earth's surface and the atmosphere even if there are difference between, for example, the north and the south poles (convection effect).

If we admit that the Earth behaves as a black body and using the Stefan's law, the flow of energy transmitted to the ground (390 $W.m^{-2}$) corresponds to an Earth's average temperature of about 288 K. However, the amount of energy that actually receive the Earth + atmosphere system is approximately 240 $W.m^{-2}$ that only corresponds to a temperature of about 255 K. The 33 K difference is commonly called greenhouse effect [3, 4].

Certain phenomena can alter the energy balance as, for instance, a major volcanic eruption which would result in the production of a huge amount of dust increasing the Earth's albedo. Thus, since the beginning of the industrial age, increasing the amount of CO_2 in the atmosphere has been correlated with a significant increase of the average temperature at Earth's surface, leading to the famous global warming phenomenon. However, an increase in sea temperature also affects the solubility of gases, and such feedback effect makes exact predictions on the influence of anthropogenic emissions on the global warming very difficult to establish.

In general, these changes of the energy balance correspond to the radiative forcing of the climate system [5, 6]. Radiative forcing is a quantity measured or calculated in $W.m^{-2}$ that results in either a warming (positive forcing) or cooling (negative forcing) of the Earth's surface. However, as previously mentioned, this radiative forcing is often difficult to quantify because of the intrication of many effects, complicated by the wide variety of molecules involved in atmospheric processes.

Figure 2.2 shows the estimated radiative forcing values for the main compounds that are supposed to participate in climate change [7]. As we can see, because of their positive radiative forcing, greenhouse gases such as carbon dioxide CO_2, methane CH_4, or nitrous oxide N_2O are related to an increase in temperature.

Aerosols are another major cause of radiative forcing as well. Their sizes, concentrations and chemical compositions are however highly variable. In addition, some aerosols are emitted directly into the atmosphere while others are the result of complex physico-chemical evolution of other compounds in the atmosphere. Thus, the influence of aerosols on the radiative forcing

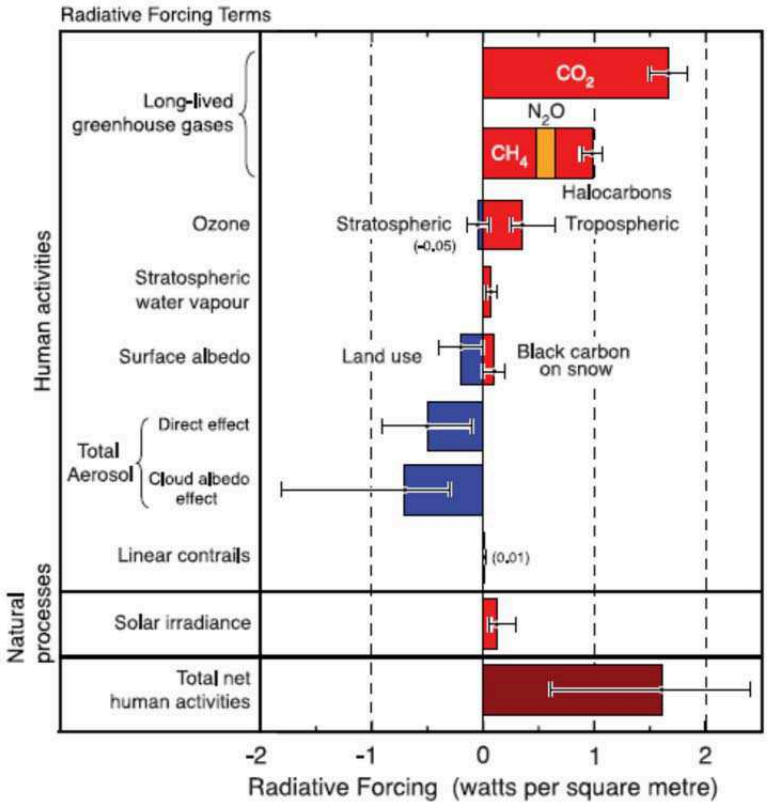


Figure 2.2: Estimated values of radiative forcing for major compounds supposed to participate in climate change [7].

is hard to evaluate and, although the radiative forcing due to aerosols is considered on average as negative (fig 2.2), large uncertainties are still remaining.

There is two types of aerosol effects on radiative forcing: the direct and the indirect effects. Direct effects are the mechanisms by which aerosols absorb and scatter light. Optical properties like single scattering albedo, extinction and scattering phase function coefficient computed as a function of the wavelengths, relative humidity, geographical distributions and vertical and horizontal concentrations are key parameters to determine these effects [6, 8, 9].

The indirect effect arises from the mechanisms by which aerosols modify the microphysical properties of clouds. These properties are related to the efficiency of aerosols to act as nuclei in the condensation processes of water vapor. The nucleating properties depend on the size, the chemical composition of aerosols, and on their surrounding [9]. Microphysical properties have,

for example, an influence on the size and number of water droplets. This effect is called 'first indirect effect' [6], cloud albedo effect [10], or Twomey effect [11]. The effects concerning cloud height, or lifetime are called second indirect effect [6] cloud 'lifetime effect' [10] or 'Albrecht effect' [12]. These effects are summarized in Figure 2.3.

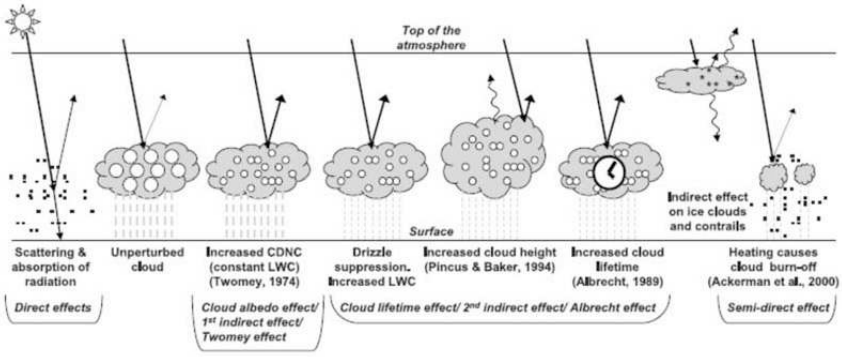


Figure 2.3: Direct and indirect effects of aerosols [7].

2.2 Carbonaceous aerosol

Recent studies have shown that endothelial cells treated with flame generated carbon nanoparticles exhibit increased tendency of cell death [13] and that toxicity of flame soot appears to increase with oxidation in the ambient air [14]. Thus, there is a strong impact of soot on the air quality [15, 16] and their sub-micrometer size is now a matter of questions regarding their effect on human health [17, 18].

Moreover, the radiative forcing due to carbonaceous particles, particularly those emitted by aircraft, has been the subject of many discussions. However, many uncertainties remain to quantify its direct or indirect effects and the term 'soot' is used for a wide range of light absorbing carbon [19] having different morphologies, chemical composition and optical properties as results of a wide variety of production sources.

Thus, despite according to chemists truly elemental carbon has five main ordered forms, namely graphite, diamond, nanotubes, graphene, and C60-like (buckminsterfullerene or buckyballs), there exists in the literature a certain variability in the definition of Strongly Absorbing Carbon particles, which leads to confusing terminology and thereby some difficulties in comparing different studies.

Graphite consists of sp^2 bonded carbon in planar layers, and diamond contains sp^3 bonded carbon in crystalline form. In contrast, many different names are used to represent carbonaceous systems that exhibits extensive arrays of sp^2 and sp^3 bonds: elemental carbon, graphitic carbon, black carbon, amorphous carbon, organic carbon, brown carbon, etc. Among those, black carbon (BC) is the most strongly absorbing aerosol material in the atmosphere [19]. Most of aerosol BC is anthropogenic in origin and originates from combustion of fossil fuel, biogenic fuel, and biomass burning [20, 21].

In recent years, there has been increasing evidence that organic carbon (OC) can also have appreciable light absorption, especially in the UV region [22, 23]. This light absorbing OC is commonly referred to as brown carbon (BrC) because the stronger absorption toward shorter wavelengths gives rise to brownish colors [24, 25].

Aerosol BrC originates from various sources such as biomass burning [26] , smoldering combustion [27], and natural biogenic emissions [28]. BrC can be also formed as secondary aerosol from heterogeneous reactions, e.g., of gaseous isoprene on acidic particles [29].

BrC is thought to have molecular structures similar to polycyclic aromatic hydrocarbons (PAH) or humic-like substances (HULIS) but there is still a high degree of uncertainty regarding its exact chemical composition and origin [30]. Compared to graphite-like BC, BrC has a lower degree of graphitization which means that its optical gap between filled valence band and unfilled conduction band is larger, and the absorption is shifted to shorter wavelengths. However, full characterizations incorporating chemical and physical analysis are scarce. Particularly, there is still insufficient data on optical properties of BrC compared to that of BC.

Indeed, in many studies, soot or black carbon terms are used interchangeably to describe a black substance produced from combustion, composed almost exclusively of carbon and having a morphology and a chemical composition resulting from the aggregation of primary particles. It is made of graphitic layers with a very small percentage of other species [31, 32, 33, 34, 35].

Soot when emitted by aircraft also have an impact on the global radiative forcing by promoting the formation of condensation trails (contrails) that may evolve in artificial cirrus clouds [36]. Uncertainties about the properties and amounts of combustion soot continue to impact our understanding of its climate effects [37]. Estimates of different radiative forcings associated with aviation related compounds are given in Figure 2.4 for the years 1992 and 2050.

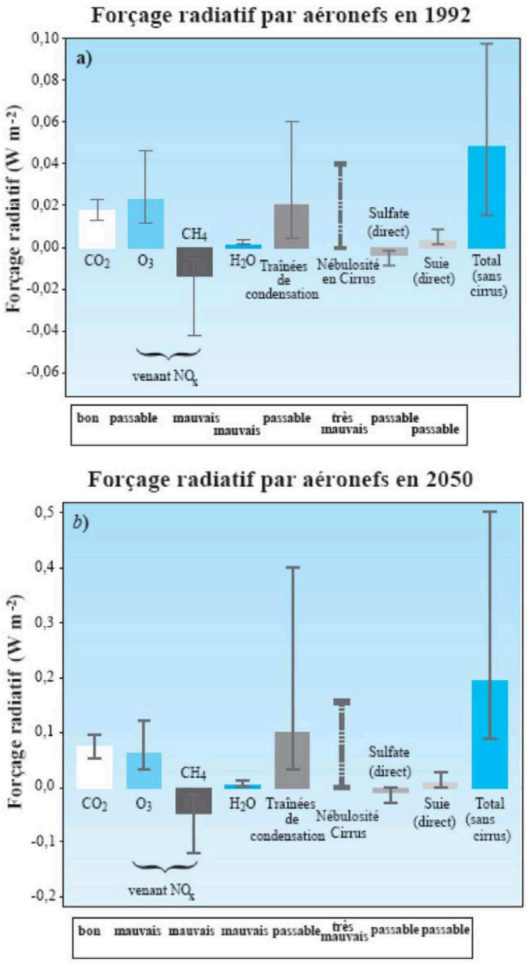


Figure 2.4: radiative forcing of the air traffic emissions in 1992 and forecasts for 2050 [1].

Nevertheless, one can see in Figure 2.2 that the direct influence of aircraft contrails (0.01 $W.m^{-2}$) seems negligible compared to other effects, but as we will see later the indirect effects of these contrails are very poorly estimated.

2.2.1 Impact of air transport

Concerns about the impact of air traffic are directly related to released compounds by aircraft. This is particularly true for commercial aircraft that fly in areas between high troposphere and lower stratosphere where they are the single direct source of pollutants. Indeed, kerosene is a mixture of sulfur containing hydrocarbons and alkanes with chemical formula C_nH_{2n+2}, and

n ranging from 10 to 14. Its combustion in the aircraft engine produce water vapour and other air pollutants such as CO_2, NO_x, SO_x, CO and also soot.

Greenhouse gases like CO_2 and H_2O absorb IR radiation and contribute to global warming. Some gases such as NO_x can destroy a fraction of stratospheric ozone, reducing the UV protection and increasing concentration of ground-level ozone, which increases the IR absorption and promote global warming. SO_x is a source of H_2SO_4 (the cause of acid rain) and can alter the radiative properties of cirrus (cooling).

Natural cirrus clouds are optically almost transparent to UV-visible light allowing the passage of most of the UV light towards the ground. However, they absorb efficiently the infrared radiation emitted by the Earth and re-emit it in all directions. Then, some of these radiations is therefore sent to the ground. The absorption of infrared radiation seems favored in the case of fine cirrus contrails promoting a positive radiative forcing. However, there are still relatively few studies that have finally quantized the impact of this artificial cloud cover [38, 39, 40, 41].

The study of Sausen et al. (2005) gives an estimate of the direct radiative forcing due to condensation trails emitted by the air traffic of the order of 0.01 $W.m^{-2}$ [41]. However, this estimate does not take into account the effect of cirrus induced by contrails. Other authors estimate that the radiative forcing of cirrus cloudiness induced by aircraft contrails ranges from 0 to 0.04 $W.m^{-2}$ [1]. Uncertainty in these estimates introduce significant uncertainties in modeling and determination of global values. Moreover, contrails can mix with natural clouds making it very difficult to differentiate between the effects induced by artificial cirrus and those from natural cirrus.

The estimate of the ratio between cloudiness induced by air traffic and contrails and natural clouds varies from 1.8 to over 10 [42, 43], which gives an idea of the uncertainties in the measurement of the impact of artificial cirrus.

It should be noted that tentative accurate measurements of the real impact of artificial cirrus have been made by comparing the induced effects in air corridors to those observed outside [44, 39]. Thus, it was shown that the surface of sky covered by contrails is estimated to be 8% of that covered by natural clouds in the main air lanes. In the middle latitudes of the northern hemisphere, the radiative forcing of these contrails was then estimated at 0.1 $W.m^{-2}$.

2.2.2 Soot particle formation

Soot nanoparticles are mainly composed of carbon atoms arising from the combustion of fuel at high temperature under conditions where the amount of oxygen is insufficient to convert all the fuel into CO_2 and H_2O [19]. It is accepted that the soot particle formation process begins with a gas-solid phase transition corresponding to the formation of soot precursors. Thus, radicals like C_2, C_3, C_2H, C_4H_2 ... who fit together to build long linear carbon chains, lead to the formation of polycyclic aromatic hydrocarbons (PAH compounds carbon-based and hydrogen having several benzene rings) by addition reactions of small molecules and in particular the addition of acetylene (C_2H_2) [45, 46].

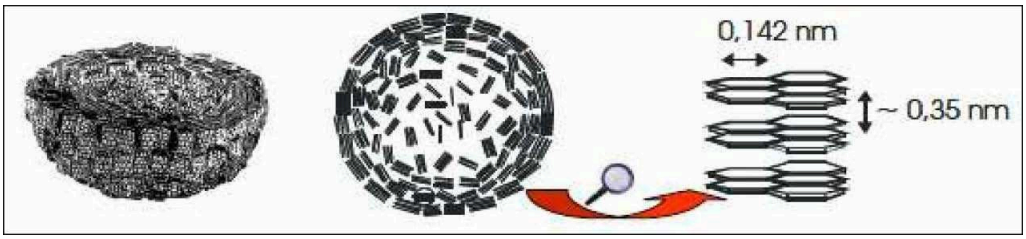


Figure 2.5: Schematic representation of a soot particle structure [47].

The continued growth of these PAHs allow the appearance of the primary soot particles whose size is typically of the order of tens of nm. Then, because of their high reactivity, due to chemical and structural defects, they can evolve by attachment of gaseous species, to form particles of larger sizes (up to about 50 nm) [48, 49]. These elementary carbon nanoparticles issued from combustion processes are constituted by large aromatic structures (sheets of the order of 2 to 4 nm), stacked together on concentric layers separated by distances greater than the interlayer distance in graphite (between 3.4 and 3.8 Å). (see an illustration of this structure on Fig. 2.5).

These elementary particles can then be agglomerated by coagulation physical processes that result in aggregates of sizes up to more than 50 microns according to transmission electron microscopy measurements [46, 50].

To summarize, the soot formation process is illustrated in Figure 2.6.

However, it is important to note that the soot particle formation process is strongly dependent on the combustion conditions, the fuel type and the shape of the combustion chamber. Thus, the structural properties of the soot nanoparticles are related with the combustion mode as well as with the fuel composition.

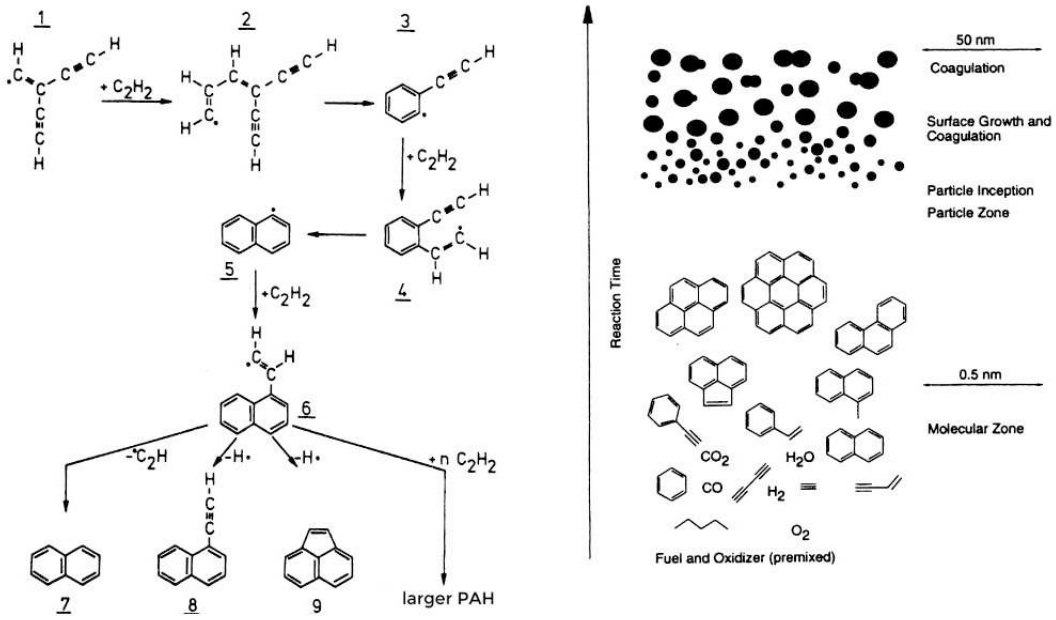


Figure 2.6: Different stages of the soot particles formation [46]. Left, the precursor formation process, particularly PAHs; right, particle formation and agglomeration as function of time.

2.2.3 Morphology

The first difficulty when seeking to experimentally characterize the soot emitted by aircraft is to collect them in different production conditions (different phases of flight and power regime of the aircraft engine). This fact has led many groups to use soot from combustion (e.g. soot flames) as a first approximation to model the real soot nanoparticles. However, even in the case of laboratory production, kerosene is an expensive fuel and other hydrocarbon mixtures are frequently used to represent the full range of products that may arise during the combustion of kerosene.

These different soot production techniques from different fuels obviously lead to a large variety of results on the atomic properties, size, porosity, or even chemical composition (percentage of oxygen atoms, presence or absence of sulfur atoms and type of oxygenated groups present in the soot)[51, 52, 53, 54].

Furthermore, it has been shown by Delhaye et al.[55] that the way of collecting the soot, the media on which they are fixed before analysis, and the technique used to analyze it (scanning electron or transmission electron microscopies) also have a significant influence on the measured properties of

the soot. In particular, the apparent size of the primary particles constituting the soot seems strongly dependent on the microscopy technique used [55].

Information about morphology and chemical composition of nascent soot is critical to a description of the surface area and the kinetics of surface reactions [56, 57]. Recently, Helium-ion microscopy (HIM) was used to probe the morphological and size evolution of nascent soot in ethylene flames. Compared to electron microscopy, HIM allows for better contrast and surface sensitivity, and soot particles as small as 2 nm could be recognized [58]. The results shows that soot collected in a burner-stabilized ethylene flame exhibits quite irregular shapes and structures even for those just a few nanometers in size, suggesting that some degree of aggregation starts as soon as soot nucleates, as predicted by earlier simulation [59]. The images taken for soot collected from different heights (i.e. growth times) were analyzed with respect to their geometrical parameters, specifically circularity, sphericity, and fractal dimension. While variations of these parameters over the collected samples were not large, comparison with representative real particle shapes and illustrative simple geometrical shapes indicates that nascent particles in these flames have no well defined shape in agreement with a conceptual assumption that particles are not spherical at their origin, but that lesser-defined structures arise at all phases of the nucleation and early growth process [60].

Moreover, the characteristics of soot from aircraft engines depend on the manufacturing process [61]. For example, particle nanostructure observed in the high resolution electron microscopy (HRTEM) images (Fig. 2.7) suggests particle composition high in organic carbon at low engine power level (4%). The short disconnected and randomly oriented lamellae (where recognizable) are of a size consistent with few (2-4) ring PAHs. The high proportion of edge sites suggests termination under atmospheric exposure by H-atoms.

In contrast the particles produced at high power (85%) demonstrate graphitic structure with lamellae of extended length and order. Both features are characteristics of a carbonaceous particle that contain mainly elemental carbon, consistent with the bulk elemental analysis as reported by Corporan et al. [62].

Another experimental result obtained after the analysis of a kerosene flame indicates the presence of primary particles with a diameter of 30 to 50 nm [63]. In this case, these carbon particles have an onion-like structure with graphitic nanocrystals stacked on successive layers [63, 64, 65] (fig 2.5).

In 2007, D. Delhaye developed a technique to collect soot by collisions behind a commercial aircraft engine, which has been tested with two types

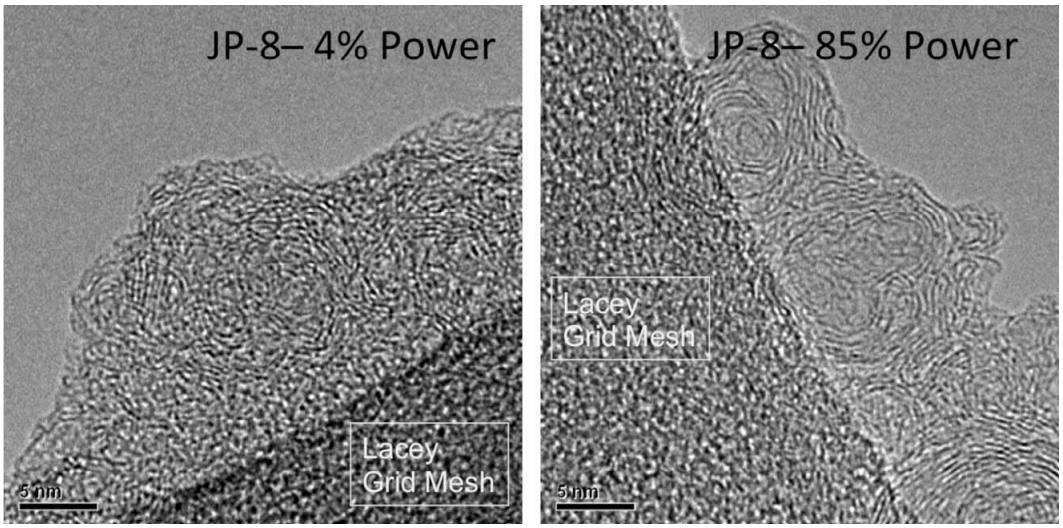


Figure 2.7: HRTEM images illustrating the nanostructure of ultra-fine soot particles [62]. Left: soot from a 4% engine power level; right: soot from an 85% engine power level.

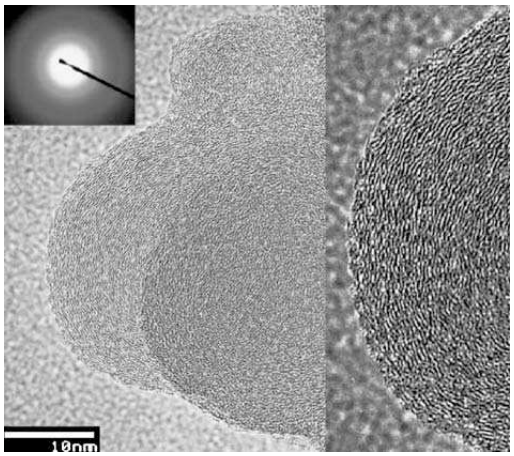


Figure 2.8: Soot particles viewed in a TEM [63].

of engines (CFM56-5C and CFM56-5B). The analysis of the collected soot shown spherical elementary particles whose basic elements were graphitic microcrystals with some carbon sheets stacked together like the successive skins in an onion like structure [55]. The size distribution of these particles was characterized by mean diameter around 20-25 nm, with a significant number of particle size under 10 nm. In addition, these elementary particles agglomerate to form aggregates, containing among 30 to 60 elementary particles in average, and a fractal dimension around 1.8. This indicates that

they have a lacey structure rather than a compact shape, for which the fractal dimension would be around 3. The average gyration diameter of these aggregates was around a few tens of nm depending on the motor type.

Recently, D. Delhaye et all have shown an experimental characterization of the morphology, structure and chemical properties of soot particles emitted from various aircraft engines (CFM56-5C, -7B, SaM-146), and a combustor [16, 66]. The soot nanoparticles were collected by direct impaction on electron microscope grids and analyzed by using Transmission electron microscopy (TEM) to determine the aggregates fractal dimension as well as soot primary particles and aggregates size distributions. The morphology, structure and texture of primary particles were also determined in addition to the elemental composition by means of X-ray energy dispersive spectrometry (XREDS). They show that irrespective of the aircraft engine considered, soot aggregates exhibit a fractal morphology (Fig. 2.9) and are composed of primary particles with diameter values distributed between 5 to 60 nm following a lognormal law (cf. Fig. Fig. 2.9). These particles show a turbostratic texture and are mainly made of C, O and traces of S. Carbonaceous cristallites that compose the soot particles have typical in-plane extensions of 2 nm and interplanar distances larger or equal to 0.36 nm.

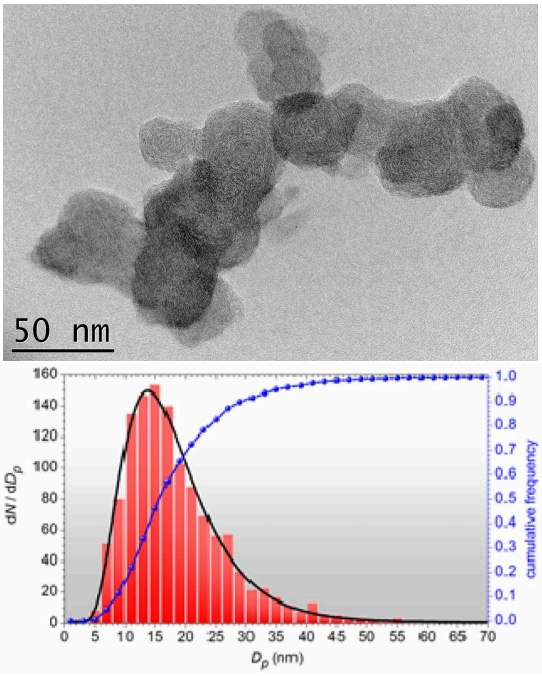


Figure 2.9: soot aggregate emitted from a SaM146 engine.size distribution of primary particles emitted from a SaM146 engine [16].

Moreover, the variability of optical properties of combustion particles generated from a propane diffusion flame under varying fuel to air (C/O) ratios was studied with a three-wavelength nephelometer, a particle soot absorption photometer, and an integrating sphere photometer [67]. Information on particle size distribution, morphology, and elemental carbon to total carbon (EC/TC) ratios were obtained from scanning mobility particle sizer measurements, transmission electron microscopy analysis, and thermal-optical analysis.

Please note, that the terminology used in the above mentioned work follows Petzold et al [68] where the term black carbon (BC) is used as a qualitative term for light-absorbing carbonaceous substances, black carbon mass determined by optical absorption methods is referred to as equivalent black carbon (EBC), and the term elemental carbon (EC) is used in thermochemical classification.

Particles generated under low C/O (0.22) ratios were >100 nm in mobility diameter and of high elemental carbon fraction (EC/TC=0.77) and low brown carbon to equivalent black carbon (BrC/EBC) ratios (0.01), while those produced under high C/O (0.60) ratios had smaller mobility diameters (<50 nm), low elemental carbon fraction (EC/TC=0.09) and high BrC/EBC ratio >100 (Fig. 2.10). Figure 2.11 shows TEM pictures of sampled particles. Particles generated under a low C/O ratio were fractal-like aggregates with D=1.74±0.08 and a=5-6 nm, while those generated under a high C/O ratio were nearly spherical in shape.

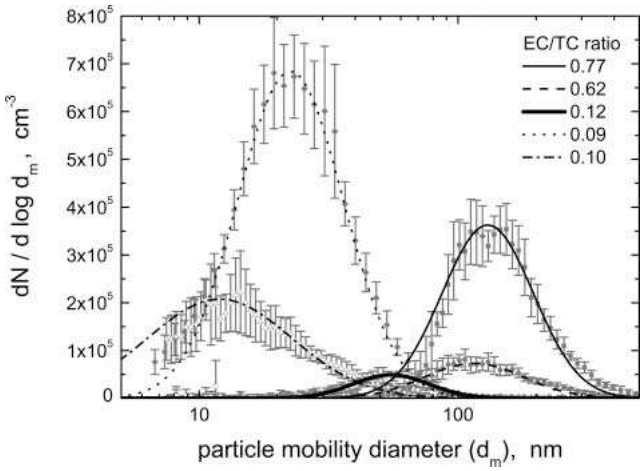


Figure 2.10: Mobility size distributions of particles generated from the CAST burner under different combustion conditions. The legend shows measured EC/TC ratios for these particles [67].

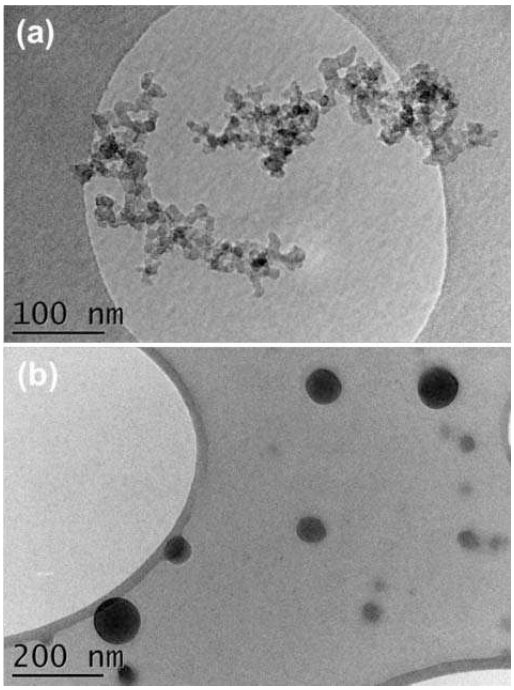


Figure 2.11: TEM pictures of combustion particles generated under (a) C/O ratio = 0.22 and (b) C/O ratio = 0.6 [67].

2.2.4 Chemical composition

As already mentioned before, soot aircraft are mainly composed of carbon atoms. However, studies based on the use of X-ray spectrometry showed that primary particles, collected at the outlet of commercial aircraft engines, also contain a small fraction of oxygen atoms (generally less than 3% in atomic percent), and very small traces of sulfur atoms (atomic percentage of sulfur of less than 0.5%) [55].

It is interesting to note that the soot collected in the combustion chamber of a D30KU engine contains an amount of sulfur slightly higher [35] although this can not be attributed to differences in the atomic composition of the fuel used in the different experiments. So it seems that it is rather the differences in combustion conditions in the different engines that are responsible for the sulfur contents measured in the soot. Trace amounts of iron and copper were also detected, probably arising from wear of metal engine parts.

Further analysis by infrared and Raman spectroscopy evidenced the vibration bands related aromatic structures (bands D) CC stretching vibration in the graphite (G-band) and signals corresponding to CH_2 and CH_3 aliphatic groups (that could be located for instance on the boundaries of the graphitic

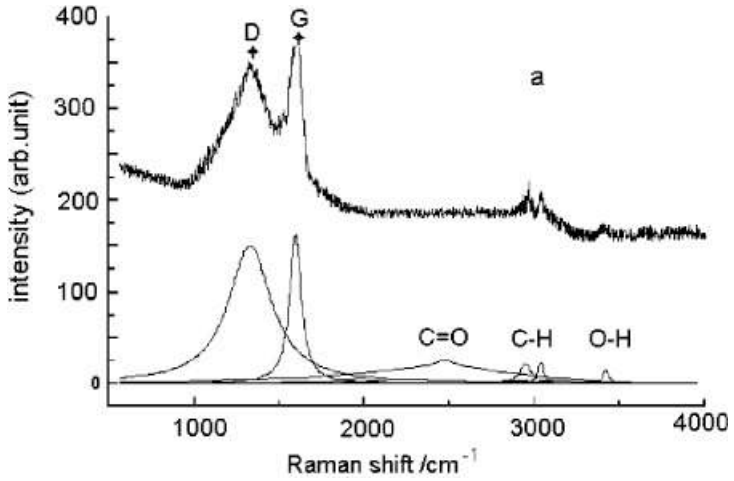


Figure 2.12: Raman spectrum of a soot nanoparticle [63].

sheets). Bands of oxygenated groups were also evidenced, mainly associated to the vibration of the OH (hydroxyl) and C=O (carbonyl or carboxyl) bonds. [63, 55].

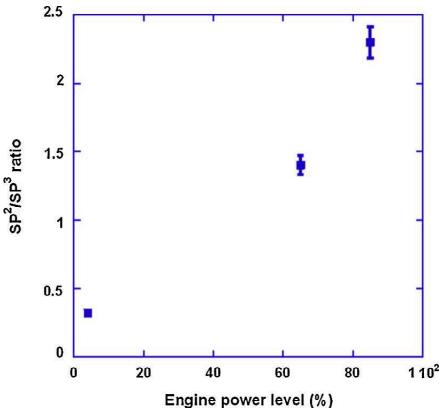


Figure 2.13: Carbon sp^2/sp^3 ratio of JP-8 derived soot at 4, 65, and 85% engine power levels [61].

Another interesting information results from the relationship between engine power level and soot composition. Figure 2.13 taken from Ref. [61] shows X-ray photoelectron spectroscopy (XPS) data for three selected engine power levels. Here, deconvolution has been applied to the high-resolution spectrum about the C1s position at 284.5 eV to resolve the carbon sp^2 , sp^3 hybridization components and oxygen functional groups. A monotonic trend with engine power is observed for increasing sp^2 content at the expense of sp^3 bonded carbon. These results are also consistent with the trend of

increasing black-to-organic carbon content with power level, as reported by Anderson et al [62].

2.2.5 Reactivity

The adsorption of a particular gas onto a soot particle is strongly dependent on the properties of the gas molecules and on the soot surface.

Soot particles exhibit a large specific surface area, $\sim$ 100 $m^2 g^{-1}$, which suggests a high potential for heterogeneous interactions with atmospheric trace gases. Consequently, there have been many attempts to evaluate the importance of chemical transformations of atmospheric constituents on soot particle surfaces, especially those involving O_3 and NO_x [71]. Other work has focused on the heterogeneous reactions of various atmospheric oxidants with PAHs [74, 75, 76, 77]. PAHs degradation on soot particles in the presence of electromagnetic radiation has also been studied [74][78]. Furthermore, the key role of carbonaceous aerosols as condensation nucleus of ice particles have lead to an exhaustive understanding of their aging condition and hydrophilicity. The adsorption on soot of toxic gases such as hydrogen chloride (HCl) issued from the burning of polivinyl chloride in fire situations has also been studied[79].

An exhaustive list of the molecules that can interact with soot would thus contain at least:

Polar Molecules: In the case of polar molecules (e.g., H_2O, HF, HCl, HBr, CO, NH_3, NO, and HCHO), atom electronegativity and molecular structure result in a molecular dipole moment. Such molecules are preferentially adsorbed at sites with unpaired electrons and at sites where oxygenated groups are present. In addition to the weaker van der Waals forces that control the physisorption of non-polar molecules, polar molecules are likely to be held by hydrogen bonding [69]. Also, molecules with high dipole moments are preferentially adsorbed over, and may even displace, those with smaller dipole moments [70, 71].

Paramagnetic Molecules: Paramagnetic molecules such as O_2 , NO_2, and NO have unpaired electrons with parallel spins. Since many chemical functionalities on the soot particle surface may also contain unpaired electrons, the interaction of this type of adsorbate molecule with these sites will be strong. The presence of paramagnetic molecules in the soot environment is expected to affect the adsorption properties of the soot toward other adsorbates, at least for those that may be adsorbed by the same sites. Study

of the adsorption of these gases on soot in combination with other diamagnetic or paramagnetic gases has provided insights into the coadsorption of multiple adsorbates [72].

Aromatic Molecules: Aromatic adsorbates, such as benzene and toluene for instance, interact most strongly with carbonyl groups (C=O, carbon-oxygen double bond) on the soot surface [70]. The affinity of aromatic adsorbates is thus enhanced by an increase in the number of carbonyl groups, that may arise from soot aging for instance.

Other Organic Compounds: Non-polar paraffinic compounds are hydrophobic in nature and adsorb preferentially on carbonaceous surfaces free from surface oxides [70]. Such surfaces preferentially adsorb hydrocarbon vapors relative to water vapor [71]. Unsaturated organic compounds are preferred to saturated compounds on polar surfaces [73].

In theoretical simulations it is often possible to avoid modeling the whole soot nanoparticle, since reactivity is generally related to chemical interaction at a given point of the soot surface. Thus, for reactivity studies, it is important to accurately model the immediate vicinity of the site where the reactivity takes place. Then, using small carbon clusters in the corresponding quantum chemistry framework would appear to be sufficiently relevant in most cases.

Water adsorption on pure graphite or graphene sheets without any surface defects has been the subject of several academic studies. For instance, in a recent study, Rubes et al. made use of DFT/CC (coupled cluster) calculations to simulate interactions of H_2O with carbonaceous aggregate, as a function of the increasing size of these aggregates [80]. The water adsorption energy on pure graphite and graphene was estimated to be ~ -15.0 kJ/mol and -13.3 kJ/mol respectively.

Furthermore, Jordan et al [81] published a study on H_2O/graphite interaction, by using a DFT/SAPT ("symmetry adapted perturbation theory") method, which provides better results than those published by the MP2 method previously used [82](∼ -24 kJ/mol). In this study, the calculated interaction energy was equal to -11.3 kJ/mol, closer to commonly accepted values of studies based on classical models (around -10 kJ/mol) [83] and to the experimentally measured value of about -15 kJ/mol [84].

Anyway, these results show that, in the lack of defect, a perfect graphite surface or a graphene sheet may attract only very few water molecules. The hydrophilicity of soot surfaces might thus come from the presence of surface defects at the soot surface, particularly defects resulting from the oxidation of the surfaces.

Adsorption of molecular or atomic oxygen on graphene was studied by using a single, infinite, plane of graphite, or a large carbon aggregate, the edges of which being saturated by hydrogen atoms. Thus, Li et al. modeled the oxidation of $C_{12}H_{24}$ and $C_{54}H_{12}$ aggregates to compare experimental vs theoretical results of graphene oxide. Their results showed that, as in the case of an infinite graphite surface, the attack of an oxygen atom leads to the formation of an epoxy-like structure, with a computed adsorption energy of $-55{,}34$ kJ/mol [85, 86] or $-73{,}79$ kJ/mol [87] depending on the functional used in the DFT method [88]. Then, the adsorption of additional oxygen atoms on the surface takes place on sites close to the one where the first atom is adsorbed, because of the breaking of the underlying C-C bonds. This process, also experimentally observed, is known as unzipping (i.e., a progressive tearing of the graphite sheet).

Another event that can cause a strong soot-water affinity are the "structural" defects. Among them, the most common one is the atomic vacancy, i.e., the lack of one (monoatomic vacancy) or several (multi-vacancy) carbon atoms in the considered carbon structure. Many studies have been published on these subject to describe their structural, electronic and magnetic properties, most of them being focused on mono [89] or divacancy sites [90].

Detailed studies of larger multivacancies (also observed experimentally by [91]) were recently published [92, 93]. In general, these theoretical studies have shown that carbon surfaces vacancies are stabilized by the formation of one or more pentadienic/pentagonal cycles adjacent to the vacancy and a slight deformation of the surface out of the plane.

Furthermore, the presence of dangling bonds on the edges of the vacancy site allows to consider a stronger reactivity than on a perfect surface. Thus, the adsorption of a water molecule has been studied by computational quantum chemistry methods on a carbon surface comprising a single [94] or a double atom vacancy [95]. This work showed that H_2O can be dissociated leading to the formation of a C = O (ketone-like) group on the edge of the monoatomic vacancy and a C-O-C (ether-like) group on the edge of a diatomic one.

Although this H_2O dissociation reaction is exothermic ($-36{,}9$ kJ/mol for the monoatomic defect [96]), it is characterized by a relatively large energy barrier (20,75 kJ/mol) to overcome from an initial physisorbed local minimum in the potential energy surface (PES) [94]. However, it is important to note that, again, significant differences were obtained in the results depending on the type of theoretical method, functionals and graphitic surface considered.

In addition, perfect and defective graphite surfaces were used to model the interaction of nitrated species like HNO_3 and NO_2 with soot, through quantum molecular dynamics simulations (within the Car Parrinello scheme) [97, 98] that helped to better understand the surface oxidation mechanisms by these molecules.

Finally, a series of studies on the adsorption of water aggregates on functionalized carbon surfaces has been developed in Besançon during the last 10 years [99, 100, 101]. In these studies, relatively large systems were considered by using, for instance, the ONIOM method that combines a high-level quantum method restricted to the heart of the system studied, to a semi-empirical description of the remaining surface. These studies focused on carbon surfaces having an OH or a COOH group anchored on the face or on the edge of the carbon system and they showed that i) the water molecules affinity is always greater at the edge sites than on the face surface and ii) that a COOH group is more attractive than an OH group.

Moreover, these quantum chemistry studies were used to build a classical potential model for describing the interaction between water and the functionalized carbon surface interaction, which was then used in molecular dynamics simulation to characterize the influence of different random distributions of OH and COOH sites on the water-functionalized graphite interaction, as a function of temperature and coverage rate of water molecules [102, 103, 104]. The results confirmed that a COOH site is always much more attractive for water than an OH site, and that very low temperatures (200 K) have to be considered for an efficient trapping of the water molecules in the OH vicinity, when these OH sites are competing with COOH sites in their neighborhood.

Recently, defects at the surface of carbon clusters have been modeled by single atomic vacancies on which water molecules have been approached. The results of the quantum calculations evidence dissociative chemisorption of the first adsorbed water molecule, resulting in the modification of the carbonaceous clusters with formation of a ketone-like structure at their surface. The corresponding reaction is however characterized by a substantial activation barrier from the initial physisorbed state, as already evidenced on infinite graphite and graphene surfaces [96, 94]. Moreover, although the vacancy site at the carbonaceous surface may dissociate a first incoming water molecule, this dissociation results in the saturation of the vacancy site which then behaves as a ketone-like site, i.e. as a quite weak nucleation center for additional water molecules. Indeed, the values of the mean adsorption energy per water molecule show that the affinity of such ketone-like site was similar to that previously found on an epoxide-like site [105], and weaker than that on a OH site [100]. It was also much weaker than the affinity between a COOH site and water [99, 100, 101].

2.2.6 Optical properties

Accurate information about light scattering properties of small particles is important in several fields of science and engineering, such as atmospheric optics, oceanography, meteorology, pollution assessment, aerosol science and technology, electrical engineering, astrophysics, colloidal chemistry, biophysics, and particle sizing.

Moreover, the assumption that optical properties and radiative effects of atmospheric trace species may be predicted from their concentrations and chemical composition, is fundamental for modeling how anthropogenic activities may induce climate evolutions. Indeed, in a general way, the use of transport models to calculate climatic effects of any species relies on two implicit assumptions:

1. There is a predictable relationship between emission (generation of new particles) and spatially distributed atmospheric concentration. This relationship is governed by advection, chemical transformation, and removal.

2. There is a predictable relationship between atmospheric concentration and its effects on radiative transfer. This relationship involves the optical properties of the species.

As it is shown in fig 2.14, starting parameters such as the wavelength of the incident wave, morphological details and the complex refractive index of the particles allow to compute optical properties like, for instance, absorption and scattering cross sections. Then, combining these results with the concentration of light absorbing particles, allows to estimate changes in the atmospheric radiative transfer. Within this framework, global climate models may predict the effect of aerosols on atmospheric radiative balance.

In this context, the role of carbonaceous particles in determining whether aerosols warm or cool the atmosphere is still not clear in spite of a large body of research works. Indeed, accurate extinction (absorption + scattering) cross section values (which could be used with the species concentration to predict changes in intensity) depend on the particle morphology and on the material refractive index [19].

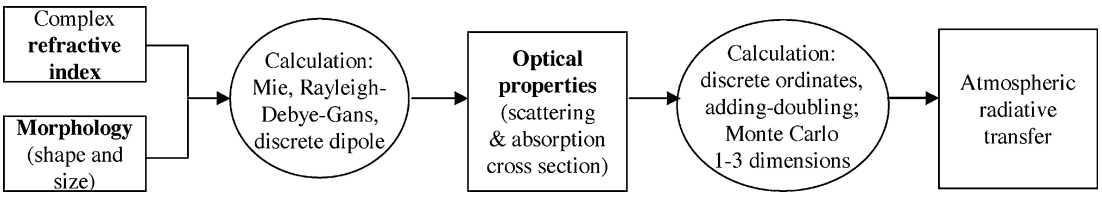


Figure 2.14: Calculating radiative transfer [19].

Hence, the quality of the approximations made for the choice of optical properties (refractive index) used to compute the effects of aerosols is very important for radiative transfer models in simulation codes of the global atmospheric radiative balance. An accurate evaluation of the optical index of soot particles as a function of their morphology and chemical structure is thus very desirable for the estimation of the climate forcing. Indeed, optical indices for small molecules such as CO_2 are very well known, while for soot nanoparticles they remain uncertain/inaccurate due to the large variety of morphologies itself due to the large number of possible combustion sources (*cf.* Fig 2.15).

Depending on the size of the soot particles, the models used in the environmental literature to compute the optical cross sections are mainly the Rayleigh scattering model for small particles, Mie theory or geometrical optics for the bigger particles. Each model is applied within its validity area according to the value of the parameter:

$$\beta = \frac{\pi D_p}{\lambda}, \tag{2.1}$$

where D_p is the particle diameter and λ the wavelength of the incident beam. Thus,

1. if $\beta >> 1$ geometrical optic can be used;

2. if $\beta \approx 1$ Mie's theory is used, which gives the exact solution to Maxwell equations for scattering and absorption by spherical particles;

3. if $\beta << 1$ (as it will be the case in my work), Rayleigh scattering model is used. In this model, the electromagnetic field of the incident wave is estimated to be quasi-uniform throughout the particle. It creates an oscillating dipole in phase with the incident wave, like a molecular dipole. The scattered wave is then the wave emitted by this oscillating dipole.

In addition to Mie exact solution to Maxwell equations for the spherical problem, some simple analytical formulas can be used to estimate the optical extinction cross-sections of small spherical carbon particles considering several geometrical arrangement and their complex refractive index [107]. Other methods employed in atmospheric modeling are the volume-equivalent sphere approach and the Maxwell–Garnett mixing theory approach [19]. In the volume equivalent sphere approach, the absorption properties of soot particles are calculated using Mie or Rayleigh theory for a volume equivalent sphere. The refractive index of this volume equivalent sphere is assumed to be equal to the bulk refractive index of the material composing the sphere.

Reference	Cited by	Real (n)	Imag. (k)	Material
Measurements				
Coal				
McCartney et al. 1965	TW	1.7–2.0	0.25–0.5	Coal of various ranks
Gilbert 1962		1.8–2.05	0–0.8	Coal from specific mines
Carbon particles				
1 Batten 1985	H	1.20–1.35	0.1–0.22	Kerosene soot
2 Chang and Charalampopoulos 1990		1.77	0.63	Premixed propane-oxygen, $\phi = 1.8$
3 Chippett and Gray 1978		1.9	0.35	Smoke generator
4 Dalzell and Sarofim 1969	H	1.56	0.47	Average of coal and propane soots
5 Erickson et al. 1964		1.4	1.0	Benzene-air flame
6 Habib and Vervisch 1988		1.3	0.3	Premixed flames, various fuels
7 Janzen 1979	FMK	2.0	1.0	Carbon black
8 Lee and Tien 1981	CHH	1.95	0.48	Polystyrene and plexiglas flames
9 Mullins and Williams 1987		1.88–1.93	0.39–0.45	Toluene, propane, n-heptane
10 Marley et al. 2001		1.87	0.56	Soot from candle flame
11 Marley et al. 2001		1.68	0.56	Diesel soot
12 Pluchino et al. 1980	H, CHH	1.7–1.8	0.6–0.8	Carbon black, single particle
13 Powell and Zinn 1983	CHH	1.108	0.075	Flaming polymeric materials
14 Senftleben and Benedict 1918	TW	1.9	0.65	Arc-lamp soot
15 Stagg and Charalampopoulos 1993		1.52	0.36	Propane flame
16 Wu et al. 1997		1.58	0.51	Turbulent diffusion flames
Graphite				
Egan 1982	CHH	1.67–2.05	0.01–0.7	1st Intercomparison work
Taft and Phillip 1965		2.58	1.44	Graphite (normal incidence)
Tsu et al. 1978	CHH	2.05–2.75	0.66–1.46	3 grades of graphite
17 Greenaway et al. 1969	MR	2.72/1.46	1.34/0.0	Graphite (normal/parallel incidence)
Stagg and Charalampopoulos 1993		2.65	1.39	Pyrolytic graphite
Derived Values				
Original source	Cited by	Real (n)	Imag. (k)	Notes
Dalzell and Sarofim 1969	MR	1.84	0.46	Adjusted for void fraction
Janzen 1979	H, FMK	1.25	0.25	Hypothesized for 75% air, 25% soot
Janzen 1979	H, FMK	1.5	0.5	Hypothesized for 50% air, 50% soot
Ergun and McCartney 1960 [a]	MR	2.02	0.56	Interpolated to H/C ratio of carbon black
Secondary References				
Citing reference	Cited by	Real (n)	Imag. (k)	Original source
Ackermann and Toon 1981	H	1.94	0.66	Senftleben and Benedict 1918
Bergstrom 1972	FMK, CHH	1.95	0.66	Senftleben and Benedict 1918
Bergstrom 1973	H	2.0	0.66	Senftleben and Benedict 1918
Twitty and Weinman 1971	FMK	1.80	0.8	See this tabulation
Hess and Herd 1993	FMK	2.0	1.0	Janzen 1979
Hänel 1987	H	1.9	1.0	Value not found in Hänel paper
Janzen 1979	CHH	1.4–2.35	0.46–1.42	Values not found in this paper
Jaenicke 1988	H, CHH	1.75	0.44	Twitty and Weinman
Kattawar and Heard 1976	H	1.95	0.66	Senftleben and Benedict 1918
Ouimette and Flagan 1982	H	1.56	0.47	Dalzell and Sarofim 1969
Roessler and Faxvog 1980	H	1.96	0.66	Senftleben and Benedict 1918
Roessler and Faxvog 1980	CHH	1.75	0.5	Value not found in cited paper
Roessler and Faxvog 1980	H	2.0	0.66	Value not found in cited paper
Shettle and Fenn 1979	H	1.76	0.45	Average of Twitty and Weinman 1971
"various textbooks"	H	2.0	1.0	Probably from Janzen 1979

[a] Paper assumed to contain data from conference proceedings paper by Horvath (1993) citation.

Figure 2.15: Complex refractive index for different carbonaceous material [19].

In the mixing-theory approach, the effective permittivity of a sphere enclosing the soot particles is determined using the Maxwell–Garnett mixing rule using the permittivities of soot and its volume and the permittivity

of the ambient atmosphere and the complementary volume. The absorption properties of the effective sphere are then determined by using Mie's or Rayleigh's results. These methods have the advantage to be quite simple. However, they poorly characterize the radiative properties of soot. Hence, it is suspected that the structural details of the soot particles have indeed to be considered.

In fact, more involved exact solutions to Maxwell equations can be used for that purpose. Among these, the T-matrix method is a powerful asymptotically exact technique for computing light scattering by rotationally symmetric particles [117, 108]. It is based on the expansion of the solution to Maxwell equations using a (truncated) basis of spherical vector wave functions and boundary conditions on the surface of the particle, that lead to a simplified expression of the scattered field outside the particle as a surface integral. Its applicability to particles with very large size parameters and various aspect ratios, and also the use of a highly efficient analytical method for computing orientationally averaged optical cross sections and scattering matrix elements certainly make T-matrix codes a very powerful tool for computing the scattering of light by randomly oriented rotationally symmetric particles based on directly solving Maxwell's equations. However, although the method is theoretically applicable to any particle shape (using an infinite basis), an obvious disadvantage of the corresponding codes is that most practical implementations of the technique deal with solids of revolution. So, they are mainly applicable to spheroids, finite circular cylinders, and Chebyshev particles [109].

In contrast, computer codes based on numerical approaches such as the discrete dipole approximation (DDA) [110] or the finite difference time domain (FDTD) method [111] can be used with arbitrarily shaped particles. Several research groups have implemented a DDA code for their own use. Some codes are publicly available, either freely or commercially, for instance, the commercially available SIRRI, the publicly available DDSCAT and ADDA or ZDD (available for its developers) [112]. The DDA codes usually solve an integral form of Maxwell equations for an in incident plane wave (hence a single frequency) by discretizing the volume of the scatterer on a Cartesian grid and identifying the scattering of each subvolume element as the scattering of a single induced dipole (i.e. Rayleigh's approximation for each discretization element). All these induced dipoles must first be determined self-consistently for each incident wave and geometrical configuration of the scatterer, which can be quite time consuming. For this self-consistent determination, a key ingredient is the effective polarizability of each discretization element, which is computed using the (complex) refractive index of the

material in the discretization element (thus allowing for completely inhomogeneous scatterers). All the measurable optical quantities can latter be computed from these dipoles.

However, none of these methods takes into account the exact positions of the atoms in the system under consideration, and, as a consequence, they cannot account for the influence of the atomistic structure of the nanoparticles on their spectroscopic signals. Thus, in this work and as explained in a next chapter, an atomistic point dipole interaction method (PDI) similar to DDA but based on the use of atoms as discretization elements (hence with some peculiarities in the determination of the effective polarizabilities) is used to calculate the optical properties of nanoparticles made of pure carbon.

Moreover, as mentioned before, soot is commonly observed to be made of a large number of inter-connected nearly spherical primary particles (monomers). Despite the random distribution of these spherical monomers within an aggregate, morphology of soot fairly follows a fractal law [113]. Thus, in addition to the Multi-Sphere T-Matrix (MSTM) method [114] and several DDA codes implementations [112] a common approximate model used in the visible region to compute the optical properties of soot is the Rayleigh–Debye–Gans theory (RDG) [115] applicable to the fractal soot structures [116].

However, it should be noted that in my PhD work, only optical properties of "primary" soot nanoparticles have been computed by means of the PDI approach, the extension to large aggregates being thus one of the perspectives of this work.

Bibliography

[1] J. Penner, D. Lister, D. Griggs, D. Dokken, and M. McFarland, IPCC Special Report, Aviation and the global atmosphere (Cambridge University Press, **1999**).

[2] A. P. M. Baede, E. Ahlonsou, Y. Ding, and D. Schimel, IPCC Third Assessment Report - Climate Change 2001 : The Scientific Basis (Cambridge University Press, 2001), chap. The Climate System : an Overview, **2001** pp. 85–98.

[3] J. H. Seinfeld and S. N. Pandis, Atmospheric chemistry and physics. Wiley,**1998**.

[4] A. Miller, Meteorology, Merril Books, Colombus, Ohio, **1966**.

[5] V. Ramaswamy, O. Boucher, J. Haigh, D. Hauglustaine, J. Haywood, G. Myhre, T. Nakajima, G. Shi, and S. Solomon, Third Assessment Report of the Intergovernmental Panel on Climate Change : Climate Change 2001.The Scientific Basis (Cambridge University Press, Cambridge, 2001), chap. Radiative Forcing of Climate Change,**2001**, pp. 349-416.

[6] V. Ramaswamy, M.-L. Chanin, J. Angell, J. Barnett, D. Gaffen, M. Gelman, P. Keckhut, Y. Koshelkov, K. Labitzke, J.-J. Lin, et al., Reviews of Geophysics,**2001** , 39(1), 71.

[7] P. Forster, V. Ramaswamy, P. Artaxo, T. Berntsen, R. Betts, D. Fahey, J. Haywood, J. Lean, D. Lowe, G. Myhre, et al., Fourth Assessment Report of the Intergovernmental Panel on Climate Change, Climate Change 2007 : The Physical Science Basis (Cambridge University Press, Cambridge, United Kingdom and New York, NY, USA., 2007), chap. Changes in Atmospheric Constituents and in Radiative Forcing,**2007**, pp. 130-234.

[8] J. Haywood and O. Boucher, Reviews of Geophysics,**2000** , 38(4), 513.

[9] J. Penner, D. Hegg, and R. Leaitch, Environmental Science and Technology,**2001** , 35(15), 332A.

[10] U. Lohmann and J. Feichter, Atmospheric Chemistry and Physics,**2005**, 5, 715.

[11] S. Twomey, Journal of Atmospheric Sciences,**1977** , 34, 1149.

[12] B. Albrecht, Science,**1989**, 245, 1227.

[13] Pedata, N. Bergamasco, A. D'Anna, et al.,Toxicol. Lett.,**2013**, 219, 307-314.

[14] L. Holder, B.J. Carter, R. Goth-Goldstein, D.Lucas, C.P. Koshland, Atmos. Pollut. Res.,**2012** , 3,25-31.

[15] Lee, D.S., G. Pitari, V. Grewe, K. Gierens, J.E. Penner, A. Petzold, M.J. Prather, U. Schumann, A. Bais, T. Berntsen, D. Iachetti, L.L. Lim, R. Sausen (2010).Transport impacts on atmosphere and climate: Aviation. Atmos. Env.,**2010** , 44 (37) 4678-4734.

[16] Delhaye, D Ferry. Morphology and structure of soot emitted from various aircraft engines. International Aerosol Conference 2014, Oct **2014**, BUSAN, South Korea.

[17] Ferry D., C. Rolland, D. Delhaye, F. Barlesi, P. Robert, P. Bongrand, J. Vitte, Jet exhaust particles alter human dendritic cell maturation. Inflamm. Res.,**2011**, 60 (3) 255-263.

[18] A. Sgro, A. Simonelli, L. Pascarella, P. Minutolo, D. Guarnieri, N. Sannolo, P. Netti, A. D'Anna, Environ. Sci. Technol.,**2009** ,43,2608-2613.

[19] Tami C. Bond, Robert W. Bergstrom, Aerosol Science and Technology,**2006** , 40:27-67.

[20] Ramanathan, V., and Carmichael, G., Global and Regional Climate Changes Due to Black Carbon. Nat. Geosci.**2008**, 1:221-227

[21] Bond, T. C., Doherty, S. J., Fahey, D. W., Forster, P. M., Berntsen, T., DeAngelo, B. J., Bounding the Role of Black Carbon in the Climate System: A Scientific Assessment. J. Geophys. Res. Atmos.**2013** ,118:5380-5552.

[22] Hoffer, A., Gelencser, A., Guyon, P., Kiss, G., Schmid, O., Frank, G. P.,Optical Properties of Humic-Like Substances (HULIS) in Biomass-Burning Aerosols. Atmos. Chem. Phys.**2006** , 6:3563-3570.

[23] Schnaiter, M., Gimmler, M., Llamas, I., Linke, C., Jaeger, C., and Mutschke, H., Strong Spectral Dependence of Light Absorption by Organic Carbon Particles Formed by Propane Combustion. Atmos. Chem. Phys.**2006**, 6:2981-2990.

[24] Andreae, M. O., and Gelencser, A., Black Carbon or Brown Carbon? The Nature of Light-Absorbing Carbonaceous Aerosols. Atmos. Chem. Phys.**2006**, 6:3131-3148.

[25] Alexander, D. T. L., Crozier, P. A., and Anderson, J. R. , Brown Carbon Spheres in East Asian Outflow and Their Optical Properties. Science,**2008**, 321:833-836.

[26] Lewis, K., Arnott, W. P., Moosmuller, H., and Wold, C. E. . Strong Spectral Variation of Biomass Smoke Light Absorption and Single Scattering Albedo Observed with a Novel Dual-Wavelength Photoacoustic Instrument. J. Geophys. Res.**2008**, 113:D16203.

[27] Chakrabarty, R. K., Moosmuller, H., Chen, L. W. A., Lewis, K., Arnott, W. P., Mazzoleni, C., Brown Carbon in Tar Balls from Smoldering Biomass Combustion. Atmos. Chem. Phys. **2010**, 10:6363-6370.

[28] Graber, E. R., and Rudich, Y. , Atmospheric HULIS: How Humic-Like Are They? A Comprehensive and Critical Review. Atmos. Chem. Phys.,**2006**, 6:729-753.

[29] Limbeck, A., Kulmala, M., and Puxbaum, H., Secondary Organic Aerosol Formation in the Atmosphere via Heterogeneous Reaction of Gaseous Isoprene on Acidic Particles. Geophys. Res. Lett.**2003**, 30(19), 1996, doi:10.1029/2003GL017738.

[30] Moosmuller, H., Chakrabarty, R. K., and Arnott, W. P., Aerosol Light Absorption and Its Measurement: A Review. J. Quant. Spectrosc. Radiat. Transfer,**2009**,110:844-878.

[31] A. Oberlin, Chemistry and Physics of Carbon,**1989**,22, 1.

[32] M. Wentzel, H. Gorzawski, K.-H. Naumann, H. Saathoff, and S. Weinbruch, Journal of Aerosol Science, **2003** 34(10), 1347.

[33] M. P osfai, J. Anderson, P. Buseck, and H. Sievering, Journal of Geophysical Research D : Atmospheres **1999** 104(D17), 21685.

[34] W. Grieco, J. Howard, L. Rainey, and J. Vander Sande, Carbon.**2000**, 38(4), 597.

[35] D. Ferry, J. Suzanne, S. Nitsche, O. Popovitcheva, and N. Shonija, Journal of Geophysical Research. **2002**, 107, 4734.

[36] Schumann U., P. Jebberger , C. Voigt . Contrail ice particles in aircraft wakes and their climatic importance. Geophys. Res. Lett. **2013**,40 (11) 2867-2872.

[37] M.O. Andreae, V. Ramanathan, Science. **2013**, 340 ,280-281.

[38] F. Stordal, G. Myhre, W. Arlander, T. Svendby, E. Stordal, W. Rossow, and D. Lee, Atmospheric Chemistry and Physics Discussions,**2004**, 4, 6473.

[39] F. Stordal, G. Myhre, E. Stordal, W. Rossow, D. Lee, D. Arlander, and T. Svendby, Atmospheric Chemistry and Physics. **2005**, 5(8), 2155.

[40] S. Marquart, M. Ponater, F. Mager, and R. Sausen, Journal of Climate. **2003**, 16(17), 2890.

[41] R. Sausen, I. Isaksen, V. Grewe, D. Hauglustaine, D. Lee, G. Myhre, M. Kohler, G. Pitari, U. Schumann, F. Stordal, et al., Meteorologische Zeitschrift. **2005**, 14(4), 555.

[42] P. Minnis, J. Ayers, R. Palikonda, and D. Phan, Journal of Climate. **2004**, 17(8), 1671.

[43] H. Mannstein and U. Schumann, Meteorologische Zeitschrift. **2005**, 14(4), 549.

[44] C. Zerefos, K. Eleftheratos, D. Balis, P. Zanis, G. Tselioudis, and C. Meleti, Atmospheric Chemistry and Physics. **2003**, 3, 1633.

[45] I.M. Kennedy, Prog. Energy Combust. Sci. **1997**, 23, 95.

[46] H. Richter and J.B. Howard, Prog. Energy Combust. Sci. **2000**,26, 565.

[47] F. Douce, Etude de la formation des particules de suie a partir de constituants representatifs du gazole, Ph.D. thesis, Universite d'Orleans **2001**.

[48] J.T. McKinnon and J.B. Howard, The roles of PAH and acetylene in soot nucleation and growth, Proceeding oft he 24th Symposium (International) on Combustion, The Combustion Institute.**1992**, p.965.

[49] M. Frenklach, On surface growth mechanism of soot particles, Proceeding of the 26th Symposium (International) on Combustion, The Combustion Institute.**1996**, p. 2285.

[50] R. Dhaubhadel, F. Pierce, A. Chakrabarti, C.M. Sorensen, Phys. Rev. **2006**, E73, 011404.

[51] Popovicheva et al., Aerosol and Air Quality Research. **2014**, 14: 1392-1401.

[52] R.L. Vander Wal, A.J. Tomasek, Combust. Flame. **2003**, 134, 1-9.

[53] C. Han, Y. Liu, J. Ma, H. He, J. Chem. Phys. **2012**, 137, 084507.

[54] R.L. Vander Wal, A. Strzelec, T.J. Toops, C.S. Daw, C.L. Genzale, Fuel. **2013**, 113, 522-526.

[55] D. Delhaye, PhD Thesis, Université d'Aix-Marseille II, **2007**

[56] A. D'Anna, Proc. Combust. Inst. **2009**, 32,593-613.

[57] H. Wang, Proc. Combust. Inst. **2011**, 33, 41-67.

[58] M. Schenk, S. Lieb, H. Vieker, et al., ChemPhysChem. **2013**, 14,3248-3254.

[59] M. Balthasar, M. Frenklach, Proc. Combust. Inst. **2005**,30,1467-1475.

[60] Marina Schenk et all.Proceedings of the Combustion Institute. **2015**, 35,1879-1886.

[61] Randy L. Vander Wal, Vicky M. Bryg, Chung-Hsuan Huang.Combustion and Flame. **2014**, 161, 602-611

[62] B.E. Anderson, A.J. Beyersdorf, C.H. Hudgins, J.V. Plant, K.L. Thornhill, E.L. Winstead, L.D. Ziemba, R. Howard, E. Corporan, R.C. Miake-Lye, S.C. Herndon, M. Timko, E. Woods, W. Dodds, B. Lee, G. Santoni, P. Whitefield, D. Hagen, P. Lobo, W.B. Knighton, D. Bulzan, K. Tacina, C. Wey, R.L. Vander Wal, A. Bhargava, Alternative Aviation Fuel Experiment (AAFEX), **2011**. NASA/TM- 2011-217059.

[63] O.B. Popovicheva, N.M. Persiantseva, B.V. Kuznetsov, T.A. Rakhmanova, N.K. Shonija, J. Suzanne, D. Ferry, J. Phys. Chem. **2003**, 107, 10046.

[64] O.B. Popovicheva, A. Starik, Atmos. Oceanic. Phys. **2007**, 43,147.

[65] B. Demirdjian, D. Ferry, J. Suzanne, O.B. Popovicheva, N.M. Persiantseva, N.K. Shonija, J. Atmos. Chem. **2007**, 56, 83.

[66] Petzold, A., R. Marsh, M. Johnson, M. Miller, Y. Sevcenco, D. Delhaye, A. Ibrahim, P. Williams, H. Bauer, A. Crayford, W.D. Bachalo, D. Raper. Evaluation of methods for measuring particulate matter emissions from gas turbines. Environ. Sci. Technol. **2011**, 45, (8), 3562-3568.

[67] J. Kim,H. Bauer,T. Dobovicnik,R. Hitzenberger,D. Lottin, D. Ferry, and A. Petzold,Assessing Optical Properties and Refractive Index of Combustion Aerosol Particles Through Combined Experimental and Modeling Studies, Aerosol Science and Technology. **2015**, 49, 340-350.

[68] Petzold, A., Ogren, J. A., Fiebig, M., Laj, P., Li, S. M., Baltensperger, U., Recommendations for Reporting Black Carbon Measurements. Atmos. Chem. Phys. **2013**, 13, 8365-8379.

[69] K.U. Goss and S.J. Eisenreich, Sorption of Volatile Organic Compounds to Particles from a Combustion Source at Different Temperatures and Relative Humidities, Atmospheric Environment, vol. 31, no. 17, **1997**, pp. 2827-2834.

[70] J.T. Cookson, Jr., Adsorption Mechanisms: The Chemistry of Organic Adsorption on Activated Carbon, in Carbon Adsorption Handbook, P.N. Cheremisinoff and F. Ellerbusch, Eds., Ann Arbor, MI: Ann Arbor Science Publ. Inc **1978**, pp. 241-279.

[71] D.J. Lary, D.E. Shallcross, and R. Toumi, Carbonaceous Aerosols and Their Potential Role in Atmospheric Chemistry, Journal of Geophysical Research-Atmospheres, vol. 104, no. D13, **1999**, pp. 15,929-15,940.

[72] A.R. Chughtai, M.M.O. Atteya, J. Kim, B.K. Konowalchuk, and D.M. Smith, Adsorption and Adsorbate Interaction at Soot Particle Surfaces, Carbon, vol. 36, no. 11, **1998**, pp. 1573-1589.

[73] P.N. Cheremisinoff and A.C. Morresi, Carbon Adsorption Applications, in Carbon Adsorption Handbook, P.N. Cheremisinoff and F. Ellerbusch, Eds., Ann Arbor, MI: Ann Arbor Science Publ.,Inc. **1978**, pp. 1-53

[74] Esteve W, Budzinski H, Villenave E .Relative rate constants for the heterogeneous reactions of NO2 and OH radicals with PAHs adsorbed on carbonaceous particles Part 2: PAHs adsorbed on diesel particulate exhaust SRM 1650a. Atmos Environ,**2006**, 40 (2):201-211.

[75] Gross S, Bertram AK ,Reactive uptake of NO3 , N2O5 , NO2 , HNO3 , and O3 on three types of PAH surfaces. J Phys Chem A, **2008** , 112(14):3104-3113.

[76] Kahan TF, Kwamena NOA, Donaldson DJ. Heterogeneous ozonation kinetics of PAHs on organic films. Atmos Environ, **2006**, 40(19):3448-3459.

[77] Mmereki BT, Donaldson DJ. Direct observation of the kinetics of an atmospherically important reaction at the air-aqueous interface. J Phys Chem A, **2003**, 107(50):11038–11042.

[78] Kamens RM, Karam H, Guo JH, Perry JM, Stockburger L . The behavior of oxygenated PAHs on atmospheric soot particles. Environ Sci Technol, **1989**, 23(7):801-806.

[79] Kathryn M. Butler and George W. Mulholland. Generation and Transport of Smoke Components. Fire Technology, **2004**, 40, 149-176.

[80] M. Rubes, P. Nachtigall, J. Vondrasek, and O. Bludsky, J. Phys. Chem. C, **2009**, 113, 8412.

[81] G.R. Jenness and K.D. Jordan, J. Phys. Chem. C, **2009**, 113, 10242.

[82] D. Feller and K.D. Jordan, J. Phys. Chem. A. **2000**, 104, 9971.

[83] K. Karapetian, K.D. Jordan, Water in confined geometries; V. Buch, J.P. Devlin, Eds.; Springer Verlag : Berlin, **2003**.

[84] N.N. Avgul, A.V. Kieslev, Chemistry and Physics of Carbon; P.L. Walker, Ed.; Dekker : New York, **1970**, vol. 6

[85] J.L. Li, K.N. Kudin, M.J. McAllister, R.K. Prud homme, I.A. Aksay, R. Car, Phys. Rev. Lett. **2006**, 96 ,176101.

[86] H.C. Schniepp, J.L. Li, M.J. McAllister, H. Sai, M. Herrera-Alonso, D.H. Adamson, R.K. Prud homme, R. Car, D.A. Saville, and I.A. Aksay, J. Phys. Chem. B, **2006**, 110 ,8535.

[87] K.A. Mkhoyan, A.W. Contryman, J. Silcox, D.A. Stewart, G. Eda, C. Mattevi, S. Miller, and M. Chhowalla, Nano Lett. **2009**, 9, 1058.

[88] Y. Ferro, A. Allouche, F. Marinelli, C. Brosset, Surf. Sci. **2004**, 559, 158.

[89] H. Tachikawa, H. Kawabata, J. Phys. Chem. C. **2009**, 113, 7603.

[90] V.A. Coleman, R. Knut, O. Karis, H. Grennberg, U. Jansson, R. Quinlan, B.C. Holloway, B. Sanyal, and O. Eriksson, J. Phys. D: Appl. Phys. **2008**, 41, 062001.

[91] Z. Tang, M. Hasegawa, T. Shimamura, Y. Nagai, T. Chiba, Y. Kawazoe, M. Takenaka, E. Kuramoto, and T. Iwata, Phys. Rev. Lett. **1999**, 82, 2532.

[92] K. Yamashita, M. Saito, T. Oda, Jpn. J. Appl. Phys. **2006**, 45 , 6534.

[93] M. Saito, K. Yamashita, T. Oda, Jpn. J. Appl. Phys. **2007**, 47, L1185.

[94] P. Cabrera Sanfelix and G.R. Darling, J. Phys. Chem. C. **2007**, 111, 18258.

[95] B. Sanyal, O. Eriksson, U. Jansson, H. Grennberg, Phys. Rev. B, **2009**, 79, 113409.

[96] A. Allouche, Y. Ferro, Carbon. **2006**, 44, 3320.

[97] A. Rodriguez-Fortea, M. Iannuzzi, M. Parrinello, J. Phys. Chem. C. **2007**, 111, 2251.

[98] A. Rodriguez-Fortea and M. Iannuzzi, J. Phys. Chem. C. **2008**, 112, 19642.

[99] S. Hamad, J.A. Mejias, S. Lago, S. Picaud and P.N.M. Hoang, J. Phys. Chem. B, **2004**, 108, 5405.

[100] B. Collignon, P.N.M. Hoang, S. Picaud and J.C. Rayez, Chem. Phys. Lett. **2005**,406 ,431.

[101] B. Collignon, P.N.M. Hoang, S. Picaud, and J.C. Rayez, Comp. Lett. **2005**, 1, 277.

[102] S. Picaud, P.N.M. Hoang, S. Hamad, J.A. Mejias, and S. Lago, J. Phys. Chem. B. **2004**, 108, 5410.

[103] S. Picaud, B. Collignon, P.N.M. Hoang, and J.C. Rayez, J. Phys. Chem. B. **2006** ,110, 8398.

[104] S. Picaud, B. Collignon, P.N.M. Hoang, and J.C. Rayez, Phys. Chem. Chem. Phys. **2008**, 10, 6998.

[105] M. Oubal, S. Picaud, J.C. Rayez, M.T. Rayez, Carbon. **2010**, 48, 1570.

[106] M. Oubal,S. Picaud, J.C. Rayez, M.T. Rayez. Surface Science. **2010**, 604, 1666-1673.

[107] B. Michel, Th. Henning, C. Jager, U. Kreibig.Optical extinction by spherical carbonaceous particles. Carbon **1999**, 37, 391–400

[108] Mishchenko M, Larry D, Mackowski D. T-Matrix computations of light scattering by nonspherical particles: A review. J. Quant. Spectrosc.Radial. Transfer **1996** Vol. 55, No. 5, pp. 535-515.

[109] Mishchenko M, Larry D. Travis. Capabilities and limitations of a current Fortran implementation of the T-Matrix method for randomly oriented, rotationally simetric scatterers.J. Quant. Spectrosc. Radiat. Transfer **1998** Vol. 60, No. 3, pp. 309-324.

[110] Draine, B. T. and Flatau, P. J., J. Opt. Soc. Am. A, **1994**, 11, 1491-1499.

[111] Kunz, K. S. and Luebbers, R. J., 1he Finite Difference 1ime Domain Method for Electromagnetics, CRC Press, Boca Raton, FL, **1993**.

[112] Antti Penttilaa, Evgenij Zubkoa, Kari Lummea, Karri Muinonena, Maxim A. Yurkin, Bruce Draine, Jussi Rahola, Alfons G. Hoekstra, Yuri Shkuratov.Comparison between discrete dipole implementations and exact techniques.Journal of Quantitative Spectroscopy Radiative Transfer. **2007**, 106, 417–436

[113] Forrest S, Witten Jr T. Long-range correlations in smoke-particle aggregates. J Phys A: Math General **1979**, 12(5), L109.

[114] Mackowski D, Mishchenko M. A multiple sphere t-matrix fortran code for use on parallel computer clusters. J Quant Spectrosc Radiat Transf **2011**;112(13):2182–92.

[115] Bohren C, Huffman D. Absorption and scattering of light by small particles. New York: John Wiley Sons; **2008**.

[116] Dobbins R, Megaridis C. Absorption and scattering of light by polydisperse aggregates. Appl Opt **1991**, 30(33), 4747–54.

[117] Waterman P. Matrix formulation of electromagnetic scattering. Proceedings of the IEEE **1965**, 53, 805-812

Chapter 3

Elements of Computational Quantum Chemistry

Molecular modelling is a collective term that refers to theoretical methods and computational techniques to model or mimic the behaviour of molecules. These techniques are used in the fields of computational chemistry, computational biology and materials science for studying molecular systems ranging from small chemical systems to large biological molecules and material assemblies.

A frequently used distinction is to divide molecular modelling techniques into molecular graphics and computational chemistry:

Molecular graphics provides for the visualization of molecular structures and their properties: ability to display structures in a variety of styles, with visual aids to move the structures interactively in 3D. The graphics part of the modelling system also provides an interface to the computational chemistry tools, allowing calculations to be defined and run and then analyzed when complete.

Computational chemistry carry out calculation of stable structures and properties, by using:

i) Molecular Mechanics (MM): a classical approach to calculate the energy of a structure. The molecule is treated essentially as a set of charged point masses (the atoms) which are coupled together with springs. It provides no information on the electronic structure.

ii) Quantum Mechanics (QM): Starting with a specified nuclear geometry, quantum mechanics calculations concern the resolution of Time-Independent Schrödinger Equation (TISE) for this arrangement of nuclei. This yields

both the energy of the molecule and the associated wave function from which electronic properties, such as electron density, can be calculated.

In this chapter, the reader will find some basic concepts of the formalism of computational chemistry. However, the interest is not to enter into the details of this subject but rather to establish a clear framework for a correct understanding of the simulations developed along this PhD thesis work. The results will be discussed in the next chapter. For a better understanding of this techniques, I recommend a series of books and research papers [1, 2, 3].

3.1 General problem

The ultimate goal of most quantum chemical approaches is the solution of the time-independent, non-relativistic Schrödinger equation (TISE)

$$\hat{H}\Psi_i(\vec{x}_1, \vec{x}_2, \cdots, \vec{x}_N, \vec{R}_1, \vec{R}_2, \cdots, \vec{R}_M) = E_i\Psi_i(\vec{x}_1, \vec{x}_2, \cdots, \vec{x}_N, \vec{R}_1, \vec{R}_2, \cdots, \vec{R}_M) \tag{3.1}$$

where $\hat{H}$ is the Hamiltonian operator for a molecular system consisting of M nuclei and N electrons in the absence of magnetic or electric field. $\hat{H}$ is a differential operator representing the total energy:

$$\hat{H} = -\frac{1}{2}\sum_{i=1}^{N}\nabla_i^2 - \frac{1}{2}\sum_{A=1}^{M}\frac{1}{M_A}\nabla_A^2 - \sum_{i=1}^{N}\sum_{A=1}^{M}\frac{Z_A}{r_{iA}} + \sum_{i=1}^{N-1}\sum_{j>1}^{N-1}\frac{1}{r_{ij}} + \sum_{A=1}^{M-1}\sum_{B>A}^{M-1}\frac{Z_A Z_B}{R_{AB}} \tag{3.2}$$

Here, A and B run over the M nuclei while i and j denote the N electrons of the system. The first two terms describe the kinetic energy of the electrons and nuclei respectively, where the Laplacian operator ∇_q^2 is defined as a sum of differential operators (in cartesian coordinates)

$$\nabla_q^2 = \frac{\partial^2}{\partial x_q^2} + \frac{\partial^2}{\partial y_q^2} + \frac{\partial^2}{\partial z_q^2} \tag{3.3}$$

and M_A is the mass of nucleus A (expressed in multiples of the mass of an electron when using atomic units). The remaining three terms define the potential energy of the Hamiltonian and represent the attractive electrostatic interaction between the nuclei and the electrons and the repulsive potential due to the electron-electron and nucleus-nucleus interactions, respectively.

$$\hat{H} = T_{el} + T_{Nu} + V_{Nu-el} + V_{el-el} + V_{Nu-Nu} \tag{3.4}$$

The r_{pq} term (and similarly R_{pq}) is the distance between the particles p and q, i.e., $r_{pq} = |\vec{r}_p - \vec{r}_q|$ and $\Psi_i(\vec{x}_1, \vec{x}_2, \cdots, \vec{x}_N, \vec{R}_1, \vec{R}_2, \cdots, \vec{R}_M)$ stands for the wave function of the ith state of the system, which depends on the $3N$ spatial coordinates $\{\vec{r}_j\}$, and the N spin coordinates $\{S_j\}$ of the electrons, which are collectively termed $\{x_j\}$ and the $3M$ spatial coordinates of the nuclei, $\{\vec{R}_I\}$. The wave function Ψ_i contains all information that can possibly be known about the quantum system at hand. Finally, E_i is the numerical value of the energy of the state described by Ψ_i.

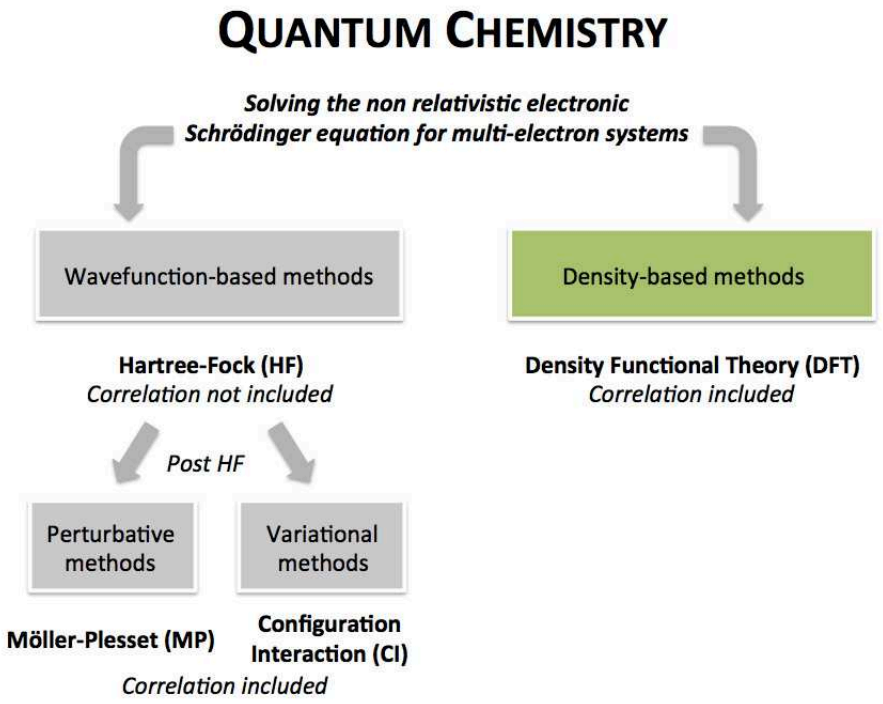


Figure 3.1: Quantum chemistry framework.

This Hamiltonian operator contains a large number of terms even for a system as simple as one water molecule. This 10-electron and 3-nucleus system leads to 13 kinetic terms, 30 electron-nucleus attractive potential terms, 45 electron-electron repulsive potential and 3 nucleus-nucleus potential terms. At the end, we would have to take into account 91 terms to solve the TISE, even for such a simple system !

A way to make this task easier relies on the fact that the two sets of variables, electronic coordinates and nuclei coordinates do not have the same status.

Even for the lightest nucleus, the proton ^1H , the mass is roughly 1800 larger than the mass of an electron. For a nucleus like carbon, the mass ratio well exceeds 20,000. Since both particles experience the same kind of forces (Coulombic in nature), the nuclei move much slower than the electrons.

The practical consequence of this fact is that we can (at least in most of the situations) take the extreme point of view and consider the electrons as moving in the field of fixed nuclei. Indeed, the kinetic energy is vanishingly small and then the potential energy due to nucleus-nucleus repulsion is merely a constant.

Thus, the complete Hamiltonian given in equation 3.2 reduces to the so-called electronic Hamiltonian

$$\hat{H}_{el} = T_{el} + V_{Nu-el} + V_{el-el} \tag{3.5}$$

Then, the eigenvalues U_k of the Schrödinger electronic equation:

$$\hat{H}_{el}\Psi_k(\vec{x}_1, \vec{x}_2, \cdots, \vec{x}_N, \vec{R}_1, \vec{R}_2, \cdots, \vec{R}_M) = U_k\Psi_k(\vec{x}_1, \vec{x}_2, \cdots, \vec{x}_N, \vec{R}_1, \vec{R}_2, \cdots, \vec{R}_M) \tag{3.6}$$

depend on the nuclei coordinates since this equation is solved for all the geometries of the molecular system. They are considered as a potential averaged over the electronic motions. They form what we call the set of potential energy surfaces (**PES**) which will be used in a second step as potential terms in a Schrödinger equation for the motion of the nuclei (rotation, vibration and of course reactivity), With this notation, U_1 denotes the lowest PES of the molecule.

This resolution in two steps is an approximate way to solve the TISE due to Born and Oppenheimer [4]. It is called the Born-Oppenheimer (BO) approximation or the Born-Oppenheimer separation. This is in mathematics a classical procedure to solve differential equations with two sets of variables of which the range and the speed of variation are very different. We solve the problem of the fast variables first and then use the solutions of this first set to determine the solutions of the second set. Of course, the method leads to approximate solutions since it always remains some couplings between the two sets of variables. This resolution can be improved by taking into account explicitely the coupling between the two sets. In this case we use what we call calculations beyond the BO approximation.

3.1.1 The Variation Method

The analytical resolution of the Time-Independent Schrödinger Equation (TISE) can only be performed exactly for some specific one-particle problems like the particle in a box, the harmonic oscillator or the rigid rotor. As long as we have to deal with polyelectronic systems the presence of electron-electron repulsion terms in the Hamiltonian operator prevents analytical resolution of TISE. Only numerical solutions are accessible within a reasonable computing time.

To perform calculations governed by a numerical convergence with respect to given experimental data, it is important to get a convenient criterion of convergence.

Such a criterion is usually based on the total energy of the system. Indeed, the variation theorem states that given a system described by a time-independent Hamiltonian, then for any Ψ normalized well-behaving (continuous everywhere and quadratic integrable) trial function that satisfies the boundary conditions of the problem, it can be demonstrated, by expanding Ψ in terms of the set of orthonormalized eigenfunctions of $\hat{H}$, that

$$W \equiv \int_{Dq} \Psi^*.H.\Psi d\tau \geq E_0 \tag{3.7}$$

where E_0 is the ground-state energy and Dq is the integration domain of the variables q of the problem.

In other words, W is always larger than E_0, the equality being satisfied only when $\Psi = \Psi_0$ is the exact solution of the ground state of the system i.e., when Ψ_0 is eigenvalue of $\hat{H}$ associated with the eigenvalue E_0 : $\hat{H}\Psi_0 = E_0\Psi_0$.

The variation method associated with this theorem is the method to find the best functional which leads to $W = E_0$. When I write the best functional and not the best function, I claim the best function in nature, not the best function of a given kind. Pratically, this research is out of range. Then, the best functional is replaced by the best function of a given type. To do that, a set of flexible parameters is introduced in Ψ (flexible means that they can vary) and we find the best set of parameters which leads to the lowest value of the variational integral W. When this minimization is achieved, we have obtained the best function of the type chosen. However, the energy W is always an upper limit of E_0 due to the variation theorem.

A priori, the variation theorem concerns only the energy of the ground state of the system or at the very most, the lowest state of a given symmetry. The

use of a trial function which depends only on linear parameters increases fantastically the power of this method, since we are now able to get an upper limit of all the states of the system, not only the lowest one (Mc Donald's theorem [5]).

Let see how it works. The trial function Ψ_{trial} is now expressed as a linear combination of n independent well-behaving functions f_i as:

$$\Psi_{trial} = \sum_{i=1}^{n} c_k f_i \tag{3.8}$$

The parameters are the coefficients c_k. The best representation of the electronic wavefunction describing the n^{th} state of the system, is given by the minimization of the variational integral according to :

$$\frac{\delta W}{\delta c_k} = 0 \qquad k = 1, \ldots, n \tag{3.9}$$

This minimization leads to a set of n linear homogeneous equations with the unknown coefficients $c_1, \ldots, c_n$

$$\sum_{k=1}^{n} [H_{ik} - S_{ik}W]c_k = 0 \qquad k = 1, \ldots, n \tag{3.10}$$

with

$$H_{ik} = \langle f_i^* | H | f_k \rangle \quad and \quad S_{ik} = \langle f_i^* | f_k \rangle \tag{3.11}$$

To get a nontrivial solution of this set of n linear homogeneous equations, the determinant built on the coefficients c_k of this set should vanish. We get a polynomial equation of n^{th} degree in W (often called the secular equation) which has n real roots $W_0 \leq W_1 \leq W_2 \leq \cdots \leq W_{n-1}$.

$$det(H_{ik} - S_{ik}W) = 0 \tag{3.12}$$

The n roots of this equation are upper bonds for the true energies $E_0, \ldots, E_{n-1}$ of the n lowest states [5]:

$$E_0 \leq W_0, E_1 \leq W_1, \ldots, E_{n-1} \leq W_{n-1} \tag{3.13}$$

and having found the roots W_k, we substitute them one at a time into the set of equations, which we then solve to get the c's. In fact, we get only $n-1$ linearly independent equations (if there is no degeneracy between the W_k) which lead to the ratio of each coefficient c_i over for instance c_0. The normalization of the wavefunction is the n^{th} relation which allows to determine all the coefficients. For each root W_k, we find a set of coefficients $c_1(k), \ldots, c_n(k)$. Finally, the use of these n sets of coefficients in the expression of Ψ provides approximate wave functions for the n lowest states.

3.2 Ab initio methods

3.2.1 General presentation

As shown in 3.1, computational chemistry is based on different quantum-chemical methods that aim at solving the molecular Schrödinger equation associated with the molecular Hamiltonian. Methods that do not include any empirical or semi-empirical parameters in their equations, being derived directly from theoretical principles, with no inclusion of experimental data are the so called *ab initio* methods.

Practically it is impossible to solve equation 3.9 by searching through all acceptable N-electron wave functions. Then, we need to define a suitable subset, which offers a physically reasonable approximation to the exact wave function without being unmanageable in practice.

In the Hartree-Fock scheme (HF) the simplest, yet physically sound approximation to the complicated many-electron wave function is used. It consists of approximating the real N-electron wave function by an antisymmetrized product of N one-electron wave functions $\chi_i(\vec{x}_i)$ in order to obey the Pauli principle. This product is usually referred to as a Slater determinant, Ψ_{SD} (strictly speaking, this statement applies only to closed-shell systems of non-degenerate point group symmetry, otherwise the wave function consists of a linear combination of a few Slater determinants):

$$\Psi_0 \approx \Psi_{SD} = \frac{1}{\sqrt{N!}} \begin{vmatrix} \chi_1(\vec{x}_1) & \chi_2(\vec{x}_1) & \cdots & \chi_N(\vec{x}_1) \\ \chi_1(\vec{x}_2) & \chi_2(\vec{x}_2) & \cdots & \chi_N(\vec{x}_2) \\ \vdots & \vdots & \ddots & \vdots \\ \chi_1(\vec{x}_N) & \chi_2(\vec{x}_N) & \cdots & \chi_N(\vec{x}_N) \end{vmatrix} \tag{3.14}$$

where the one-electron functions $\chi_i(\vec{x}_i)$ are called spin orbitals, and are composed of a spatial orbital $\psi_i(r)$ and one of the two spin functions, $\alpha(s)$ or $\beta(s)$.

$$\chi(\vec{x}) = \psi(\vec{r})\sigma(s) \qquad \sigma = \alpha, \beta \tag{3.15}$$

The research of the best Slater determinant corresponds to the research of the best spin orbitals i.e. the best spatial functions $\psi(\vec{r})$ which minimize the variational integral :

$$W =< \Psi_{SD}|H|\Psi_{SD} > . \tag{3.16}$$

When the minimum of W is reached, $W_{min} = E_{HF}$ and it is called the Hartree-Fock limit.

Practically, the optimum spin-orbitals $\chi(\vec{r})$ must satisfy the so-called Hartree-Fock equations

$$\hat{f}\chi_i = \varepsilon_i\chi_i \qquad i = 1, 2...N \tag{3.17}$$

These N equations have the appearance of an eigenvalue problem, where ε_i are the eigenvalues of the operator $\hat{f}$.

The ε_i have the physical interpretation of orbital energies and the Fock operator $\hat{f}$ is an effective one-electron operator defined as:

$$\hat{f}_i = -\frac{1}{2}\nabla_i^2 - \sum_{A=1}^{M}\frac{Z_A}{r_{iA}} + V_{HF}(i) \tag{3.18}$$

The first two terms are the kinetic energy and the potential energy due to the electron-nucleus attraction. $V_{HF}(i)$ is the Hartree-Fock potential. It is the average repulsive potential experienced by the i^{th} electron due to the remaining $N-1$ electrons. Thus, the two-electron repulsion operator $1/r_{ij}$ in the Hamiltonian is replaced by the one electron operator $V_{HF}(i)$ where the electron-electron repulsion is taken into account only in an average way (mean field approximation). Explicitly, V_{HF} has the following two components:

$$V_{HF}(\vec{x}_1) = \sum_{j}^{N}(2\hat{J}_j(\vec{x}_1) - \hat{K}_j(\vec{x}_1)) \tag{3.19}$$

where $\hat{J}$ is the Coulomb operator and represents the potential that an electron at position $\vec{x}_1$ experiences due to the average charge distribution of

another electron in spin orbital χ_j and $\hat{K}$ is the exchange operator who has no classical interpretation (consequence of the Pauli principle) defining the electron exchange energy due to the antisymmetry of the total N-electron wave function.

We see from these definitions that $\hat{f}$ actually depends on the wavefunctions of all the electrons. To proceed, we have to guess the initial form of the wavefunctions, use them to express the Coulomb and exchange operators, and solve the Hartree-Fock equations. That process is then continued using the newly found wavefunctions until each cycle of calculation leaves the energies and wavefunctions unchanged to within a chosen criterion. This is the origin of the term self-consistent field (SCF) for this type of procedure.

In 1929, Hartree with the help of his father performed numerically (by hand) this procedure for the Helium atom. Making the assumption that average electronic self-consistent field is expected to be radial, the spatial orbitals are now written as a product of a spherical harmonic function (well known functions in Mathematics) by a radial function. The 3D atomic problem is now reduced to the determination of a function of r.

However the molecular problem cannot be solved in this way. In 1951 Roothaan proposed a method [7, 8], now called Hartree-Fock-Roothaan (HFR), in which the molecular orbitals are developped linearly in a finite basis set of Q selected a priori monoelectronic functions χ_p:

$$\psi_i = c_{i1}\chi_1 + c_{i2}\chi_2 + \cdots + c_{iQ}\chi_Q = \sum_{p=1}^{Q} c_{ip}\chi_p \tag{3.20}$$

which when put into Eq. 3.17 gives the well known Roothaan equations:

$$FC = SC\varepsilon \tag{3.21}$$

where F and S are the matrices which represent respectively the Fock operator f and the so-called overlap matrix S, both in the basis $\{\chi_p\}_Q$.

Finally, it is interesting to mention the Koopmans theorem (Koopmans, 1934) which gives some physical interpretation of the energy ε_{HOMO} of the highest occupied molecular orbital (HOMO).

This theorem states that this orbital energy ε_{HOMO} is a good approximation of the first ionization energy IE_1 of the system : $-\varepsilon_{HOMO} \approx IE_1$. How can we justify this property ?

The first ionization energy IE_1 of a molecule M (or an atom) is the difference between the energy of the ion M^+ and the energy of M : $IE_1 = E_{M^+} - E_M$. If we admit i) that the quantity E_M can be estimated realistically by the Hartree-Fock method and ii) that the quantity E_{M^+} calculated as E_M but from the Slater determinant $(N-1)\times(N-1)$ obtained from the determinant $N \times N$ in which the row associated with the HOMO and the N^{th} column corresponding to the N^{th} electron have been removed. From this calculation, it is easy to prove that $IE_1 \approx E_{(HF,M),M^+} - E_{HF,M} = \varepsilon_{HOMO}$.

We see that two levels of approximations are introduced : i) we assume that the HF energy of M is the true energy and ii) we assume the HF MO of M^+ are the same as those of M. In spite of these crude approximations, the agreement between theory and experience is quite acceptable.

Thus, the main difference between the exact energy E_0 of the electronic wavefunction (non relativistic) and the E_{HF} remains in the size of the basis set introduced in 3.20 and the effect of the electronic correlation energy term E_{corr} introduced in the HF formalism because the exact function describing the ground state of an atomic or molecular system cannot be expressed by a Slater determinant, i.e., as an antisymmetrized product of monelectronic functions. In other words, the Slater determinant is only the exact wave function of N non-interacting particles moving in the field of the effective potential V_{HF}.

However, in the context of traditional wave function based *ab initio* quantum chemistry a large variety of computational schemes have been developed to evaluate the correlation energy. Here, we only mention the two important families of this kind of refined post Hartree-Fock schemes : a perturbative method through the Moller-Plesset scheme and a variation approach : the Configuration Interaction method (CI). Of course, these methods are more accurate than the HF approach but they are rather time consuming. Moreover, they become difficult to use conveniently when dealing with systems containing a large number of atoms, namely, more than 100.

3.2.2 The Restricted and Unrestricted Hartree-Fock Models

Frequently we are dealing with systems having an even number of electrons paired to give an overall singlet, so-called closed shell systems. The vast majority of all normal compounds, such as water, methane or most other ground state species in organic or inorganic chemistry, belongs to this class. In these instances the Hartree-Fock solution is usually characterized by having doubly occupied spatial orbitals, i. e., two spin orbitals χ_p and χ_q share the same spatial orbital ψ_p connected with an α and a β spin function, respectively, and have the same orbital energy. If we impose this double

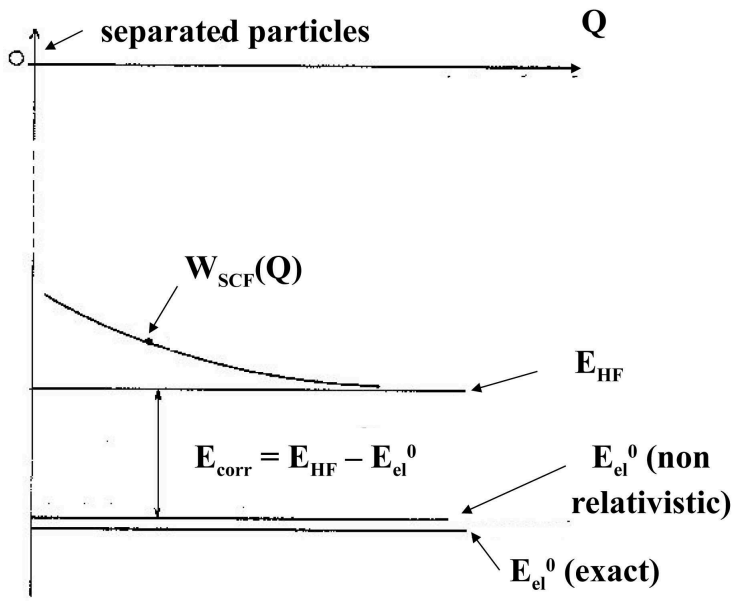


Figure 3.2: HFR main approximation

occupancy right from the start, we arrive at the restricted Hartree-Fock approximation, RHF for short.

Situations where the RHF picture is inadequate correspond to any system containing an odd number of electrons or systems with an even number of electrons, but where not all of these electrons occupy pairwise spatial orbital, i. e., open-shell situations, such as the triplet ground states of methylene, CH_2 ($\widetilde{X}^3B_1$), or of the oxygen molecule ($X^3\Sigma_g^-$).

There are two possibilities for treating such species within the Hartree-Fock approximation. Either we stay as close as possible to the RHF picture and doubly occupy all spatial orbitals with the only exception being the explicitly singly occupied ones, or we completely forgot the notion of doubly occupied spatial orbitals and allow each spin orbital to have its own spatial part. The former is the restricted open-shell HF scheme (ROHF) while the latter is the much more popular unrestricted Hartree-Fock variant (UHF). In UHF the α and β orbitals do not share the same effective potential but experience different potentials, V_{HF}^{α} and V_{HF}^{β}. As a consequence, the α and β orbitals differ in their spatial characteristics and have different orbital energies. The UHF scheme affords equations that are much simpler than their ROHF counterparts.

Particularly, the ROHF wave function is usually composed not of a single Slater determinant, but corresponds to a limited linear combination of a few

determinants where the expansion coefficients are determined by the symmetry of the state. On the other hand, in the UHF scheme we are always dealing with single-determinantal wave functions. However, the major disadvantage of the UHF technique is that unlike the true and also the ROHF wave function, a UHF Slater determinant is no longer an eigenfunction of the total spin operator $\hat{S}^2$. The more the $\langle \hat{S}^2 \rangle$ expectation value of a Slater determinant deviates from the eigenvalue, i. e., $S(S+1)$ where S is the spin quantum number representing the total spin of the system, the more this unrestricted determinant is contaminated by functions corresponding to states of higher spin multiplicity. Note that it is also possible to project the UHF function on the eigenfunctions of S^2 to get the proper spin components and calculate their energy.

3.3 DFT

A technique that has gained considerable ground in recent years to become one of the most widely used technics for the calculation of molecular structure is density functional theory (DFT). Its advantages include less computational time, and, in some cases (particularly d-metal complexes), better agreement with experimental values than from Hartree-Fock procedures.

The central focus of DFT is the electron density, ρ, a function of only 3 spatial coordinates, rather than the wavefunction Ψ, a function of $4N$ coordinates for a N-electron system. The functional part of the name comes from the fact that the energy of the molecule is a function of the electron density, written E[ρ], and the electron density is itself a function of position, $\rho(r)$, and in mathematics a function of a function is called a functional. The exact ground-state energy of an N-electron molecule is

$$E[\rho] = E_K + E_{p,el-nu} + E_{p,el-el} + E_{xc}[\rho], \tag{3.22}$$

where E_K is the total electron kinetic energy, $E_{p,el-nu}$ the electron-nucleus potential energy, $E_{p,el-el}$ the electron-electron potential energy, and $E_{xc}[\rho]$ the exchange-correlation energy, which takes into account all the effects due to spin. The orbitals used to construct the electron density from

$$\rho(r) = \sum_{i=1}^{N} |\psi_i(r)|^2, \tag{3.23}$$

are calculated from the Kohn–Sham equations, which are found by applying the variation theorem to the electron energy, and looks like the Hartree-Fock

equations except for a term V_{XC}, which is called the exchange-correlation potential:

$$\left(-\frac{1}{2}\nabla^2 + \left[-\sum_{A=1}^{M}\frac{Z_A}{r_{iA}} + \int\frac{\rho(\vec{r}_2)}{r_{12}}d\vec{r}_2 + V_{xc}(\vec{r}_1)\right]\right)\psi_i = \varepsilon_i\psi_i \quad i = 1,\ldots,N, \tag{3.24}$$

where the exchange–correlation potential is the functional derivative of the exchange–correlation energy:

$$V_{xc} = \frac{\delta E_{xc}(\rho)}{\delta\rho}. \tag{3.25}$$

The KS equations can be written with an effective potential, leading to one-particle equations where V_{KS} is the one-particle KS potentia, solution ofl:

$$\left(-\frac{1}{2}\nabla^2 + V_{ks}(\vec{r}_1)\right)\psi_i = \varepsilon_i\psi_i \quad i = 1,\ldots,N. \tag{3.26}$$

In other words, we deal with a set of N non-interacting particles moving in an effective potential V_{KS} which is the sum of the Hartree-Fock potential, the external potential and the exchange-correlation potential:

$$V_{ks} = \int\frac{\rho(\vec{r}_2)}{r_{12}}d\vec{r}_2 - \sum_{A=1}^{M}\frac{Z_A}{r_{iA}} + V_{xc} = V_{hf} + V_{ext} + V_{xc}. \tag{3.27}$$

Note that the non local exchange operator $\hat{K}$ of eq 3.18 in the HF method has been now replaced by the local exchange correlation potential V_{xc}. Nevertheless, the two approaches HF and KS provide one-electron equations for describing a polyelectronic system.

As in the HF method the Kohn–Sham equations are solved iteratively and self-consistently. Departing with a guessed electron density the exchange-correlation potential is calculated by assuming an approximate form of the dependence of the exchange–correlation energy on the electron density and evaluating the functional derivative in eq 3.25. Then, the Kohn–Sham equations are solved to obtain an initial set of orbitals. Then this set of orbitals is used to obtain a better approximation to the electron density from eq 3.23 and the process is repeated until the density and the exchange–correlation energy are constant to within a priori given tolerance.

Strictly speaking the KS orbitals do not have any physical significance. Similarly the KS eigenvalues ε_i do not have strict physical meaning, except the energy of highest occupied KS orbital which is still an estimation of minus the ionization energy. As in HF theory, the total electronic energy is not the sum of the orbital energies ε_i.

It is important to stress that if the exact form of E_{xc} and V_{xc} were known (which is unfortunately not the case) the KS approach would lead to the exact ground state energy since no approximation is introduced in the formalism. Then, the search for an accurate E_{xc} is still the greatest challenge of DFT.

3.3.1 Functionals

The local density approximation (LDA) is the basis of all approximate exchange-correlation functional. LDA makes use of the uniform electron gas model defined by a constant electron density anywhere in a infinite volume.

This is a model in which electrons move on a positive charge distribution (positive cores) such that the total ensemble is electrically neutral. The central idea of LDA is to write the E_{xc} functional as:

$$E_{xc}^{LDA}[\rho] = \int \rho(\vec{r})\varepsilon_{xc}(\rho(\vec{r}))d\vec{r}, \tag{3.28}$$

where $\varepsilon_{xc}(\rho(\vec{r}))$ represents the exchange-correlation energy per particle of an uniform electron gas of density ρ. Indeed, the energy per particle is weighted by the probability $\rho(\vec{r})$ that there is an electron at position r. Then, the energy per particle ε_{XC} can be further split into exchange and correlation contributions taking the exchange part functional derived from the Slater approximation but with the inconvenient that no such explicit expression is known for the correlation part. Thus, to solve this problem several authors have proposed analytical expressions based on interpolation/parameterization schemes.

The LDA is a very drastic approximation for atomic and molecular systems where the density is certainly not constant. Despite this fact, LDA approximation is surprisingly not so bad to reproduce some molecular properties such as equilibrium structures, harmonic frequencies, charges and dipole moments. Its main failure is that LDA often gives overestimated values of bond energies or atomic ionization energies.

A rational step to go beyond the LDA is to use, not only the density $\rho(r)$ at a particular point r but also the gradient of the charge density in order to

account for the non-homogeneity of the true electron density. This is what we call the generalized gradient approximation (GGA).

In the GGA framework, the exchange terme (x) of the E_{xc} functional is defined as:

$$E_x^{GGA}[\rho] = E_{xc}^{LDA}[\rho] - \int \rho(\vec{r})F(s)(\rho^{\frac{4}{3}}(\vec{r}))d\vec{r}, \tag{3.29}$$

where the s variable has to be understood as a local inhomogeneity parameter that assumes large values not only for large gradients, but also in regions of small densities, such as the exponential tails far from the nuclei.

$$s(\vec{r}) = \frac{|\nabla\rho(\vec{r})|}{\rho^{\frac{4}{3}}(\vec{r})}. \tag{3.30}$$

Some well known and widely used examples of the function F was proposed by Becke in 1988 (B88) [9] with the parameter $\beta = 0.0042$ fitted on exact HF exchange calculations on rare gas atoms:

$$F = \frac{\beta s^2}{1 + 6\beta s\ sinh^{-1}s}. \tag{3.31}$$

Following the same idea, hybrid functionals incorporate some exact (Hartree-Fock) exchange as:

$$E_x^{HYB} = aE_x^{HF} + (1-a)E_x^{GGA}. \tag{3.32}$$

Specifically in this class we found the most popular and multireferenced, in recent years, B3LYP functional from A.D. Becke [10].

$$E_{xc}^{B3LYP} = aE_x^{HF} + (1-a)E_x^{GGA} + bE_x^{B88} + cE_c^{LYP} + (1-c)E_c^{LDA}, \tag{3.33}$$

where a, b, and c are semi-empirical coefficients fitted to reproduce experimental atomization and ionization energies.

3.4 Basis set

In modern computational chemistry, quantum chemical calculations are typically performed using a finite set of basis functions composed of a finite number of atomic orbitals, centered at each atomic nucleus within the molecule.

$$\psi_i(r) = \sum_{p=1}^{Q} c_{ip}\chi_p(r). \tag{3.34}$$

These atomic orbitals $\chi_p(r)$ are well described with Slater-type orbitals (STOs), since STOs decay exponentially with distance from the nuclei, describing the long-range overlap between atoms, and reaching a maximum at the nucleus. However, STOs are not convenient for evaluating multicenter integrals.

Happily, it was later realized that these Slater-type orbitals could in turn be approximated as linear combinations of Gaussian orbitals. This led to huge computational time saving and a considerable advance for the implementation and use of modern softwares, because the use of Gaussian-type orbitals (GTOs) ensures analytical solutions for all integrals appearing in HF method.

In this section the reader can find some support information to become familiar with the general nomenclature used in the next chapter for the atom basis set employed.

Moreover, as all calculations were performed with the Gaussian09 package I present some examples of the Gaussian basis set proposed by Pople and Dunning.

The notation for the split-valence basis sets arising from the group of John Pople [11] is:

$$N - n_1 n_2 + G(x), \tag{3.35}$$

where core orbitals (first term) are described by one contracted function (GTO) developed over N primitive Gaussian functions as:

$$AO(core) = GTO = \sum_{i=1}^{N} a_i \chi_i^G. \tag{3.36}$$

Afterward, valence orbitals are composed of two basis functions GTO_1 and GTO_2 developed over n_1 and n_2 primitive Gaussian functions respectively:

$$AO(valence) = c_1 GTO_1 + c_2 GTO_2 = c_1 \sum_{i=1}^{n_1} a_i \chi_i^G + c_2 \sum_{i=1}^{n_2} b_i \chi_i^G. \quad (3.37)$$

In addition, we can add polarization functions that enable to describe molecules with a charge flow between atoms having different electronegativities. Thus, writing (d,p) instead (x) in eq. 3.35 set d orbitals on all non hydrogen atoms and p orbitals added on all hydrogen atoms. The + symbol add diffuse functions required for an accurate description of the outermost part of the electronic density and therefore allows to reproduce properties associated with the less bound electrons.

Furthermore, correlation consistent (cc) polarized basis sets developed by Dunning [12] are one of the most widely used because they are designed to converge systematically to the complete-basis-set (CBS) limit using empirical extrapolation techniques. Valence (V) X-zeta orbitals are setting through the D(double) T(triple) and so on label.

$$aug - cc - pVXZ \quad (3.38)$$

Indeed, polarization functions are already included (p) while diffuse funtions can be added by using the keyword aug (augmented) or d-aug (double augmented).

In fig 3.3 an example of the pope basis set used to describe the acetonitrile molecule CH_3CN including diffuse and polarization effects is shown.

3.5 Conclusion

DFT is presently one of the most successful approach for electronic structure calculations due to a good computationally price/performance relation. Supported by the computer power increase and important developments in the accuracy of news exchange correlation functional, DFT has often replaced old semiempirical methods in electronic structure studies, becoming simulation of very large systems a reality. An important remark is that DFT is an exact theory and KS method is an exact way of doing it. Their performances comes from our choice of the $E_{xc}[\rho]$ potential.

GAUSSIAN BASIS SETS

Pople basis sets

Example: acetonitrile molecule CH_3CN

	core orbitals	*valence orbitals*
C	1s	2s, 2px, 2py, 2pz
C	1s	2s, 2px, 2py, 2pz
N	1s	2s, 2px, 2py, 2pz
H	/	1s
H	/	1s
H	/	1s
total	**3**	**15**

Polarized triple-zeta basis set with diffuses
6-311+G(d,p) – also noted 6-311+G**
1 contracted Gaussian func) on used per core orbital
3 contracted Gaussian func) ons used per valence orbital
5 *d* orbitals added on all non-hydrogen atoms
3 *p* orbitals added on all hydrogen atoms
3 *sp* orbitals added on all non-hydrogen atoms
$N_{basis} = 3\times1 + 15\times3 + 5\times3 + 3\times3 + 3\times3 =$ ***81 basis func%ons***

Figure 3.3: Example of Gaussian basis nomenclature.

Where DFT goes wrong? In multireference problems or highly correlated systems, because self-interaction corrections are rather difficult to implement in DFT. Another disadvantage is that basic DFT completely neglects dispersion interactions and functionals needs to be improved by empirical corrections, DFT-D, vdW-DF or RPA (Random phase approximation). Also, excited states cannot be found by DFT by usual methods, it requires time-dependent DFT (TDDFT).

Finally, I want to point out that, for all the above-mentioned reasions, to simulate the interaction of graphene surfaces with tropospherically relevant molecules and obtaining accurate results for the lowest energy state of the system, I have mainly used DFT rather than HF approaches during my PhD Work. Indeed, most of the time, DFT has guaranted a very good compromise between accuracy and computational cost.

Bibliography

[1] J.P. Lowe and K. Peterson, Quantum Chemistry, 3rd ed. Elsevier Academic Press 2006

[2] A. Szabo and N.S. Ostlund, Modern Quantum Chemistry, McGraw-Hill 1989, Dover 1996

[3] R.G. Parr, Quantum Theory of Molecular Electronic Structure, Benjamin 1963

[4] Max Born. J. Robert Oppenheimer. Annalen der Physik (in German) 389 (20): 457-484 (1927)

[5] MacDONALD, J. K. L. .Successive Approximations by the Rayleigh-Ritz Variation Method. Phys.Rev. 40;830:1933.

[6] D. R. Hartree.The Calculation of Atomic Structures. Repts. Progr. Phys. 1948;11;113

[7] C. C.J. Roothaan, Revs. Modern Phys. 1951;23; 69

[8] C.C.J.Roothaan.Self-Consistent Field Theory for open shells of electronic systems.Revs. Modern Phys. 1960,32,9.

[9] A. D. Becke, "Density-functional exchange-energy approximation with correct asymptotic-behavior," Phys. Rev. A, 38 (1988) 3098-100.

[10] A. D. Becke, Density-functional thermochemistry. III. The role of exact exchange. J. Chem. Phys.;1993,98:5648-52.

[11] Ditchfield, R.; Hehre, W.J.; Pople, J. A. Self-Consistent Molecular-Orbital Methods. IX. An Extended Gaussian-Type Basis for Molecular-Orbital Studies of Organic Molecules. J. Chem. Phys. 1971;54 (2): 724–728

[12] Dunning, Thomas H. Gaussian basis sets for use in correlated molecular calculations. I. The atoms boron through neon and hydrogen. J. Chem. Phys. 1989; 90 (2): 1007–1023

Chapter 4

First-Principle Study of the Interaction between NO, Cl, and HCl and Large Carbonaceous Clusters Modeling the Soot Surface

In this chapter first-principle calculations are performed to characterize the adsorption of NO, Cl, and HCl molecules on large carbonaceous clusters modeling the surface of soot. Possible adsorption on the face and on the edges of perfect and defective clusters is considered in the calculations. It is shown that the first situation corresponds to physisorption and requires taking into account long-range dispersion interactions in the calculations. In contrast, interaction of NO with the unsaturated edge of a defective cluster leads preferentially to a C-N rather than to a C-O chemical binding. This indicates that soot may be an efficient sink for NO in the troposphere only if it contains a high number of unsaturated carbon atoms. Similar calculations for Cl and HCl on defective carbonaceous surfaces are still in progress and only preliminary results will be presented here.

From a more fundamental point of view, this study also clearly evidences that quantum calculations have to be carefully conducted when considering the interaction between radical species and carbonaceous surfaces. Problems encountered with the choice of the functional used in density functional theory approaches as well as with the size of the basis set, spin multiplicity, and spin contamination have to be systematically addressed before any relevant conclusion can be drawn.

4.1 General problem

As already stated in the previous chapters, combustion-derived solid particles are suspected to have a non-negligible impact on the Earth's radiative balance by accounting for both a direct effect due to light absorption and an indirect effect because of their activation as ice and cloud condensation nuclei[1].

These particles, mainly made of carbon atoms, are currently one of the largest sources of uncertainties in understanding the fossil fuel burning impact on climate, mostly due to the high natural variability of their sources, conditions of combustion, and fuel compositions[2].

Widely accepted structural models for combustion carbonaceous particles assume the presence of graphene sheets, whose stacking on concentric spheres of different radii results in typical onion-like structures containing also other elements (mainly oxygen) besides carbon due to partial oxidation [3] and defects like edges or atom vacancies formed during the recombination of soot precursors[4]. Furthermore, characterizing the ability of these graphene sheets to trap water molecules and to promote chemical reactions, especially with atmospheric oxidants, is a preliminary step toward a better understanding of the impact of the particles emitted by engines on atmospheric chemistry and climate evolutions.

In a series of recent papers, the group in Besançon used theoretical approaches based on either classical simulation methods [5, 6, 7] or first-principle calculations [8, 9, 10, 11, 12, 13] to characterize the interaction between carbonaceous surfaces and surrounding molecules including water, polycyclic aromatic hydrocarbons (PAHs), and various atmospheric oxidants (atomic and molecular oxygen,ozone). The results of these studies have shown that pure and defective carbonaceous surfaces may chemically interact with the surrounding molecules, leading to the formation of oxygenated groups (mainly phenol, carbonyl, carboxyl, and ether-and epoxy-like groups) anchored at the surface that can participate in the hydrophilic behavior of soot together with specific structural characteristics such as pores of various sizes.

Although a wide variety of atmospheric molecules have been considered in these studies, the adsorption of nitrogen oxide species were not at all characterized. NO, N_2O, and, more generally, N_xO_y species are usually formed during high-temperature combustion of fuels and coals or electrical storms, and they are involved in several environmental problems, including stratospheric ozone depletion, the formation of acid rain, and climatic changes because they also act as greenhouse effect gases[14]. Depletion of these N_xO_y

species in the atmosphere occurs through a variety of processes, including nitrate aerosol formation, photo-chemical reactions, and also reduction on carbonaceous surfaces[15]. A thorough theoretical characterization of the interaction between nitrate oxides and the surface of soot is thus of great interest to better understand fundamental processes involved in atmospheric chemistry. Furthermore, several theoretical studies have been recently devoted to the interaction between nitrogen oxides and carbonaceous surfaces, most of them considering interactions with the unsaturated edges of carbon clusters [16, 17, 18] or with atom vacancies at the surface of graphite [19, 20] because the bare surface of carbon materials is expected to be less reactive[21].

Similarly, theoretical studies devoted to the characterization of the interaction between chlorinated (and, more generally, halogenated) species and large carbonaceous surfaces are very scarce and recent in the literature [22, 23, 24, 25, 26, 27]. This is surprising because the interaction of chlorinated species with soot surface is a quite old question, related to the transport of irritant gases into the lungs during/after combustion of polyvinyl chloride in domestic or industrial fires [28]. Indeed, it has been long inferred that smoke aerosols including soot could be particularly effective in transporting hydrogen chloride past the respiratory defenses [29]. More recently, experimental analyses have actually shown that small chlorinated species can be efficiently trapped at the surface of soot, and that they may even modify the hydrophilicity of soot [30].

Here, we have thus chosen to characterize the interaction between NO, Cl, and HCl, and carbonaceous clusters modeling the surface of soot because these species have not been considered much in the literature, at least from a theoretical point of view. Moreover, the few studies especially devoted to the adsorption of NO on a perfect carbonaceous surface (i.e., a surface without any defect) have led to significantly different results especially in terms of adsorption energies [31, 32, 33], the calculated values being in addition far from the heat of adsorption experimentally measured at low temperature on graphitized carbon (values between 2.9 and 4.3 kcal/mol)[34]. Indeed, while the strong interaction between NO and a defective carbonaceous surface is supposed to be well-described theoretically by standard quantum methods, the interaction with the surface of perfect carbonaceous surfaces is expected to be mainly governed by dispersion interactions leading to physisorption. The same assumption can also be made for the adsorption of HCl on perfect carbonaceous surfaces. Calculating such weak interactions is still challenging, and as a consequence, besides their atmospheric interests, the NO/soot and HCl/soot systems can also be used as test systems to compare various theoretical approaches.

The computational methods used in this work and the details of the calculations are briefly given in section 4.2.

The results are presented in section 4.3, and 4.4 and their atmospheric implications are discussed in section 4.3.3.

Finally, the main conclusions are summarized in section 4.5. Note that the results obtained in this PhD work for NO have been published in the Journal of Physical Chemistry A (C. Garcia-Fernandez, S. Picaud, M.T. Rayez, J.C. Rayez, and J. Rubayo-Soneira. First-Principles Study of the Interaction between NO and Large Carbonaceous Clusters Modeling the Soot Surface. J. Phys. Chem. A 2014; 118:1443-1450.) whereas a paper presenting the results for the chlorinated species is currently being written.

4.2 Computational details

Like in the previous papers[8, 9, 10, 11, 12], the soot surface has been modeled by large carbonaceous clusters, the edges of which are saturated by hydrogen atoms. These clusters will be referred as the C_nH_m clusters with $n = 24, 54, 96$, and 150 and the corresponding values for $m = 12, 18, 24, 30$ (see Fig 4.1).

Because adsorption on carbonaceous clusters can *a priori* occurs on faces or on edges of the clusters, we have analyzed both occurrences. Moreover, when considering adsorption on the edge of the clusters, defect sites frequently exist (even more than on the face). Here, we have modeled such defects by removing one hydrogen atom at the edge of the considered cluster, leaving thus one unsaturated bond at the surface.

In this work, I use quantum chemical calculations to characterize both the equilibrium structures of the adsorbed species at various sites of the carbonaceous surfaces and the binding energy of the adsorbed molecule that was defined as:

$$\Delta E_{ads} = E[C_nH_m - M] - E[C_nH_m] - E[M], \tag{4.1}$$

where $E[M]$ is the energy of the isolated species (M =NO, Cl or HCl), $E[C_nH_m]$ is the total energy of the optimized C_nH_m cluster in the absence of the adsorbate, and $E[C_nH_m - M]$ is the energy of the interacting system. The adsorption energy ΔE_{ads} accounts not only for the bonding energy but also for the energy difference coming from all possible structural changes (i.e.,deformation) of the carbonaceous cluster and of the molecule/radical upon adsorption.

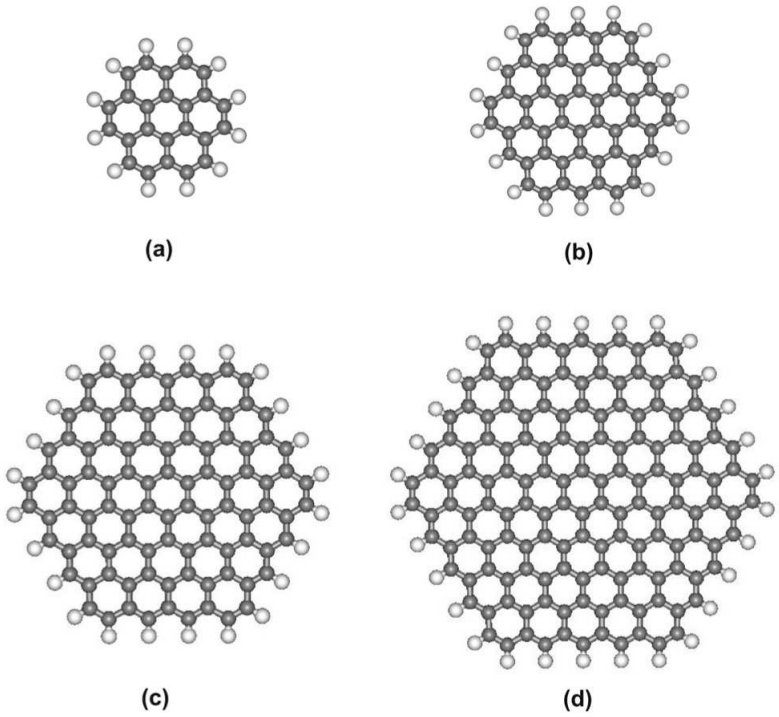


Figure 4.1: Structure of the various C_nH_m carbonaceous clusters considered in the present work.

Because adsorption of NO, Cl or HCl on C_nH_m clusters can involve both long-range forces if physisorption is the dominant effect and intermediate and short-range interactions if chemical bonds are created, I have decided to use density functional theory (DFT) involving different exchange-correlation functionals and taking into account long-range interactions. Then, I used the ωB97X-D functional[35], which is very appropriate to describe long-range dispersion forces (modeled by a London term) in addition to exchange-correlation effects[36].

The role of long-range forces will be analyzed by comparing the results obtained with this methodology and those provided by other functionals that do not contain any specific long-range term to describe dispersion effects, like the local spin density approximation (LSDA)[37], the hybrid B3LYP (Becke three-parameter, Lee, Yang, and Parr)[38]. Amazingly, it has been shown recently that LSDA seems able to describe more or less accurately the interaction of gas molecules with, for instance, carbon nanotubes[33, 39].

Thus, it has been interesting to check the validity of this assertion for the systems with which we are dealing. On the other hand, B3LYP is a well-known hybrid GGA (generalized gradient approximation) functional that

has been used to characterize the interaction of NO both with the face [31] and with the edges[16, 18] of carbonaceous systems. In the case of chlorinated species, I also used the half-and-half functional (BHandHLYP) [41] that has been proved in the literature to be well-suited for the characterization of Cl adsorption on benzene molecule [42].

Because the treatment of open-shell systems like the NO and Cl radicals considered here may require an unrestricted methodology (it is not of course the unique solution), spin contamination problems can occur because these systems may have numerous high-spin electronic states. Moreover, this spin contamination could considerably affect geometry optimization and the calculated adsorption energy on the surface[17].

To analyze the importance of such situations, I have used restricted open-shell DFT (RO-DFT), a method that does not allow, by definition, any spin contamination, in parallel with an unrestricted DFT approach[40]. It is interesting to note that the unrestricted DFT method was shown to have a much smaller spin contamination than *ab initio* unrestricted Hartree-Fock (UHF) approach[17]. Therefore, to complete these analyses, I have also compared the results obtained by DFT methods to those provided by standard *ab initio* molecular orbital (MO) open-shell methodologies like UHF, restricted open-shell Hartree-Fock (ROHF)[44], and the Møller-Plesset second-order (MP2) method that takes into account a part of the correlation energy[45].

Concerning now the basis sets used, the large number of atoms in the various C_nH_m clusters considered here leads to a selection of basis set sizes that represents a good compromise between accuracy and computational efficiency, even when dealing with 150 carbon atoms. Thus, the 6-31G, 6-31+G, 6-31G(d,p), and cc-pVDZ basis sets, were retained.

All of the calculations have been carried out by using the Gaussian 09 quantum chemistry package[46], and all stable geometries have been calculated with a tight criterion for geometry optimization.

4.3 Results for the adsorption of NO on carbonaceous surfaces

4.3.1 Adsorption of NO on the Face of Perfect Carbonaceous Clusters

We started this study by a detailed analysis of the adsorption characteristics of NO on the face of carbonaceous clusters without any defect.

The first series of calculations was performed using the $\omega B97X - D$ functional [35] that takes into account the dispersion effects in the calculation of the interaction energy between NO and the carbonaceous surface. The corresponding results are presented in Table 1 as a function of the size of the carbonaceous cluster and the basis set used. Note that because we have performed a full optimization of the NO-C_nH_m system, the adsorption geometry discussed below corresponds to the absolute minimum of the potential energy surface. The values displayed in Table 1 show that the optimized geometry of the NO-C_nH_m systems does not significantly depend on the size of the carbonaceous cluster or the basis set used in the calculations. In the corresponding equilibrium geometry (Figure 4.2-a), the NO radical is adsorbed nearly parallel to the carbonaceous surface, the N atom being slightly closer to the surface than the O atom (the tilt angle is equal to about 15° with respect to the carbon plane). In this position, the N and O atoms are located nearly above a C atom (top site) and above the center of a carbon hexagon (hollow site), respectively.

Table 1. DFT/ωB97X-D Binding Energies (kcal/mol) Calculated for NO Adsorbed on the Face of Various C_nH_m Clusters Using Three Different Basis Sets[a]

	$C_{24}H_{12}$	$C_{54}H_{18}$	$C_{96}H_{24}$	$C_{150}H_{30}$
6-31G	−2.94	−3.56	−3.7	−3.95
	N−C = 3.15 Å	N−C = 3.07 Å	N−C = 3.12 Å	N−C = 3.15 Å
	O−C = 3.38 Å	O−C = 3.28 Å	O−C = 3.32 Å	O−C = 3.27 Å
	N−O = 1.17 Å	N−O = 1.17 Å	N−O = 1.17 Å	N−O = 1.17 Å
cc-pVDZ	−3.02	−3.66	−3.75	−4.08
	N−C = 3.15 Å	N−C = 3.07 Å	N−C = 3.12 Å	N−C = 3.15 Å
	O−C = 3.31 Å	O−C = 3.28 Å	O−C = 3.32 Å	O−C = 3.25 Å
	N−O = 1.15 Å	N−O = 1.15 Å	N−O = 1.15 Å	N−O = 1.15 Å
6-31+G	−3.57	−4.55	−4.8	−5.05
	N−C = 3.13 Å	N−C = 3.05 Å	N−C = 3.10 Å	N−C = 3.13 Å
	O−C = 3.40 Å	O−C = 3.37 Å	O−C = 3.41 Å	O−C = 3.34 Å
	N−O = 1.17 Å	N−O = 1.17 Å	N−O = 1.17 Å	N−O = 1.17 Å

[a]Note that structural information has also been given in this table, namely, the N−C, O−C, and N−O distances.

The molecule-surface distance (N-C) is around 3.1 Å. In contrast, the adsorption energy increases (in absolute value) from 2.94 to 5.05 kcal/mol when increasing the size of the C_nH_m cluster and when changing the basis set. However, because the calculations for the $C_{150}H_{30}$ cluster are very time-consuming, especially when using the 6-31+G basis set that contains diffuse functions, the results given in Table 1 indicate that the $C_{54}H_{18}$ and $C_{96}H_{24}$ cluster could be a good compromise between accuracy and calculation time when characterizing adsorption on large carbonaceous systems such as those found in the soot structure.

The weak interaction between NO and the carbonaceous surface can be illustrated by a Mulliken analysis of the charge distribution. The values given in Table 2 clearly show that physisorption of NO is accompanied by a very weak charge transfer between the surface and the adsorbed molecule.

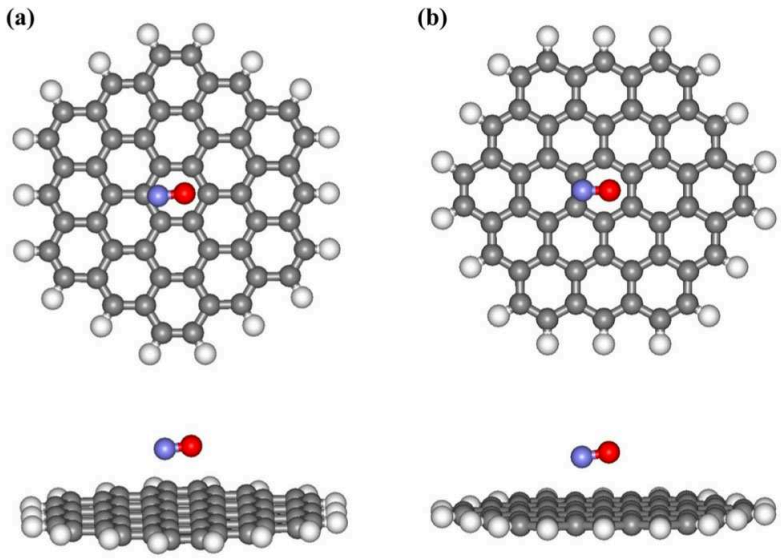


Figure 4.2: Optimized structures calculated for the adsorption of NO on the face of a $C_{54}H_{18}$ cluster using the 6-31G basis set and the (a) ωB97X–D or (b) LSDA functional. Both top and side views of the system are shown. N, O, C, and H atoms are represented by blue, red,gray, and white balls, respectively.

This charge transfer slightly modifies the charge distribution of the surface in the vicinity of the adsorption site, the atoms located far from this site being unaffected by adsorption.

When using the LSDA functional, that is, a DFT method that does not contain any specific long-range dispersion term, I calculate an adsorption energy value of about -6.7 kcal/mol for the $C_{54}H_{18}$ cluster with the 6-31G basis set. The NO radical is adsorbed nearly parallel to the carbonaceous cluster, as shown previously using the ωB97X-D functional, but the molecular center of the mass-surface distance is equal to about 2.8 Å instead of 3.1 Å, and the N atom is now adsorbed above the center of a C-C bond (see Figure 4.2b, associated with LSDA). In contrast, when using the B3LYP functional, the calculated adsorption energy is much weaker (about -0.3 kcal/mol), and the NO-surface distance is much larger (around 3.5 Å) than when using LSDA. Note that very similar results are obtained when using different basis sets (6-31G, 6-31+G, and cc-pVDZ). Moreover, as expected for these calculations on physisorbed systems, the spin contamination obtained when using the unrestricted DFT method remains very weak because the corresponding average (S^2) value is equal to at most $0.7553\hbar^2$, a value very close to the S^2 eigeinvalue $S(S+1)\ \hbar^2 = 0.75\ \hbar^2$.

Table 2. Mulliken Analysis of the Charge Distribution for the $NO/C_{54}H_{18}$ System before and after Adsorption[a]

atom type	before adsorption	after adsorption
N	0.166	0.157
O	−0.166	−0.169
C	−0.015	−0.011
C	−0.015	−0.018
C	−0.015	−0.017
C	−0.015	−0.021
C	−0.015	−0.026
C	−0.015	−0.022
C	0.014	0.015
C	0.014	0.016
C	0.014	0.017
C	0.014	0.020
C	0.014	0.017
C	0.014	0.016
C	−0.041	−0.041
C	−0.041	−0.041
C	−0.041	−0.041
C	−0.041	−0.040
C	−0.041	−0.040
C	−0.041	−0.040
C	−0.041	−0.040
C	−0.041	−0.041
C	−0.041	−0.041
C	−0.041	−0.041
C	−0.041	−0.040
C	−0.041	−0.040

[a]Calculations have been performed at the DFT level, with the ωB97X-D functional and the 6-31G basis set. Note that charges are given here for atoms located in the nearest vicinity of the adsorption site only.

These analyses are in agreement with the theoretical results already published in the literature [31, 33] and confirm that a functional like B3LYP is unable to give reasonable values for the adsorption energy of the NO/graphite-like system because the corresponding results are quite far from the experimental values (between −2.9 and −4.3 kcal/mol)[34]. In fact, as evidenced here, B3LYP strongly underestimates the binding energy, whereas the LSDA functional overestimates it, as already mentioned, for instance, in ref [47]. Note that the GGA functional [48] has also been shown to underestimate the adsorption energy (-0.7 kcal/mol) when compared to the experimental values[32].

To check the influence of structural defects on the NO adsorption, I have also performed additional calculations by considering a $C_{96}H_{24}$ cluster that contains one Stone-Wales defect [49] because such a defect has been shown

to strongly impact the adsorption of NO_2 on graphene, leading to the chemisorption of this molecule, accompanied by a significant change of the surface geometry upon adsorption[50]. A Stone-Wales defect consists of two pentagon-heptagon pairs in the hexagonal network and is one of the most frequently observed defective structures in carbon nanotubes and graphene[49].

However, calculations performed here with the ωB97X-D functional still lead to a physisorption process, characterized by an adsorption energy value very close to that obtained on the perfect surface. This indicates that NO interacts weakly with the face of a carbonaceous surface, even when it contains a crystallographic defect. Such a feature is in fact similar to what has been evidenced for NH_3 and H_2CO interacting with a Stone-Wales defect on graphene and which has been related to the weak electron orbital overlap between these molecules and the defective surface[50, 51].

As a conclusion of this study on NO adsorption on the face of a carbonaceous cluster, the binding energy values obtained here with the ωB97X-D functional are consistent with the experimental data obtained at very low temperature and submonolayer coverage[34], irrespective of the cluster size considered in the calculations. This supports the hypothesis of a physisorption process for NO on C_nH_m clusters, mainly governed by the dispersion interactions. The approach used here thus represents a significant improvement compared to previous studies on similar systems.

Finally, it is important to mention that the optimization procedure for such systems was never an easy task, irrespective of the functionals and basis sets used. Indeed, due to the geometry of the carbonaceous surface and its weak interaction with NO, there are many nearly equivalent adsorption sites at the surface, characterized by small energy wells. As a consequence, the potential energy surface for NO appears very weakly corrugated, preventing thus a fast numerical minimum-energy search.

4.3.2 Interaction of NO with the Edge of Carbonaceous Clusters.

After considering adsorption of NO on the face of the C_nH_m clusters, I have also investigated the possible adsorption at the edges of the perfect carbonaceous clusters. However, starting from an initial position close to a cluster edge, the optimization procedure always leads ultimately to the adsorption of NO on the face of the cluster. Clearly, the presence of the H atoms appears to prevent adsorption of the NO radical at the edges of the carbonaceous cluster.

Then, I studied adsorption on a defective cluster created by removing one H atom, thus leaving one dangling bond at the cluster edge. For open-shell structures, I have performed calculations using the RO-DFT method with both RO-ωB97X-D and RO-B3LYP functionals and various basis sets. In addition, unrestricted DFT (U-ωB97X-D,U-B3LYP) calculations have also been performed to investigate the influence of spin contamination.

Table 3. Binding Energies (in kcal/mol) Calculated for NO Adsorbed at the Defective Edge of a $C_{54}H_{17}$ Cluster[a]

	$C_{54}H_{17}$–NO singlet			$C_{54}H_{17}$–ON triplet		
	DFT		ab initio	DFT		ab initio
	ωB97X-D	B3LYP	HF	ωB97X-D	B3LYP	HF
restricted and RO methods	−61.9	−59.3	−31.8	−30.0	−28.4	−34.9
unrestricted	−60.3	−58.8	−24.2	−33.3	−27.8	−27.1
($\langle S^2\rangle$ value for $C_{54}H_{17}$,	(0.78)	(0.76)	(1.33)	(0.78)	(0.762)	(1.33)
NO,	(0.752)	(0.752)	(0.93)	(0.752)	(0.752)	(0.93)
adsorbed system)				(2.00)	(2.009)	(2.07)

[a]The calculations have been performed with the 6-31G basis set, using restricted, RO, and unrestricted DFT and HF methods (depending on the situation; see the text). Two possible adsorption geometries have been considered in the calculations involving binding through either a C–N or a C–O bond (see the text). The spin contamination is illustrated by the $\langle S^2\rangle$ values, which are given in parentheses for the surface alone, the NO radical alone, and the adsorbed system.

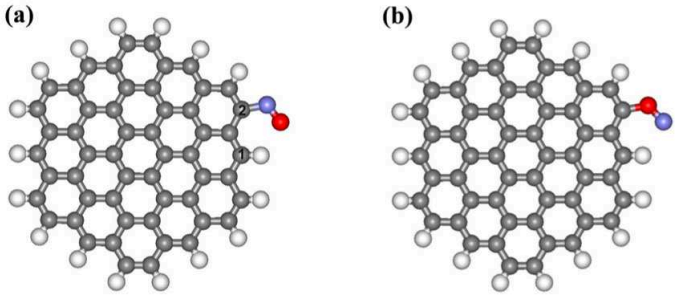


Figure 4.3: Optimized structures calculated with the DFT method for the chemisorption of NO on the edge of the defective $C_{54}H_{17}$ clusters using the 6-31G basis set and the ωB97X-D functional. Binding through either a C-N (a) or a C-O (b) bond is shown. N, O, C, and H atoms are represented by blue, red, gray, and white balls, respectively. The two different adsorption sites considered in the calculations see text are indicated by numbers 1 and 2 in the left panel.

The results obtained on the $C_{54}H_{17}$ cluster with the 6-31G basis set are given in Table 3, and the corresponding adsorption geometries are illustrated in Figure 4.3. Note that two different sites have been considered in the calculations corresponding to two different positions of the missing H atom at the edge (see Figure 4.3a), but the two situations lead to very similar results due to the symmetry of the carbonaceous cluster. These results show that NO strongly interacts with such a defective cluster, preferentially by forming a C-N (Figure 4.3a) rather than a C-O (Figure 4.3b) bond, the

corresponding binding energies being equal to about −60 kcal/mol in the first situation and around −30 kcal/mol in the second one, irrespective of the functional used. Indeed, calculations performed with ωB97X-D and B3LYP give very similar results, thus indicating that the dispersion effects do not play any significant role in the situations considered here. Moreover, spin contamination in these DFT calculations appears rather weak, as indicated by the S^2 values given in Table 3. Note that the adsorption of NO on the defective edge of the carbonaceous cluster is a barrierless process between two radicals, and no transition state has been searched along the reaction path.

Moreover, it is also interesting to mention that, in the first case (i.e., C-N bonding), the final stable $C_{54}H_{17}NO$ system corresponds to a singlet state, whereas in the latter situation (C-O bonding), the most stable $C_{54}H_{17}ON$ system is found to be in a triplet state. These conclusions can be rationalized by a simple MO analysis, which has been checked here using the semiempirical AM1 method applied to the NO + C_6H_5 system used as a proxy for the more general NO + C_nH_m systems. Let us consider the shape of the π MOs of NO radical (see Figure 4.4a and 4.4b). In its electronic ground state, the doubly occupied π MO displays a larger coefficient on the oxygen site than that on the nitrogen site because oxygen is more electronegative than nitrogen (Figure 4.4a). It is the reverse for the singly occupied π^* MO (Figure 4.4b). Then, when considering the reaction of NO with a σ aromatic radical, like the phenyl radical C_6H_5, the formation of C_6H_5-NO rather than C_6H_5-ON is expected. To get C_6H_5-ON, one electron must be promoted from the doubly occupied π (or σ , see below) MO to the singly occupied π^* MO in such a way that the remaining electron on the π (or σ, see below) MO can be paired with its phenyl partner. Now, the two electrons guided by the two-fold-degenerate π^* MO of NO have the propensity to be in the same spin state rather than be paired according to the well-known Hund rule. Such a situation favors a triplet rather than a singlet state. This analysis is in accordance with the fact that the angles C-N-O in C_6H_5-N-O and C-O-N in C_6H_5-O-N are around 120°. Then, it is actually the NO π orbitals that mainly govern the bonding.

To be more precise, we should mention that the AM1 energy ordering of the doubly occupied MOs in NO places the σ MO slightly above the π ones. Irrespective of this ordering, there are two possible promotions of one electron to the π^* MO, either from a σ or from a π MO. The two first excited states of NO are, respectively, $^4\Pi_i$ (38440 cm$^-$1) and $^2\Sigma^+$ (43965.7 cm$^-$1) (see ref [52]).

The configuration $\sigma\pi\pi$ does not correlate with a $^4\Pi$ state but with a $^2\Sigma\sigma^+$ one. On the contrary, the configuration $\pi\pi\pi$ correlates with a $^4\Pi$ state. The allowed electron-dipole $A^2\Sigma^+ \leftarrow X^2\Pi_r$ transition argues for the $\pi^* \leftarrow \sigma$

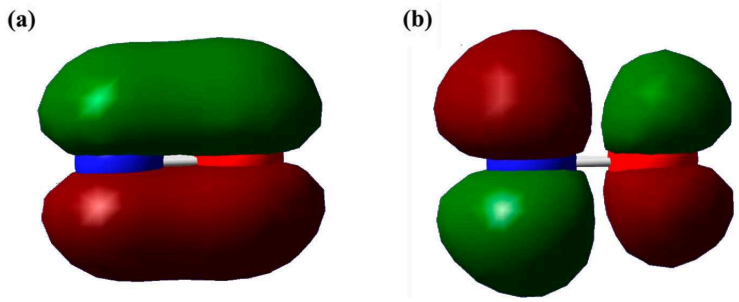


Figure 4.4: (a) Singly occupied MO π^* and (b) doubly occupied MO π^* of NO (the red ball is the oxygen atom). Both MOs have been obtained directly from a simple AM1 calculation

promotion. Anyway, there is a mixture between these two possible events because the angle C-O-N is neither 180 nor 90°.

In conclusion, we can note that the formation of C_6H_5-NO is expected to occur from the ground state of NO. In contrast, C_6H_5-ON requires that NO be promoted in a specific excited state, for instance, by an *ad hoc* radiation. We do not know if such processes have already been observed experimentally, but it would be a good test to reinforce the present analysis.

Table 4. Binding Energies (in kcal/mol) Calculated for the NO Interaction with the C_6H_5 Molecule[a]

	C_6H_5–NO (singlet)		C_6H_5–ON (triplet)	
	B3LYP	HF	RO-B3LYP	RO-HF
6-31G	−58.8	−34.7	−30.9	−35.8
6-31G(d,p)	−57.5	−34.0	−24.9	−30.5
cc-pVDZ	−56.1	−32.2	−22.8	−27.7

[a]The calculations have been performed with various basis sets for comparison, using RO-DFT and HF approaches when required.

When dealing with this simplified NO + C_6H_5 system, energy calculations performed at the DFT level show that the binding energy value in the C_6H_5 system is about twice (in absolute value) the value obtained for the C_6H_5-ON, system irrespective of the basis set used in the calculations (here, the calculations have been conducted with the 6-31G, 6-31G(d,p), cc–pVDZ basis sets; Table 4). This conclusion being very similar to that obtained for the larger $C_{54}H_{17}$ system. I have performed additional calculations to characterize the influence of the size of the carbonaceous system on the

results. As evidenced by the values given in Table 5, it turns out that the size of the surface does not strongly influence the binding energy value of NO, indicating thus that the reactivity with the defective cluster mainly depends on the local environment of the adsorbed NO species. Moreover, as already mentioned, the size of the basis set does not have any significant influence on the results.

Table 5. Binding Energies (in kcal/mol) Calculated for NO Adsorbed at the Defective Edge of Various C_nH_m Clusters of Increasing Size When Considering the Most Favorable Situation, That Is, Binding through a C−N Bond (Singlet State)[a]

	C_6H_5−NO		$C_{54}H_{17}$−NO		$C_{96}H_{23}$−NO	
	B3LYP	HF	B3LYP	HF	B3LYP	HF
6-31G	−58.8	−34.7	−59.3	−31.8	−61.5	−31.9
cc-pVDZ	−56.1	−32.2	−54.5	−29.6	−55.3	−29.7

[a]The calculations have been performed with the 6-31G and the cc-pVDZ basis sets for comparison, using RO shell methods (in both DFT and HF approaches) when required (i.e., for open-shell systems).

For comparison, Hartree-Fock calculations for the same systems as those considered in the DFT calculationswe were also performed, using a similar procedure (i.e., restricted, RO, or unrestricted calculations according to the situation) and the same basis sets. The corresponding results are given in Tables 3, 4, and 5, where it can be seen that HF and DFT approaches lead to strongly different values of the binding energies. For instance, the binding energy calculated for the formation of a C-N bond between NO and the $C_{54}H_{17}$ cluster is equal to −31.8 kcal/mol only with the HF approach, that is, a value that is about half of the one obtained in DFT calculations (Table 3). Worse, the formation of a C-O bond seems to be slightly favored in the HF approach, the corresponding binding energy value being around −34.9 kcal/mol. This conclusion is at odds with the MO orbital analysis presented above and clearly indicates a failure of the calculations at the HF level with the modest 6-31G basis set. Indeed, using larger basis sets seems to favor the C-N rather than the C-O binding, as evidenced in Table 4, in agreement with the conclusions drawn from the DFT results. Moreover, it should be noted that the results obtained with an unrestricted methodology

are characterized by a larger spin contamination than the corresponding unrestricted DFT calculations, in accordance with previously published studies for similar substrates[17].

Note that using a more accurate method, namely, the post-HF MP2 [45], leads to larger (absolute) values of the binding energy between NO and the defective cluster. For instance, the binding energy calculated in the singlet state for the $C_{54}H_{17}$-NO system is equal to -49.6 kJ/mol, that is, 50% larger than the value obtained at the HF level for the same system.

However, such sophisticated methods are very time-consuming for the large systems considered here, and DFT approaches thus appear as a good compromise between accuracy and tractability of the calculations.

Finally, calculations based on the (classical) reactive ReaxFF force field [53, 54] have been also carried out using the LAMMPS package [55] for comparison with the quantum results presented above. The optimization of the NO + C_nH_{m-1} systems confirms that the C-N is favored with respect to the C-O binding, the corresponding energies being equal to about -60 and -40 kJ/mol, respectively. It is interesting to note that not only the conclusions but also the binding energy values are in good agreement with the results obtained from DFT approaches. This indicates that the ReaxFF classical reactive potential might be accurate enough to investigate adsorption processes on carbonaceous systems. Of course, such a conclusion has to be confirmed by additional tests on other adsorbed species. Anyway, this conclusion may be very interesting especially for studying much larger systems (large soot nanoparticles, for instance) for which quantum approaches are totally prohibited due to their expected huge computational cost.

Unfortunately, the present results cannot be directly compared to the results available in the literature because the systems considered are not strictly equivalent. Indeed, both Kyotani et al.[16] and Montoya et al.[17] investigated the adsorption of NO on zigzag and armchair sites located at the edges of unsaturated carbonaceous clusters, that is, they do not consider any hydrogen atom in the vicinity of the possible adsorption sites. The resulting systems thus favored a parallel adsorption of NO, with a binding by both N and O atoms. However, it can be noted that among the various structures optimized by Kyotani et al.[16] and corresponding to local minima of the potential energy surface, a perpendicular C-NO configuration is much more favored than a C-ON one (see Figure4.3 and Table 4 of ref [16]), as obtained in the present paper. The binding energy calculated by Kyotani et al. for this C-NO structure is equal to -48 kJ/mol, a value slightly lower (in absolute value) than the one calculated here using however a different level of theory.

4.3.3 Discussion

Depletion of N_xO_y species by adsorption on carbonaceous surfaces is an important open question in atmospheric sciences [15]. This work was thus focused on the interaction between NO and carbonaceous clusters (C_nH_m), modeling the surfaces that are likely present in soot nanoparticles. I made use of quantum approaches to investigate the NO-C_nH_m system and found the following results: NO is physisorbed on the face of carbonaceous clusters even when they contain a Stone-Wales crystallographic defect. Although the present work is formally based on a more rigorous approach than previous studies [31],[33], especially because it takes into account the dispersion interactions in the DFT calculations, the conclusion remains similar; the interaction energy of NO on carbonaceous surfaces without any dangling bond is equal to a few kJ/mol (calculated at 0 K), and as a consequence, NO would not be efficiently trapped on such surfaces in atmospheric conditions.

This conclusion is in accordance with experimental results obtained at low temperature and low coverage[34]. It should be mentioned that I do not investigate here the influence of coverage on the adsorption process for two reasons; first, the experimental results showed that the adsorption energy is almost constant up to monolayer coverage and that adsorption is not accompanied by dimerization[34]; second, in the troposphere, it is unlikely that two NO species can be adsorbed in a close vicinity due to their quite low concentration.

It is interesting to note that Xu et al.[31] also studied the dissociative adsorption reaction of NO on graphite, which turns out to be a very complex process, characterized by very high energy barriers (more than 70 kcal/mol) along the corresponding reaction path. Although I do not find any evidence for such chemisorption in our optimization procedure (based on a different theoretical approach), it is worth noting that it does not change the relevance of the present conclusions in the atmospheric context. Indeed, the high barrier calculated by Xu et al.,[31] if confirmed by further experimental or theoretical works, cannot be overcome at tropospheric temperatures.

The situation is completely different when a dangling bond is created at the surface, for instance, by leaving an unsaturated C atom at the edge of the carbonaceous cluster. In this situation, our calculations evidenced a strong interaction between NO and the surface, leading to a chemisorption process without any barrier along the reaction path. This conclusion is in accordance with previous works based on different models for the unsaturated surface edges [16],[17] and also with theoretical studies devoted to adsorption of NO on graphite surfaces containing monovacancy defects, that is, a surface that also contains a dangling bond [20]. Such a situation is likely occurring in real

soot nanoparticles, and the corresponding defect sites formed, for instance, during the recombination of soot precursors [4], thus can be efficient trapping sites for NO in the troposphere.

4.4 Results for the adsorption of chlorinated species on carbonaceous surfaces

4.4.1 Adsorption of HCl on the face of a perfect carbonaceous cluster

The adsorption of HCl on a perfect carbonaceous surface modeled either by the coronene ($C_{24}H_{12}$) or the circumcorone ($C_{54}H_{18}$) molecules has been characterized by using the DFT method with the ωB97x-D (b) and BHandHLYP (a) functionals, as explained in the first part of this chapter.

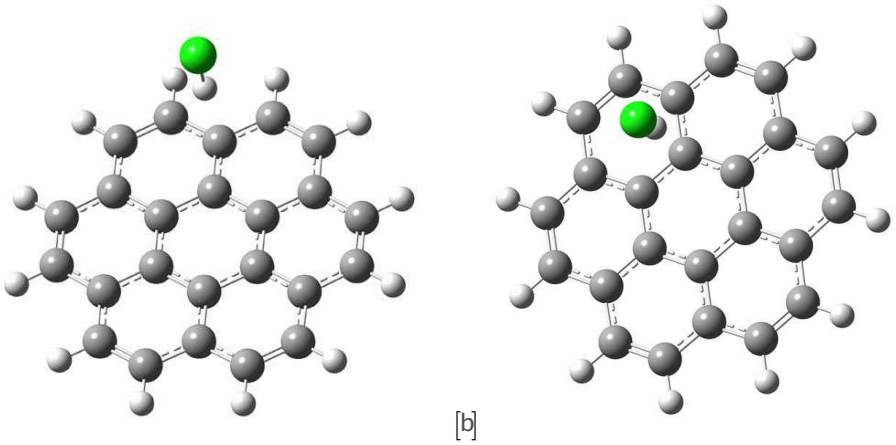


Figure 4.5: Optimized structures calculated for the adsorption of HCl on the face of a $C_{24}H_{12}$ cluster using the 6-311G^{++}(d,p) basis set and (a) the BHandHLYP and (b) the ωB97X–D functional

First, let us comment the results obtained on the coronene molecule. As it is shown in Fig 4.5, the BHandHLYP (a) and ωB97x-D (b) functionals lead to different results although in both cases the HCl molecule is found to adsorb vertically above a carbon site with the hydrogen atom pointing towards the carbonaceous surface. However, when using the BHandHLYP functional, HCl is located near the edge of the corenene molecule whereas it is adsorbed on a C of the central hexagon when using the ωB97x-D functional. Note that this adsorption geometry perpendicular to the surface, unlike the NO orientation on graphene, is due to the large electronegative

difference between the H and Cl atoms. Quantitatively, the BHandHLYP functional leads to an H-C distance of around 2.5 Å with an adsorption energy equal to −2.3 kcal/mol whereas the ωB97x-D gives 2.3 Å and −5.6 kcal/mol. The different results between the two functionals (different positions and energies) come from the dispersion term (explicitely respresented by an analytical form) in the ωB97x-D functional which tends to favor configurations corresponding to the maximum number of nearest neighbors. This results is confirmed when considering a larger cluster like $C_{54}H_{18}$. Indeed, in this case, the HCl position using the ωB97x-D functional is again found to be on top of a C atom of the central hexagon, whereas it is still on top of a cluster edge when using the BHandHLYP. Nonetheless, without any available experimental information, it is quite risky to discriminate between the different results obtained using different functionals. However, for such molecular systems where physisorption is expected, a functional taking into account the dispersion interaction should certainly be preferred.

For this adsorption process, the results of the Mulliken charge calculations (given in Fig 4.6 for $C_{24}H_{12}$ (a), HCl (b) and $C_{24}H_{12}HCl$ (c)) with the ωB97x-D functional, clearly show that the presence of HCl modifies locally but significantly the D_{6h} symmetry of the charge density on $C_{24}H_{12}$. Then, there is a small charge transfer from HCl to the cluster, especially near the carbon atom on which the molecule is adsorbed. Indeed, this carbon atom which is initially neutral (black color) in $C_{24}H_{12}$ becomes negatively charged (red color) in the adduct. Note that, although the carbon atoms saturated by hydrogen atoms at the edges of the cluster are negatively charged, the presence of these hydrogen atoms leads to a repulsion with the hydrogen of the HCl molecule, thus excluding these carbon atoms as possible adsorption sites.

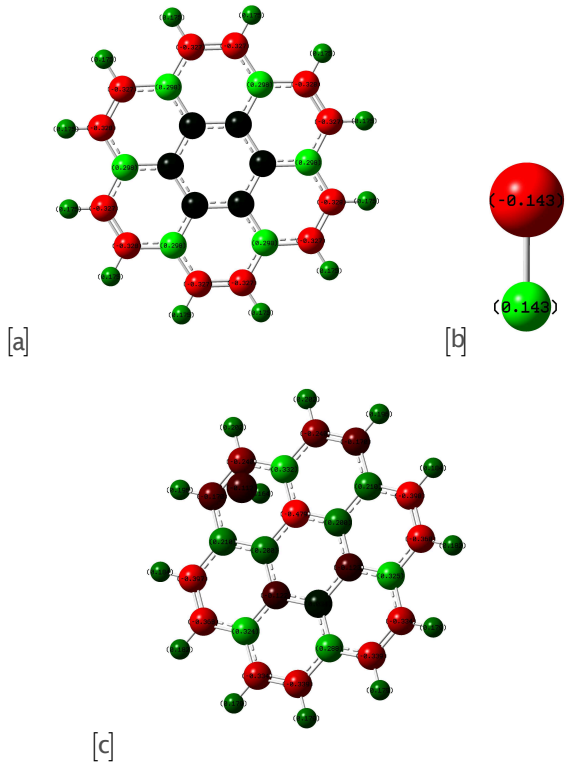


Figure 4.6: Mulliken analysis of the charge distributions for the a) $C_{24}H_{12}$ b) HCl and c) $C_{24}H_{12}HCl$ using the 6-311G^{++}(d,p) basis set and the ωB97X–D functional

4.4.2 Reaction of HCl on a defective carbonaceous cluster and of Cl on a perfect carbonaceous cluster

Furthemore, I have considered the adsorption process of the HCl molecule on a carbonaceous cluster containing a defect created by removing one H atom, thus leaving one dangling bond at the edge of the cluster. In this situation, chemisorption becomes a likely process and using a functional including explicit dispersion term is no more mandatory as shown when considering the case of NO on defective carbonaceous clusters (see above). In contrast, it remains still interesting to compare the results obtained with two different functionals. Thus, I characterized the adsorption process with the B3LYP and BHandHLYP functionals that have been previously used in the literature for discribing the bonding between chlorinated species and small PAHs[42].

Moreover, it is interesting to note that the expected reaction

$$C_nH_{m-1} + HCl \rightarrow C_nH_mCl \tag{4.2}$$

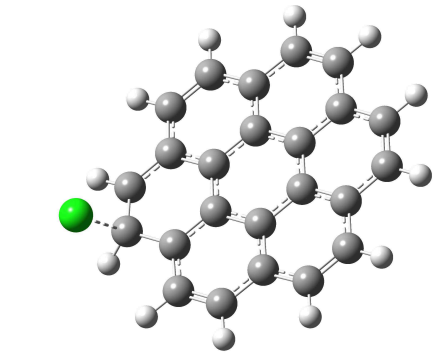
may *a priori* have the same final product as the following reaction

$$C_nH_m + Cl \rightarrow C_nH_mCl. \tag{4.3}$$

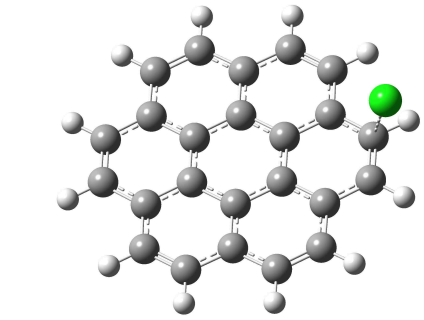
Thus, I also characterized the adsorption process of Cl on a perfect carbonaceous cluster. Note that both cases, HCl on C_nH_{m-1} and Cl on C_nH_m, corresponds to open-shell systems with the same number of electrons.

Then, the structures of the separated reactants ($C_{24}H_{12}$, Cl, $C_{24}H_{11}$, HCl) and of the products of their interactions were optimized by using the large 6-311G^{++}(d,p) basis set. Again, the coronene molecule is chosen as an example of small carbonaceous cluster for the following discussion.

The first interesting result is that when using the BHandHLYP functional, two stable structures (here named σ and π) were found for the final product of both reactions. In contrast, with the B3LYP functional, only one of these minima was reached, illustrating thus the importance of the choice of a functional when performing DFT calculations. These two structures, ilustred in Fig 4.7 a) σ and b) π have almost the same energy value (total energy of the system) being the π structure a little bit more stable (by less than 2 kcal/mol) than the σ, with a Cl-C distances of 2.51 Å and 1.93 Å respectively.



σ



π

Figure 4.7: Optimized structures calculated with the BHandHLYP functional and the 6-311G^{++}(d,p) basis set for the chemisorption of HCl on the edge of the defective $C_{24}H_{11}$ cluster or Cl on $C_{24}H_{12}$. The two stable structures obtained for the product $C_{24}H_{12}Cl$ are shown.

In fact, the energy difference of less than 2 kcal/mol between these two structures must be considered carefully because their respective stability comes from the competition process between the change of Cl-C bond length (2.61 to 1.93 Å) and the lost of aromaticity when passing from a π like structure to a σ one. Then, it is actually difficult to predict *a priori* which of these two tendencies is the most probable, and we can reasonably admit that both structures have more or less the same energy. This result is consistent with those published by Platz et all [42] who, in a study for benzene as aromatic reactant instead of coronene, shown in addition that only the BHandHLYP functional leads to a full set of optimized structures irrespective of the size of the basis set used. Moreover, Platz et al. discussed some experimental arguments based on UV-visible spectroscopy, ESR and kinetics, to justify that the π like structure is the global minima of the full potential energy surface for the system benzene+Cl.

With the global minimum already known, an interesting question concerns the energy character ΔE_{ads} of the two reactions 4.2 and 4.3 when using the BHandHLYP functional and the 6-311G^{++}(d,p) basis set. Then, taking as final product the π configuration, the corresponding binding energies were equal to -23.7 kcal/mol for the reaction $C_{24}H_{11}$ + HCl and -7.1 kcal/mol for the $C_{24}H_{12}$ + Cl.

These quite puzzling energy difference can be explained by using experimental (thermodynamics tables) and some selected theoretical data from the evaluation of heats of formation with the AM1 semiempirical method [56] (for more details, see the appendix A). But for short, considering that in both reaction there is formation of a Cl-C bound, it is easy to realize that this energetic difference of about 15 kcal/mol comes from the energy gained when, on the one hand breaking a Cl-H bound (103 kcal/mol) and, on the other hand, creating a C-H bond (C_nH_{m-1}–H) in the carbonaceous cluster (113 kcal/mol). Nevertheless, this comparison is not immediate because our DFT calculations provides energy differences at 0K without any zero point energy (ZPE) correction whereas AM1 and experimental values correspond to enthalpie values at 298K.

Another important result is that I also performed similar DFT calculations with the quite small 6-31G basis set, to evaluate the accuracy of much shorter (in terms of computing time) calculations. The main conclusion is that such a difference of about 10-15 kcl/mol can only be obtained when using a large basis set like the 6-311G^{++}(d,p) including polarization effects irrespective of the functional used. Indeed, the smaller basis set leads to much larger differences, mainly as a result of a very poor energetic description of the H-Cl bond.

4.4.3 Reaction of HCl on carbonaceous cluster with a single vacancy site

Another interesting configuration from a theoretical point view is the precense of defects on the carbon surfaces. Thus, in this section, a monovacancy is modeled by removing one central carbon atom in a cluster made of 30 fused benzene rings arranged in a single atomic layer. The defective particle thus contain 79 carbon atoms with the edges of this carbonaceous cluster being saturated by hydrogen atoms ($C_{79}H_{22}$ cluster).

It should be noted that removing a C atom from a perfect carbonaceous surface is the simplest way to simulate a defective surface, despite it is an unlikely process in realistic atmospheric conditions because of the high activation energy required by the corresponding process [43]. However, carbon atom vacancies have been evidenced in atomistic simulations of soot

formation, coming from incomplete recombination of small soot precursors (typically CnHm with small n and m values) [4]. In that sense, the defective cluster optimized here can be considered as a realistic model of defective surfaces that might exist in soot.

Then, based on the results of the previous section, DFT calculations with the BHandHLYP functional and the 6-311G^{++}(d,p) were performed to optimize the structure of the corresponding defective particle ($C_{79}H_{22}$) and to investigate the interaction of HCl with the resulting defective carbonaceous cluster.

Lets first comment the most stable structure found for the reactants. The atomic vacancy created is surrounded by three carbon atoms, each having a dangling sp^2 bond corresponding to 3 unpaired σ electrons and one unpaired π electron. For the $C_{79}H_{22}$ cluster, two of the three carbon atoms carrying an unpaired electron tend to reform a single bond, and a five-membered ring is consequently stabilized in the defective cluster. Moreover, a σ dangling bond is localized on the third atom around the vacancy site, and the presence of this dangling bond together with that of the five-membered ring finally leads to a loss of planarity for the optimized structure of the $C_{79}H_{22}$ defective cluster with a small increase of the first nearest-neighbor distances around the vacancy site (1.68 Å instead of 1.42 Å in perfect graphite).

Then, the optimization procedure starting from the HCl molecule located right above the carbon vacancy leads to the dissociative chemisorption of the HCl molecule, and ends with the chemisorption of the H atom on one C atom around the vacancy with a C-H distance equal to 1.05 Å, and the chemisorption of the Cl atom on top of a C atom of the unsaturated hexagonal ring, with a C-Cl bond length equal to 1.9 Å. In this configuration, the Cl-H distance is finally equal to 2.27 Å, and the binding energy calculated as the energy difference between the product of the reaction and the two reactants separated from each other, is equal to -36.5 kcal/mol. This indicates that chemisorption of HCl on such defective surface is an exothermic process that should be possible in fire situations (see the Introduction part of this chapter), although I did not characterize the energy barriers along the corresponding reaction path.

It is interesting to mention that this adsorption process is however less exothermic than the chemisorption of H_2O on the same surface (binding energy equal to) which leads to the dissociation of the water molecule and a resulting binding energy of more that 300 kJ/mol [11]. Indeed, the next interesting step for our study would be the characterization of the adsorption process on the chlorinated carbonaceous surface, in order to help at interpreting experimental observations showing that, for soot produced by fuels containing chlorine (PVC, electrical cables, electrical equipment), the

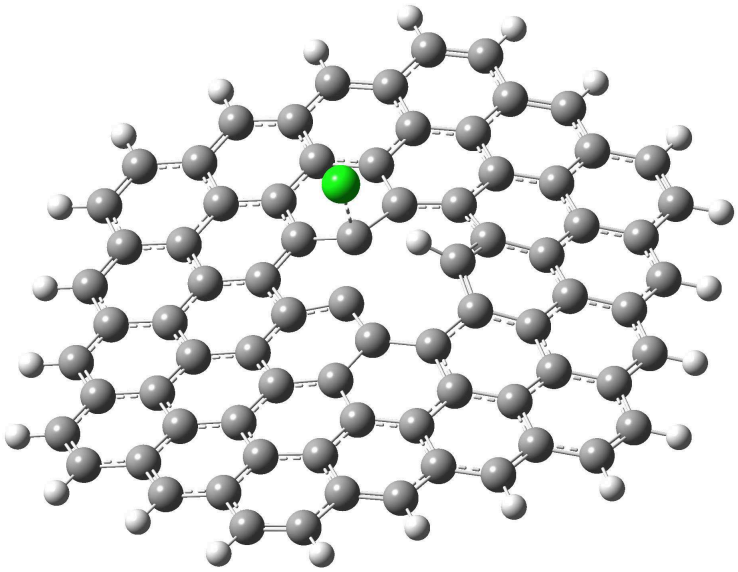


Figure 4.8: Optimized structure calculated with the BHandHLYP functional and the 6-311G^{++}(d,p) basis set for the chemisorption of HCl on a monovacancy created on a carbonaceous cluster (here, the product of the reaction HCl + $C_{79}H_{22}$ is shown)

.

amount of water sorbed on the surface of soot (determined using sorption balance) is much larger than on soot without Cl [30].

4.5 Conclusions

The goal of this study was first to investigate the adsorption of NO, Cl and HCl molecules on perfect carbonaceous clusters, mainly by using DFT approaches. Here, it has been shown that the interaction of these molecules with a perfect carbonaceous surface corresponds to a physisorption process that requires using a functional taking into account the dispersion effects. In this way, ωB97X-D seems to represent an accurate functional for studying physisorption on weakly interacting systems such as those considered here.

In a second step, I have used various theoretical approaches to characterize the interaction between NO, Cl and HCl species and the defective edges or faces of carbonaceous clusters because such a situation could also model the surfaces that can be found in soot nano-particles[4].

In contrast with the adsorption on the face, interaction of NO with the edge of a defective cluster leads to chemical bonding, with a net preference for a C-N rather than a C-O binding that can be explained on the basis of simple theoretical chemistry considerations. Similarly, the adsorption of HCl on a carbon monovacancy leads to a chemisorption process resulting in the dissociation of the HCl molecule. Both studies show the specific role that may play the defects in carbonaceous structures regarding the adsorption of atmospheric species.

The first conclusion of this work is thus that soot may be an efficient sink for NO and chlorinated species in the troposphere only if it contains a sufficiently high number of defective sites, mainly unsaturated carbon atoms. Moreover, besides its atmospheric interest, this study is clearly evidence that quantum calculations (both at the DFT and HF levels of theory) have to be carefully conducted when considering the interaction between atmospheric species and carbonaceous surfaces, although these systems might appear quite simple at first glance. Problems encountered with system size, functional type, size of the basis set, spin contamination, and spin multiplicity should be thus systematically carefully addressed before any credible conclusion can be drawn.

Bibliography

[1] Chung, S.H., Seinfeld J.H. Global Distribution and Climate Forcing of Carbonaceous Aerosols. J Geophys Res 2002;107:4407.

[2] Chen, Y.; Penner, J.E. Uncertainty Analysis for Estimates of the First Indirect Aerosol Effect. Atmos. Chem. Phys. 2005;5:2935-2948.

[3] Demirdjian, B.; Ferry, D.; Suzanne, J.; Popovicheva, O.B.;Persiantseva, N.M.; Shonija, N.K. Heterogeneities in the Micro-structure and Composition of Aircraft Engine Combustor Soot:Impact on the Water Uptake. J. Atmos. Chem. 2007;56:83-103.

[4] Violi, A. Modeling of Soot Particle Inception in Aromatic and Aliphatic Premixed Flames. Combust. Flame 2004;139:279-287.

[5] Picaud, S.; Hoang, P.N.M.; Hamad, S.; Mejias, J.A.; Lago, S. A Theoretical Study of the Adsorption of Water on a Model Soot Surface. II. Molecular Dynamics Simulations. J. Phys. Chem. B 2004;108:5410-5415.

[6] Moulin, F.; Picaud, S.; Hoang, P.N.M.; Jedlovszky, P. Grand Canonical Monte Carlo Simulation of the Adsorption Isotherms of Water Molecules on Model Soot Particles. J. Chem. Phys. 2007; 127:164719.

[7] Hantal, G.; Picaud, S.; Hoang, P.N.M.; Voloshin, V.P.; Medvedev, N.N.; Jedlovszky, P. Water Adsorption Isotherms on Porous Onion-Like Carbonaceous Particles. Simulations with the Grand Canonical Monte Carlo Method. J. Chem. Phys. 2010; 133:144702/1-144702/12.

[8] Hamad, S.; Mejias, J.A.; Lago, S.; Picaud, S.; Hoang, P.N.M. A Theoretical Study of the Adsorption of Water on a Model Soot Surface. I. Quantum Chemical Calculations. J. Phys. Chem. B 2004; 108: 5405-5409.

[9] Collignon, B.; Picaud, S.; Hoang, P.N.M.; Liotard, D.; Rayez, M.T.; Rayez, J.C. A Semi-Empirical Potential Model for Calculating the

Interactions between Large Aromatic Molecules and Soot Surfaces. J. Mol. Struct.; THEOCHEM 2006; 772: 1-12.

[10] Oubal, M.; Picaud, S.; Rayez, M.T.; Rayez, J.C. A Theoretical Characterization of the Interaction of Water with Oxidized Carbonaceous Clusters.Carbon 2010; 48: 1570-1579.

[11] Oubal, M.; Picaud, S.; Rayez, M.T.; Rayez, J.C. Interaction of Water Molecules with Defective Carbonaceous Clusters: An Ab Initio Study. Surf. Sci. 2010; 604: 1666-1673.

[12] Oubal, M.; Picaud, S.; Rayez, M.T.; Rayez, J.C. Water Adsorption on Oxidized Single Atomic Vacancies Present at the Surface of Small Carbonaceous Nanoparticles Modeling Soot. Chem. Phys. Chem. 2010; 11: 4088-4096.

[13] Oubal, M.; Picaud, S.; Rayez, M.T.; Rayez, J.C. Adsorption of Atmospheric Oxidants at Divacancy Sites of Graphene: A DFT Study. Comput. Theor. Chem. 2013; 1016: 22-27.

[14] Finlayson-Pitts, B.J.; Pitts, Jr., J. Chemistry of the Upper and Lower Atmosphere. Theory, Experiments, and Applications; Academic Press: San Diego, CA; 2000: p 17.

[15] Seinfeld, J.H.; Pandis, S.N. Atmospheric Chemistry and Physics. From Air Pollution to Climate Change; Wiley: New York, 1998: p 259.

[16] Kyotani, T.; Tomita, A. Analysis of the Reaction of Carbon with NO/N_2O Using Ab Initio Molecular Orbital Theory. J. Phys. Chem. B 1999; 103: 3434-3441.

[17] Montoya, A.; Truong, T. N.; Sarofim, A. F. Spin Contamination in Hartree-Fock and Density Functional Theory Wavefunctions in Modeling of Adsorption on Graphite. J. Phys. Chem. A 2000; 104:6108-6110.

[18] Zhu, Z.H.; Finnerty, J.; Lu, G.Q.; Yang, R.T. Opposite Roles of O_2 in NO- and N_2O-Carbon Reactions: An Ab Initio Study. J. Phys. Chem. B 2001; 105: 821-830.

[19] Ghigo, G.; Maranzana, A.; Tonachini, C.; Zicovich-Wilson, C.M.; Causa, M. Modeling Soot and Its Functionalization under Atmospheric Combustion Conditions by Density Functional Theory within Molecular (Polycyclic-Aromatic-Hydrocarbon-like) and Periodic Methodologies. J. Phys. Chem. B 2004; 108: 3215-3223.

[20] Xu, S.C.; Irle, S.; Lin, M.C. Quantum Chemical Prediction of Reaction Pathways and Rate Constants for Reactions of NO and NO_2 with Monovacancy Defects on Graphite (0001) Surfaces. J. Phys. Chem. C 2010; 114: 8375-8382.

[21] Smith, D.M.; Welch, W.F.; Graham, S.M.; Chughtai, A.R.; Wicke, B.G.; Grady, K.A. Reaction of Nitrogen Oxides with Black Carbon: An FT-IR Study. Appl. Spectrosc. 1988; 42: 674-680.

[22] D.W. Boukhvalov and M.I. Katsnelson. Chemical functionalization of graphene. J. Phys.: Condens. Matter 2009; 21:344205.

[23] Y. G. Zhou, X. T. Zu, F. Gao, H. F. Lv, and H. Y. Xiao. Adsorption-induced magnetic properties and metallic behavior of graphene.App. Phys. Lett. 2009; 95:123119.

[24] P.V.C. Medeiros, A.J.S. Mascarenhas, F. de Brito Mota and C.M.C de Castilho. A DFT study of halogen atoms adsorbedon graphene layers. Nanotechnology 2010; 21:485701.

[25] M. Ijas, P. Havu, and A. Harju. Fracturing graphene by chlorination: A theoretical viewpoint.Phys. Rev. 2012; 85:035440.

[26] M. Yang, L. Zhou, J. Wang, Z. Liu, and Z. Liu. Evolutionary Chlorination of Graphene: From Charge-Transfer Complex to Covalent Bonding and Nonbonding. J. Phys. Chem. C 2012; 116:844–850.

[27] D.B. Karki and N.P. Adhikari. First-principles study of the stability of graphene and adsorption of halogen atoms (F, Cl and Br) on hydrogen passivated graphene.Int. J. Modern Phys. B 2014; 28:1450141.

[28] J.P. Stone, R.N. Hazlett, J. Enoch Johnson, and H.W. Carhart. The transport of hydrogen chloride by soot from burning polyvinyl chloride. J. Fire and Flammability 1973; 4:42-51.

[29] E.A. Ramskill. Toxicity aspects and application of the naval protective gas mask to shipboard fires. Section VIII of Naval Research Laboratory Memorandum Report 1816 (1967).

[30] F.-X. Ouf. Private communication (2015).

[31] Xu, S.C.; Irle, S.; Musaev, D.G.; Lin, M.C. Quantum Chemical Prediction of Reaction Pathways and Rate Constants for Dissociative Adsorption of CO_x and NO_x on Graphite (0001) Surface. J. Phys. Chem. B 2006; 110: 21135-21144.

[32] Leenaerts, O.; Partoens, B.; Peeters, F.M. Adsorption of H_2O,NH_3, CO, NO_2, and NO on Graphene: A First-Principles Study. Phys. Rev. B 2008; 77: 125416.

[33] Zhang, Y.H.; Chen, Y.B.; Zhou, K.G.; Liu, C.H.; Zeng, J.; Zhang, H.L.; Peng, Y. Improving Gas Sensing Properties of Graphene by Introducing Dopants and Defects: A First-Principles Study. Nanotechnology 2009; 20: 1885504.

[34] Brown, C.E.; Hall, P.G. Physical Adsorption of Nitric Oxide on Graphite and Silica and Adsorption of Gases on Nitric Oxide Preadsorbed on Carbon. J. Colloid Interface Sci. 1973; 42: 334-341.

[35] Chai, J.D.; Head-Gordon, M. Long-Range Corrected Hybrid Density Functionals with Damped Atom-Atom Dispersion Corrections. Phys. Chem. Chem. Phys. 2008; 10: 6615-6620.

[36] Klimes, J.; Michaelides, A. Perspective: Advances and Challenges in Treating van der Waals Dispersion Forces in Density Functional Theory. J. Chem. Phys. 2012; 137: 120901.

[37] Vosko, S.H.; Wilk, L.; Nusair, M. Accurate Spin-Dependent Electron Liquid Correlation Energies for Local Spin Density Calculations: A Critical Analysis. Can. J. Phys. 1980; 58: 1200-1211.

[38] Becke, A.D. Density-Functional Thermochemistry III. The Role of Exact Exchange. J. Chem. Phys. 1993; 98: 5648-52.

[39] Tournus, F.; Charlier, J.C. Ab Initio Study of Benzene Adsorption on Carbon Nanotubes. Phys. Rev. B 2005; 71: 165421.

[40] Jacob, C.R.; Reiher, M. Spin in Density-Functional Theory. Int. J. Quantum Chem. 2012; 112: 3661-3684.

[41] Becke, A.D. A new mixing of Hartree-Fock and local density-functional theories. J. Chem. Phys. 1993; 98:1372-1377.

[42] Tsao, M.-L., Hadad, C.M., and Platz, M.S. Computational Study of the Halogen Atom-Benzene Complexes. J. Am. Chem. Soc. 2003; 125:8390-8399.

[43] A.A. El-Barbary, R.H. Telling, C.P. Ewels, M.I. Heggie, P.R. Briddon, Phys. Rev. B (2003) 68 144107.

[44] Lauderdale, W.J.; Stanton, J.F.; Gauss, J.; Watts, J.D.; Bartlett, R.J. Many-Body Perturbation Theory with a Restricted Open-Shell Hartree-Fock Reference. Chem. Phys. Lett. 1991; 187: 21-28.

[45] Head-Gordon, M.; Pople, J.A.; Frisch, M.J. MP2 Energy Evaluation by Direct Methods. Chem. Phys. Lett. 1988; 153: 503.

[46] Frisch, M.J.; Trucks, G.W.; Schlegel, H.B.; Scuseria, G.E.; Robb, M.A.; Cheeseman, J.R.; Scalmani, G.; Barone, V.; Mennucci, B.; Petersson, G.A.; et al. Gaussian 09, Revision D.01; Gaussian, Inc.: Wallingford; CT; 2009.

[47] Kohanoff, J. Electronic Structure Calculations for Solids and Molecules; Cambridge University Press: Cambridge, U.K.; 2006: p 82.

[48] Perdew, J.P.; Burke, K.; Ernzerhof, M. Generalized Gradient Approximation Made Simple. Phys. Rev. Lett. 1996; 77: 3865-3868.

[49] Banhart, F.; Kotakoski, J.; Krasheninnikov, A.V. Structural Defects in Graphene. ACS Nano 2011; 5: 26.

[50] Zhang, Y.H.; Zhou, K.G.; Xie, K.F.; Gou, X.C.; Zeng, J.; Zhang, H.L.; Peng, Y. Effects of Stone-Wales Defect on the Interactions Between NH_3, NO_2 and Graphene. J. Nanosci. Nanotechnol. 2010; 10: 1.

[51] Qin, X.; Meng, Q.; Zhao, W. Effects of Stone-Wales Defect upon Adsorption of Formaldehyde on Graphene Sheet with or without Al Dopant: A First-Principle Study. Surf. Sci. 2011; 605: 930.

[52] Huber, K.P.; Herzberg, G. Molecular Spectra and Molecular Structure IV. Constants of Diatomic Molecules; van Nostrand Reinhold Company: New York; 1979.

[53] van Duin, A.C.T.; Dasgupta, S.; Lorant, F.; Goddard, W.A., III. ReaxFF: A Reactive Force Field for Hydrocarbons. J. Phys. Chem. A 2001; 105: 9396-9409.

[54] Chenoweth, K.; van Duin, A.C.T.; Goddard, W.A., III. ReaxxFF Reactive Force Field for Molecular Dynamics Simulations of Hydrocarbon Oxidation. J. Phys. Chem. A 2008; 112: 1040-1053.

[55] Plimpton, S. Fast Parallel Algorithms for Short-Range Molecular Dynamics. J. Comput. Phys. 1995; 117: 1-19.

[56] Dewar, M.J.S.; Zoebisch, E.G.; Healy, E.F.; Stewart, J.J.P. AM1: A New General Purpose Quantum Mechanical Molecular Model. J. Am. Chem. Soc. 1985; 107: 3902-3909.

Chapter 5

Optical Properties of soot

Scattering of electromagnetic waves by any system is related to the heterogeneity of that system: heterogeneity on the molecular scale or on the scale of aggregations of many molecules. Although in practice we have several kinds of heterogeneity, the nature of the physical phenomenon is always the same for all systems. Matter is composed of discrete electric charges that, in presence of an electromagnetic wave, are set into oscillatory motion by the electric field of the incident wave. Accelerated electric charges radiate electromagnetic energy in all directions; it is this secondary radiation that is called the radiation scattered by the obstacle. Thus,

$$Scattering = excitation + reradiation. \tag{5.1}$$

In addition, to reradiating electromagnetic energy, the excited elementary charges may transform part of the incident electromagnetic energy into other forms as for instance, thermal energy. This process is called absorption.

$$Absorption = excitation + transfer. \tag{5.2}$$

When an arbitrary particle is illuminated by a beam of light that can be modeled by a plane wave with specified characteristics (wavelength, polarization state), the amount and angular distribution of the light scattered by the particle, as well as the amount absorbed, depend in a detailed way on the nature of the particle, that is, its shape, size, porosity and chemical composition.

This fact leads us to the direct and inverse problems in the theory of the interaction of an electromagnetic wave with a small particle. Using a dragon

analogy, as Bohren and Huffman in their celebrated book[1], these problems are:

The *direct problem*: Knowing the dragon, describe his tracks or, given a particle of specified shape, size and chemical composition, which is illuminated by a beam of specified irradiance, polarization, and frequency, determine the field everywhere.

The *inverse problem*: Knowing the tracks, describe the dragon or, by a suitable analysis of the scattered field, describe the particle(s) that is/are responsible for the scattering.

This chapter aims at clarifying some subtle aspects of the interaction of light with soot nanoparticles. Note that as mentioned in chapter (2), soot is mainly made of strongly absorbing carbon so that scattering can usually be neglected with respect to absorption. Hence, we will concentrate on the absorption properties of soot.

One of the main goals during this PhD thesis is to provide information that allows to connect the two problems mentioned before, by using simulation methods to compute the absorption spectrum of model soot nanoparticles, starting from well defined morphological details, in order to build a database of results that will help interpreting experimental results.

The advantage of the method described in this chapter is that using an atomistic framework combined with particle construction allows to isolate certain variables to study the influence of particle features such as atomic positions (hence porosity or rugosity) or chemical composition, onto the spectroscopic signals of the particle.

5.1 Atmospheric interest

As already mentioned in the Introduction part of this manuscript, carbonaceous particles emitted by combustion processes are suspected to have a non-negligible impact on the Earth's radiative balance[2]. First, they have direct effects because they scatter and absorb solar and thermal infrared radiation, thus modifying the Earth's albedo. Second, they have an indirect effect because these particles may act as ice and cloud condensation nuclei thus impacting the local and global radiative properties of clouds[3, 4]. These particles, together with the other atmospheric aerosols, are currently one of the largest sources of uncertainties in understanding climate evolution and in quantifying the amplitude of temperature changes[5]. This mainly comes from the high natural variability of the sources of carbonaceous particles due to different conditions of combustion and fuel compositions[6].

Generally, carbonaceous particles consist of a complex mixture of chemical compounds and are usually divided (somewhat artificially) into two fractions. The black (or elemental) carbon (BC) fraction is strongly absorbing visible and near-IR light. BC concentrations are therefore usually determined by light-absorption measurements. In contrast, the organic fraction (OC) of the aerosol represents an aggregate of hundreds of individual compounds exhibiting a wide range of chemical and thermodynamic properties. Because of this complexity, aerosol OC content is usually determined from the difference between total carbon and BC contents[6], where the total carbon is usualy determined by conversion to CO_2 which is then easily measured.

As already noted, widely accepted structural models for BC combustion particles are based on fractal particles coming from agglomeration of primary carbonaceous nanoparticles. These models assume that the primary nanoparticles are made of small pieces of graphene sheets, whose stacking on concentric spheres of different radii results in typical onion-like structures[7]. These primary nanoparticles may also contain a very small fraction of other atoms (mainly oxygen) besides carbon, due to partial oxidation[8]. They also contain defects like edges or atom vacancies formed during the recombination of soot precursors[9], leading thus to different ratios of aromatic to aliphatic carbon atoms. In addition, they can be also coated by various organic and aromatic species due to aging in the atmosphere.

Owing to this complexity, a detailed understanding of both direct and indirect climatic effects of carbonaceous particles remains challenging and requires the characterization of the interaction of these particles with electromagnetic radiations, as a function of the geometrical and chemical characteristics of the nanoparticles constituting the carbonaceous fraction of the aerosols.

In this respect, theoretical approaches at the atomic scale can give details on the involved processes that are not directly accessible to experimental probes. They can also help at interpreting experimental information and data coming from observations.

In a recent series of papers[10, 11, 12, 13], researchers from UTINAM have been interested in characterizing the indirect effect of soot on climate. They thus modeled soot surfaces and their interaction with water to characterize the influence of the structural and chemical details on the ability of soot nanoparticles to act as ice and cloud condensation nuclei. Here, I rather focus on the direct effect, i.e., on the relation between the soot nanostructure and its interaction with solar radiation, on the basis of a preliminary work[14, 15].

Indeed, although the study of light absorption by carbonaceous particles is not a new field (see for instance the reviews by Sorensen[16] and Bond et al.[17]), a direct relation between the atomistic characteristics of these particles and their effect on climate is still missing. For instance, simplified macroscopic models are still widely used based on the Mie theory (exact solution of Maxwell equations)[18, 1], that assumes single (or aggregates of) homogeneous spherical particles. More sophisticated approaches are also able to take into account heterogeneity[19, 20] or irregularly shaped particles[21]. Alternatively, powerful numerical methods such as the discrete dipole approximation (DDA)[22, 23, 24] or the T-matrix method[25] are now largely disseminated for computing scattering of radiation by small particles of arbitrary shape and by periodic structures. However, none of these methods allows a direct connection between the atomic composition of carbonaceous particles and their absorption/extinction properties.

In the following, a method to calculate the absorption properties of carbonaceous primary nanoparticles is thus presented, directly based on the knowledge of the positions and polarizability of the atoms constituting the particle. This method is more specifically used to calculate the mass specific absorption cross section coefficient (MAC) of primary soot nanoparticles modeled at the atomic scale and it is described in Section 2. Then, the accuracy of the parameters used to represent the carbon atom polarizability is checked by comparison with experimental results obtained for the C_{60} molecule in Section 3. In the same section, the results for fullerene molecules of increasing radius are also given to investigate the influence of the particle size on the MAC calculations. In Section 4, the approach used to model soot particles at the atomic scale is detailed and the corresponding MAC curves are calculated in the UV spectral range. Finally, conclusions are given and further developments of this work are discussed in Section 5. Note that the method and most of the results presented in this chapter have been published in the paper "Calculations of the mass absorption cross sections for carbonaceous nanoparticles modeling soot" (C. García-Fernández, S.Picaud, M.Devel. Journal of Quantitative Spectroscopy and Radiative Transfer 2015; 164:69–81).

5.2 Model

5.2.1 Principle of the PDI model

In this study, I chose to calculate two experimentaly relevant properties, i.e., the absorption cross section C_{abs} and the mass specific absorption cross

section coefficient (MAC) defined as the ratio of C_{abs} to the total mass of the nanostructure.

Following the work of Draine[23], C_{abs} for a nanograin made of N atoms can be related to the imaginary part of the dynamic polarizability tensor $\overleftrightarrow{\alpha_i}(\omega)$ of each atom i as[23] :

$$C_{abs}(\omega) = \frac{4\pi k}{|E_0(\omega)|^2} \sum_{i=1}^{N} \left\{ Im[\vec{\mu}_i(\omega).(\overleftrightarrow{\alpha_i})^{-1}(\omega))^* \vec{\mu}_i(\omega)^*] - \frac{2}{3} k^3 \vec{\mu}_i(\omega).\vec{\mu}_i(\omega)^* \right\}, \tag{5.3}$$

where $\vec{E_0}(\omega)$ is the external homogeneous electric field applied to the system, $\vec{\mu}_i$ is the dipole moment induced on the ith atom by that applied field and $k = 2\pi/\lambda$ is the wavenumber associated to the incident light of wavelength λ.

To compute the $\vec{\mu}_i$, I use the Point Dipole Interaction (PDI) model[26] according to which this dipole can be directly computed from the knowledge of the atomic polarizabilities and of the local electric field $\vec{E}_{loc}(\vec{r}_i, \omega)$ at position $\vec{r}_i$.

Note that the PDI model is in fact similar to the discrete dipole approximation (DDA) method[22, 23, 24]. However, DDA is used at a scale at which the continuum approximation is valid. Thus, in DDA, effective polarizabilities derived from a combination of the material local dielectric susceptibility and the volume of the discretization element through a Clausius-Mossotti-like relation (with radiative corrections) are used. In contrast, as it will be explained below, PDI requires the knowledge of the exact positions $\vec{r}_i$ of the atoms constituting the nanostructure under investigation and of their polarizabilities. Note that these atomic polarizabilities can either be derived from *ab initio* Time Dependent Density Functional Theory (TD-DFT) calculations or from Clausius-Mossotti-like relations but with depolarization factors adapted to the symmetries of the true atomic lattice and not to the orthorhombic lattice used in the discretization procedure of DDA.

In the PDI model, the local electric field is thus written, as in DDA, as the sum of the external field $\vec{E_0}(\omega)$ and of the electric field created at the position $\vec{r}_i$ by the dipoles induced on the other atoms of the carbonaceous nanostructure. Hence, the individual dipoles can be computed by solving the following linear system of equations:

$$\forall i = 1, ..., N \quad \vec{\mu}_i, (\omega) = \overleftrightarrow{\alpha}_i\ (\omega)\vec{E}_0(\omega) + \sum_{j \neq i=1}^{N} \overleftrightarrow{\alpha}_i\ (\omega)\ \overleftrightarrow{T}^{(2)}\ (\vec{r}_i, \vec{r}_j, \omega)\vec{\mu}_j(\omega)\ , \tag{5.4}$$

where $\overleftrightarrow{T}^{(2)}$ is the electric field propagator in vacuum that is written as[15]

$$\overleftrightarrow{T}^{(2)}\ (\vec{r}_i, \vec{r}_{j\neq i}, \omega) = -\frac{1}{\epsilon_0}\left(\vec{\nabla}_{\vec{r}_i} \otimes \vec{\nabla}_{\vec{r}_i} + \frac{\omega^2}{c^2}\ \overleftrightarrow{\mathbb{I}}\right)\left(-\frac{e^{i\frac{\omega}{c}|\vec{r}_i - \vec{r}_j|}}{4\pi\,|\vec{r}_i - \vec{r}_j|}\right), \tag{5.5}$$

where $\overleftrightarrow{\mathbb{I}}$ is the identity tensor.

The calculation of the absorption cross section for the carbonaceous nanostructures considered here thus requires the knowledge of the exact positions $\vec{r}_i$ of the atoms constituting this nanostructure. In this respect, the PDI method thus differs from the usual implementations of the Discrete Dipole Approximation (DDA) method [22, 23] that are rather based on the scattering of dipoles on a regular cartesian grid to allow use of fast Fourier transform (FFT) algorithms. Note that despite this arbitrary discretization of the volume of the nanostructure under consideration, DDA approaches are much often used in the literature especially because of the wide dissemination of corresponding open source codes[24, 27, 28, 29], in contrast to the PDI method for which no general code is available. As the exact atomic positions are often not known in many carbonaceous structures, especially the soot systems investigated here, the PDI method thus could appear irrelevant at first sight. However, these positions can be defined in model systems such as those used in the present work and the exact relation between the optical properties of a carbonaceous nanostructure and its atomic details can be directly computed, without any assumption on the global geometry of the system under study. In a similar way, combining this PDI approach with experimental measurements could allow optical methods to be an unique probe for examining the intimate structure of such carbonaceous systems, if distinctive features broader than the resolution of the instrument can be found.

5.2.2 parametrization of carbon polarizabilities in the PDI model

Eq. 5.4 also requires the knowledge of the atomic polarizability tensors $\overleftrightarrow{\alpha}_i\ (\omega)$ associated with the atoms present in the nanostructure under study.

Considering that the carbonaceous nanostructures investigated here can *a priori* be made of different hybridized carbon atoms (depending on the local environment of the carbon atoms in the system) different atomic polarizability tensors for the corresponding C atoms must be defined.

Initially, it was envisaged that the polarizability tensors for any kind of atoms present in organic molecules or soot could be obtained by a fitting procedure. This would have consisted in using as input data the polarizability tensors of a group of small molecules computed by DFT and as model data the polarizability tensors of the same molecules computed using PDI with the polarizability tensor elements for each atom with a different chemical nature and hybridization state as parameters (see e.g. [30]). This procedure was to be applied for each frequency. Then, we realized that the DFT code we had at hand could not give us reliable results for complex polarizabilities near absorption peaks and that we should use TD-DFT codes such as those used by Malloci et al. to fill their database of spectroscopic properties of polycyclic aromatic hydrocarbons[31]. In the meantime, we had decided to use a less sophisticated approach described hereafter.

In this work, we have made the approximation that carbon atoms that are surrounded by three nearest neighbors can be treated as sp^2 hybridized carbons and given an anisotropic polarizability tensor derived from the polarizability tensor of C atoms in graphite, as computed from frequency dependent permittivities given by Draine[32], even if the carbon network is locally curved. More precisely, to compute the polarizability tensor of such a carbon atom surrounded by three nearest neighbors, we use the the coordinates of the 3 neighbors to define a local frame with two unit vectors parallel to the plane tangent to the one defined by the three nearest neighbors and one unit vector perpendicular to this plane[33]. Indeed, in this local frame, the atomic polarizability tensors are diagonal (and anisotropic) with two parallel ($\alpha_{i,||}^{local}$) and one perpendicular components ($\alpha_{i,\perp}^{local}$). For coherence with previous works done at UTINAM [14, 15], I use here a convention which is at the opposite of that usually used for graphite in which perpendicular and parallel directions are defined with respect to the c-axis (perpendicular thus usually means parallel to the graphite surface plane, whereas here it means perpendicular to the local plane of 3 nearest neighbors).

The atomic polarizability tensors can then be computed in the nanostructure global frame $(\vec{u}_x; \vec{u}_y; \vec{u}_z)$ by simple geometric transformations, as:

$$\overleftrightarrow{\alpha}_i = R^{-1} \overleftrightarrow{\alpha}_i^{local}(\omega) \cdot R \tag{5.6}$$

by using the rotation matrix R that connects the local frame to the global frame.

However, carbonaceous nanostructures may also contain C atoms that are not surrounded by three carbons. For instance, C atoms located at boundary sites or at defect edges of the nanostructure may have only one or two carbon neighbors. For these atoms, which cannot be considered at all as sp^2 hybridized carbons, isotropic polarizability tensors are rather defined, being characterized in a first approximation by the value $\alpha_i^{iso} = (2\alpha_{i,||}^{local} + \alpha_{i,\perp}^{local})/3$.

In both cases (three nearest neighbors or not), the polarizabilities should be regularized in order to compute the field created on one atom by a dipole on a nearest neighbor. Indeed, in that case, the dipolar approximation is not valid since electronic clouds of these two atoms interpenetrate each other. If that effect is not taken into account, polarization catastrophes can occur (see e.g. [34]). To avoid this, several regularization procedures have been proposed, among which the convolution of the electric field propagator introduced in Eq.5.4, by one spherically symmetric function(s) representing an approximated radial distribution function (RDF) of the electrons around the nucleus of the atom at $\vec{r}_j$ which induced dipole creates the field at $\vec{r}_i$ [35]. The special case of a Gaussian RDF was already presented in [36]. Later, Mayer introduced a propagator regularized by 2 Gaussian RDFs, in case of another induced dipole being at $\vec{r}_i$[37]. The expression in these papers are static approximations that are valid in the limit that the wavelength of the incoming plane wave is much bigger than the distance between the 2 atoms which is always valid in our case.

A cornerstone in any DDA code results from the choice of a formula for the effective polarizability values that are used to calculate the dipoles (physical and theoretical problem). Similarly, in the PDI approach, a way to compute the frequency-dependent polarizabilities for each atom must be defined. Since we could not do it with plain DFT, we followed the same path than in DDA and computed atomic polarizabilities from the atomic polarizabilities of carbon atoms in graphite (cf. above) themselves derived from parametrizations of graphite complex permittivities, through an adapted Clausius−Mossotti relation, using depolarization factors originally computed by Senet for the static case[38] and later confirmed by Andersen and Bonderup[39]. This will be detailed in the next paragraph.

5.3 Results for fullerenes

5.3.1 Parameters and validation

Here, the main goal is to compute the optical properties of carbonaceous nanostructures modeling soot nanoparticles. As mentioned above, this requires the prior knowledge of the atomic polarizability tensors $\overleftrightarrow{\alpha}_i(\omega)$ associated with the C atoms forming the nanoparticles, and thus it depends on the values assigned to the ($\alpha_{i,||}^{local}$) and $\alpha_{i,\perp}^{local}$ components. In addition, the polarizability tensors may be isotropic or anisotropic depending on the local neighboring of the C atoms (i.e., depending in this approach on the number of next neighbor C atoms).

To calculate these polarizability tensors, different sets of dielectric constant values available in the literature for carbon atoms in graphite[40, 41, 42, 43] were tested, the conversion from dielectric constant to polarizability being done through the generalized Clausius−Mossotti relation as:

$$\frac{N}{V}\frac{\alpha_{i,a}^{local}(\omega)}{\epsilon_0} = \frac{\epsilon_{i,a}(\omega)-1}{1+B_a(\epsilon_{i,a}(\omega)-1)} \quad . \tag{5.7}$$

where the index a labels one of the three principal directions defining the local basis frame and N/V is the atomic density. The coefficients B_a are the depolarization factors assumed here to be equal to those of graphite, i.e., $B_\perp = -0.606$ and $B_{//} = 0.803$ [38, 39]. Note that taking $B_\perp = B_{//} = \frac{1}{3}$ in Eq. 5.7 would lead to the usual Clausius−Mossotti relation[44, 45].

Of course, these electric susceptibility parametrizations (and thus, the polarizability values used here) have been optimized for graphite and their application to soot could be questionable although soot nanoparticles are actually made of graphite-like nanoclusters[7].

Thus, to investigate the transferability of these parameters to round shaped nanostructures such as soot nanoparticles, the polarizability per unit volume of the C_{60} and C_{70} fullerenes were calculated using the three sets of parameters. This calculation has been based on the PDI approach[26], where the polarizability of the carbonaceous nanostructure is directly computed from the knowledge of the atomic polarizabilities through the following equations[14, 15] :

$$\vec{\mu}(\omega) = \overleftrightarrow{\alpha}(\omega)\vec{E}_0(\omega) = \sum_{i=1}^{N}\vec{\mu}_i(\omega) = \sum_{i=1}^{N}\overleftrightarrow{\alpha}_i(\omega)\vec{E}_{loc}(\vec{r}_i,\omega) \tag{5.8}$$

where $\vec{\mu}$ is the total electrical dipole moment of the carbonaceous nanostructure, $\overleftrightarrow{\alpha}(\omega)$ is the dynamical polarizability tensor of the carbonaceous nanostructure containing N carbon atoms and $\vec{E_0}(\omega)$ is the external homogeneous electric field applied to the system. $\vec{\mu}_i$ is the dipole induced on atom i by the local electric field $\vec{E}_{loc}(\vec{r}_i, \omega)$ at its location $\vec{r}_i$ (Eq. 5.4). $\overleftrightarrow{\alpha}_i$ defines the dynamical polarizability tensor of atom i calculated as mentioned above using parameters coming from graphite data. Then, imposing an unit field $\vec{E_0}$ successively along the three coordinate axes $(\vec{u}_x, \vec{u}_y; \vec{u}_z)$ of the global frame, we can easily get the three columns of the polarizability tensor $\overleftrightarrow{\alpha}$ of the carbonaceous nanostructure from Eq. 5.8.

The application of graphite data to predict properties of fullerenes has been already discussed in detail by Andersen and Bonderup[39] which pointed out some inconsistency between various sets of data, especially concerning the values for $\epsilon_\perp$. However, due to the lack of any reliable set of parameters specially suited for carbon atoms in curved structures such as soot nanoparticles, using parameters optimized for graphite still remains unavoidable.

The polarizability values calculated with the three selected sets of parameters have then been used to determine the function $\mathrm{Im}(-1/\epsilon)$, through the usual Clausius−Mossotti relation

$$\sum_i N_i \alpha_i = \frac{3\epsilon_0(\epsilon_r - 1)}{\epsilon_r + 2} \tag{5.9}$$

where N_i represent the number of constituent elements by unit volume, with $1/N_i \approx 703,34 \mathring{A}^3$ by molecule in a cubic face centered (cfc) crystal of C_{60} of lattice parameter $a = 14.117$ Å.

The theoretical curves are given in Fig 5.1 for both C_{60} (Fig 5.1a) and C_{70} (Fig 5.1b) fullerenes together with the corresponding experimental curves [46] for comparison. The theoretical curves in Fig 5.1 exhibit two broad peaks that can be related to the experimental peaks characterizing collective excitations of valence electrons. For the two fullerenes considered here, the first peak (corresponding to π plasmon[47]) has its maximum between 6 and 7 eV, whereas for the second peak (which corresponds to $\sigma + \pi$ plasmon[47]) the maximum is obtained between 22 and 28 eV, depending on the parametrization that is used in the calculations.

The comparison with the experimental curves shows that the three different parametrizations used here appear to be quite relevant for describing the features below 8 eV, although the results obtained with the parameters given by Draine et al[40, 41, 42] seems slightly more accurate than those issued from Djurisic's work[43]. In contrast, theoretical results obtained by using optical constants coming from EELS and ellipsometry[43] seems to

better reproduce the experimental features above 8 eV, although a small shift (of around 2 eV) is evidenced for the maximum position of the main peak. Note that, as expected, some resonances related to excitations from π to π^* orbitals for the C_{60} and C_{70} molecules (peaks below 5 eV) [48] cannot be accounted for by any parametrization optimized for graphite where such transitions are not possible due to symmetry considerations.

To conclude, it appears that the parameters given by Draine et al.[40, 41, 42] for graphite can also be used with reasonable confidence to get at least qualitative results for fullerenes, and more generally spherical carbonaceous particles[20, 39], especially when restricting the calculations to the visible and near-UV zone, as in the following.

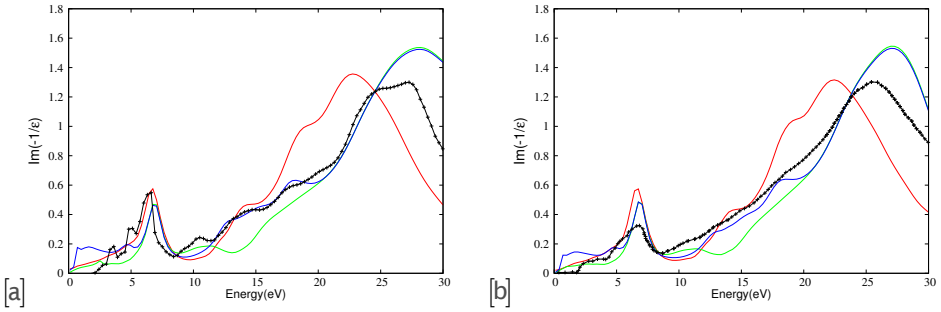


Figure 5.1: Comparison between the experimental Loss function $\mathrm{Im}(-1/\epsilon)$ (black curve) for a cristal of (a) C_{60} and (b) C_{70} [46] and the theoretical curves computed with three different sets of optical constants derived from graphite data; red, green and blue curves correspond to parametrizations from Ref.[40, 41, 42] and Ref.[43] (for optical and for EELS data), respectively.

5.3.2 Fullerenes of increasing radius

In this section, the interaction of isolated fullerene molecules with light has been simulated, in order to study their optical properties in the UV zone, as a function of their increasing size. As the extinction cross section is mainly dominated by absorption, I first seek to compare the photoabsorption cross section C_{abs} for a C_{60} fullerene with the experimental data reported in the literature[49, 50] before extending the study to larger fullerenes. The comparison given in Fig 5.2 between our theoretical results and the experimental curve shows that our approach reproduces quite well the main peak position around 6 eV, as already evidenced in the previous section when calculating $\mathrm{Im}(-1/\epsilon)$. Again this figure points out that calculations based on the optical constants derived from graphite data cannot reproduce some of the C_{60} resonances below 5 eV.

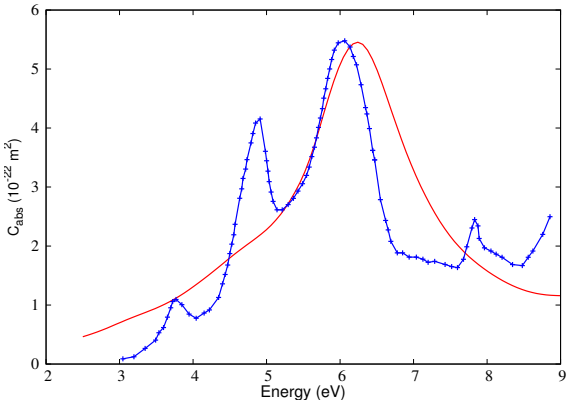


Figure 5.2: Comparison between the photoabsorption cross section calculated for a C_{60} fullerene (red curve) and that reported by [50] (blue curve). Calculations have been performed by using the graphite optical constants given by Draine *et al.*[40, 41, 42].

Then, calculations are extended to larger fullerenes, namely C_{240}, C_{540}, C_{960} that are icosahedral fullerenes like C_{60}, and C_{180}, C_{320} and C_{1280} that are triacontahedral fullerenes. The corresponding results are given in Fig 5.3 in the visible and near-UV range, i.e., typically between 150 and 550 nm (corresponding to the [2.3 - 8.3] eV range). Note that we used wavelengths in nm for the x axis of the MAC curves (and not energies as in the C_{abs} case), for coherence with the corresponding literature.

The curves in Fig 5.3 show that the maximum position of the resonance peak is shifted to high wavelength values (by about 45 nm) and that its maximum intensity increases when the size of the fullerenes increases. An interesting consequence of these two features is that for wavelengths lower than approximately 200 nm the mass specific absorption cross section (MAC) of fullerenes decreases with their radius, whereas it increases for larger wavelengths.

These results are in accordance with those of previous works that used either a simplified model[51] or an approach based on the PDI method[52] for the calculations of dynamical polarizabilities of fullerenes.

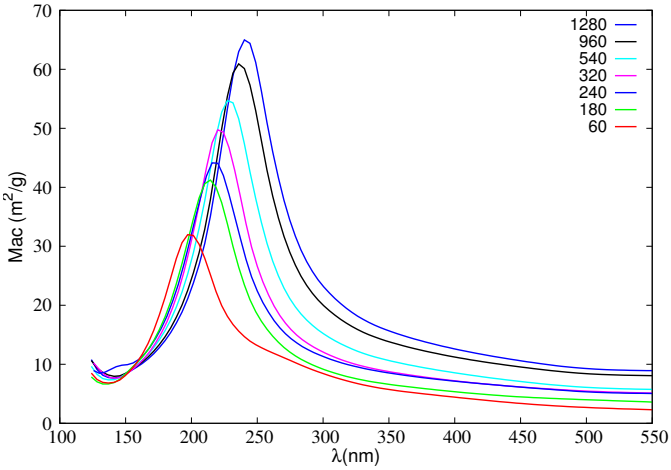


Figure 5.3: Computed mass absorption cross section (MAC) for the icosahedral C_{60},C_{240},C_{540},C_{960} and the triacontahedral C_{180}, C_{320},C_{1280} fullerenes.

Because in this model we can use either isotropic or anisotropic polarizability tensors to describe C atoms, depending for instance on their number of neighbors, it was interesting to study the influence of such a choice on the MAC curves calculated for different fullerenes. Of course, in such structures, the C atoms are all surrounded by 3 neighbors as in graphite, and considering that they could be represented by isotropic polarizability may appear surprising at first sight. Nevertheless, this allows the characterization of the influence of the parametrization on our results by comparing MAC curves obtained for the same nanostructure but for two different representations of the polarizability tensors of the C atoms.

As an illustration, the corresponding results are given in Fig 5.4 for the smallest (C_{60}) and the largest (C_{1280}) fullerenes considered here.

Interestingly, for C_{60}, both isotropic and anisotropic polarizability tensors give similar MAC curves, especially when considering the position of the resonance peak around 200 nm. In contrast, for C_{1280}, not only strong differences in the MAC intensity but also a large shift of the resonance peak (of about 30 nm) are obtained when using different hypotheses for the polarizability tensor of the C atoms. This could be related to the fact that, for such large fullerene, each C atom and its three nearest neighbors are approximately located in the same plane, as in graphite, thus enhancing the influence of the differences between isotropic and anisotropic parametrization. Moreover, this indicates that, at least in this approach and for large structures, sp^2 hybridized carbon atoms will lead to much stronger absorption than C atoms represented by isotropic polarizabilities resulting from an average of the anisotropic values. Interestingly, this could give us an useful tool

to discriminate between strongly and weakly absorbing carbons in further modeling, and thus would help, for instance, at representing the differences experimentally evidenced between elemental and organic carbons[53].

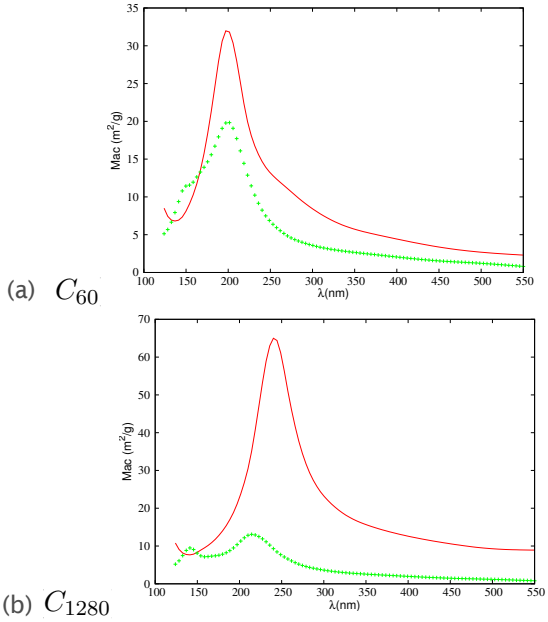


Figure 5.4: Computed mass absorption cross section (MAC, in m^2/g) obtained when using isotropic (green curve) and anisotropic (red curve) atomic polarizabilities for (a) C_{60} and (b) C_{1280} fullerenes.

5.4 Results for soot nanoparticles

5.4.1 Soot nanoparticle models

The results presented above have shown that parameters optimized for graphite can reasonably well reproduce the optical properties of fullerenes, in accordance with previous conclusions[20, 39]. The transferability of these parameters to various carbonaceous systems can thus justify using them for modeling the MAC of soot nanoparticles. As mentioned above, calculating the MAC with the PDI approach requires not only the knowledge of the atomic polarizabilities (taken here as equal to those of carbons in graphite) but also of the atom positions in the carbonaceous nanostructures.

Thus in this study, four different primary soot nanoparticles have been used, on the basis of a previous work devoted to water adsorption on soot[10, 13].

Such approach allows us to evaluate qualitatively the dependence of soot optical properties on particle morphology at the atomic scale.

The first nanoparticle is generated by randomly scattering small clusters of 19 carbon atoms on concentric spheres arranged in an onion-like structure[10]. This small cluster, referred below as the C_{19} unit, is made of five fused benzene rings. One hundred and thirteen of these C_{19} units (corresponding to a total number of 2147 carbon atoms) have been randomly scattered on the surface of four concentric spheres of increasing radii (from 9.6 to 20.7 Å), the separation between two successive spheres being equal to 3.4 Å, in accordance with experimental observations for combustion soot [54]. For the scattering of the C_{19} units on the surface of these spheres, a minimum distance of 3.80 Å has been imposed between the nearest neighboring carbon atoms of two adjacent units on the same sphere. The relative orientations of two adjacent C_{19} units have been randomly distributed. The corresponding primary soot nanoparticle, referred hereafter as the S_{units} soot nanoparticle is shown in Fig. 5.5a.

In addition to this empirically generated primary soot nanoparticle, three other nanoparticles have been built starting from the optimized structures of carbon buckyonions (i.e., multi-shell fullerenes) containing four carbon layers arranged in a concentric way just as S_{units}. However, to model the presence of holes and nanopores in the (defective) structure of primary soot nanoparticles, C atoms have been randomly removed from the initial buckyonion structure. Then, the resulting structures have been relaxed in a molecular dynamics simulation run performed at 298 K on the canonical N,V,T, ensemble, in which the adaptative intermolecular reactive empirical bond order (AIREBO) potential has been used to describe the carbon–carbon interactions[55]. It is worth noting that the corresponding structures are thus not based on a random scattering of units of same size (as S_{units}) but rather on a random distribution of holes. These particles will be referred below as S_{holes} soot nanoparticles.

Two of these S_{holes} soot nanoparticles have been based on the structure of the four-shell $C240@C540@C960@C1500$ fullerene, relaxed after removing 1033 and 1107 carbon atoms, respectively, to model different localization of carbon atoms in similar structures. They contain 2207 and 2133 carbon atoms respectively, and are characterized by an external radius of about 22 Å. These S_{holes} nanoparticles are thus similar to S_{units} with respect to the total number of C atoms, although they are slightly larger in size. The main difference comes from the size of the internal cavity, which is determined here by the radius of the smallest fullerene (C_{240}) embedded in the buckyonion. It it indeed twice smaller for the two S_{holes} (radius value equal to about 4.3 Å) than for the S_{units} soot nanoparticles (radius value equal to about 9.6 Å). The third S_{holes} soot nanoparticle is thus based on the structure of the larger

four-shell $C540@C960@C1500@C2160$ fullerene, i.e., a buckyonion that is characterized by an internal cavity of size similar to the one in S_{units}, but it contains a much larger number of C atoms. However, it was not possible to get any stable structure when removing a too large number of atoms in this buckyonion. So, an S_{holes} soot nanoparticle containing 3774 carbon atoms was chosen. The relaxed structures of the three S_{holes} nanoparticles are shown in Fig. 5.5b,c,d.

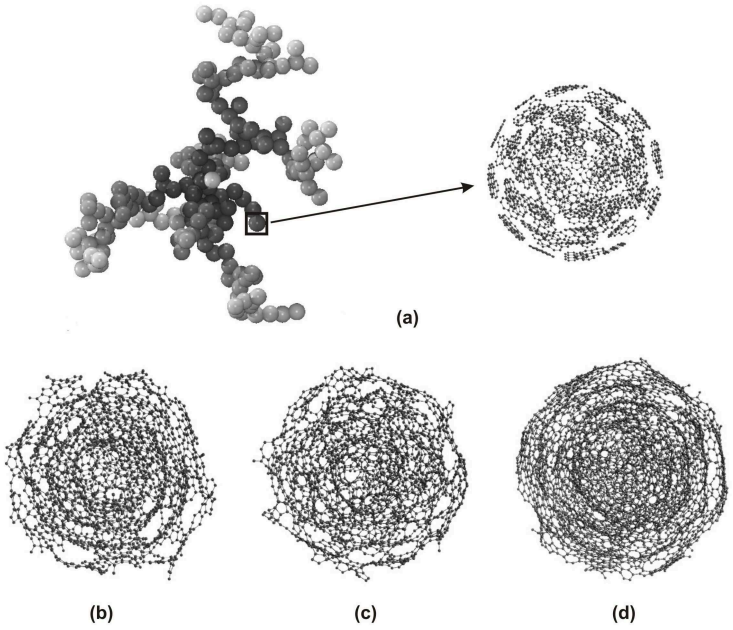


Figure 5.5: (a) Simplified representation of a soot aggregate made of agglomerated primary nanoparticles with, on the right hand side of the figure, a picture of the the S_{units} nanoparticle containing 2147 C atoms that is used to model a primary nanoparticle of soot in the present approach. Additional models for these primary particles, based on the S_{holes} nanoparticles, are also shown at the bottom of the figure where (b), (c) and (d) correspond to S_{holes} nanoparticles containing 2133, 2206 and 3774 C atoms, respectively. See text for the definition of the S_{units} and S_{holes} nanoparticles.

Of course, building soot models as described above is completely arbitrary. Nevertheless, the primary nanoparticles generated this way present the main geometric characteristics of soot collected in flames[62] or emitted by aircraft[8], i.e., graphite-type layers arranged in an onion-like structure, although they are somewhat smaller (about $4 - 4.5$ nanometers of diameter here). Indeed, considering larger particles in this PDI calculations would be rather time consuming without any further approximations[15] and we

thus choose to limit the present work to nanoparticles containing a relatively small number of carbon atoms.

Note that many different particles can be generated using this procedure. However, the calculations have been restricted to only four particles, as an illustration of the approach presented here. Moreover, as it will be shown below, this (limited) set of examples is nevertheless sufficient to show how the absorption properties can be related to the atomistic structure of soot nanoparticles.

5.4.2 Mass absorption coefficient of soot nanoparticles

In this section, the calculation of the mass absorption coefficient is presented for the four nanoparticles generated above and considered as independent nanoparticles, where the attention is focused on how spectroscopic information could be used to differentiate morphological information on soot nanoparticles at an atomistic scale. This differs from a lot of previous experimental and theoretical studies which were carried out by considering morphology dependence of absorption as a function of the fractal structures of soot aggregates, thus not considering individual nanoparticles[17, 67, 68, 69, 70].

The corresponding results are shown in Fig 5.6. Information concerning the geometrical characteristics of the nanoparticles considered as well as the position of the main peak in the MAC curves are given in Table 5.1 together with the calculated MAC values for three different wavelengths.

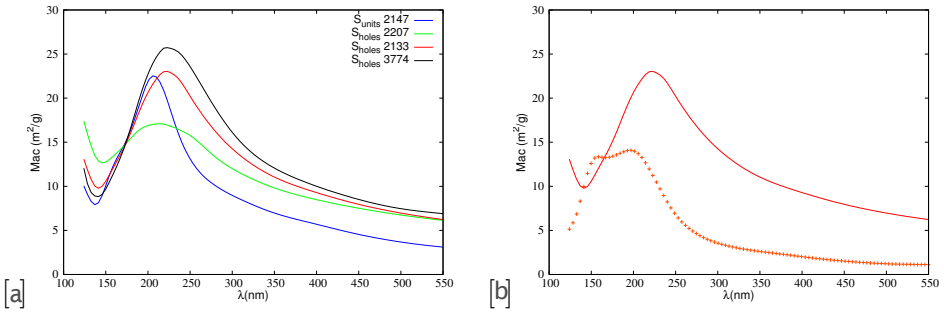


Figure 5.6: (a) MAC curves (in m^2/g) computed for various carbonaceous nanoparticles as a function of the wavelength (in nm). Blue, green, red and black curves correspond to S_{units} and S_{holes} with 2133, 2207, and 3774 carbon atoms, respectively. (b) Influence of the chemical composition on the S_{holes} (2133 C atoms) MAC curve : red and orange curves correspond to consideration of anisotropic (solid line) and isotropic (crosses) carbon polarizabilities in the calculations, respectively.

As shown in Fig. 5.6a, in the UV zone, the MAC curves for the soot nanoparticles are characterized by a large absorption peak, the maximum of which being shifted by about 20 nm from S_{units} to the largest S_{holes} (containing 3774 C atoms).

This can be related to what has been obtained for fullerenes, i.e., the position of the resonance peak is shifted to high wavelength values when the size of the nanoparticles increases. However, a shift of 7 nm is also obtained for two particles of similar size and built on a similar initial structure (S_{holes} containing 2207 and 2133 atoms). This indicates that not only the size but also the structure of the nanoparticle at the atomic level may influence the position of the absorption peak.

In fact, a careful analysis of the differences between the soot nanostructures considered here shows that, besides size and number of atoms, these particles also differ by the ratio between isotropic and anisotropic carbons, i.e., carbons having three (anisotropic) or less than three (isotropic) next neighbors. Regarding this criterion, the maximum of the absorption peak shifts to higher wavelengths when increasing the number of anisotropic carbons. In other words, because the anisotropic *vs.* isotropic character is defined here with respect to the graphite polarizability values (i.e., anisotropic carbons are characterized by the polarizability tensor of graphite atoms), such an effect in the absorption spectrum could be somehow related to the ratio between aromatic-like and aliphatic-like carbons in the nanoparticle.

structure	atoms	R_{in} (Å)	R_{out} (Å)	C_{iso}/C	peak position (nm)	Mac (250 nm) m^2/g	Mac (405 nm) m^2/g	Mac (550 nm) m^2/g
S_{unit}	2147	9.6	20.73	0.60	207	13.53	5.57	3.07
	2207	4.3	22.32	0.45	214	15.89	8.34	6.10
S_{hole}	2133	4.5	22.58	0.30	221	20.61	9.25	6.23
	3774	8.2	23.50	0.18	226	25.30	10.29	7.02

Table 5.1: Morphological details of the soot nanoparticles considered in the calculations and the corresponding computed MAC values for 3 different wavelengths. R_{in} corresponds to the radius of the internal cavity defined by the inner layer of the nanoparticle whereas R_{out} represents the radius of the nanoparticle, defined by its outer layer. Note that C_{iso}/C represent the proportion of C atoms represented by isotropic polarizabilities *vs.* the total number of C atoms in the nanoparticle.

To illustrate this influence on the MAC calculations, Fig. 5.6b shows the results obtained when considering only one specific soot nanoparticle (S_{holes} with 2133 atoms, for instance), but changing the parameters assigned to the carbon atoms. For illustration, we could consider the limiting (unrealistic) case for which all carbons are represented by the same isotropic polarizability tensor (orange curve). The MAC spectrum obtained in this case strongly differs from the one calculated for the initial particle containing only 30 % of isotropic carbons (red curve). Indeed, it is characterized by a double

peak, the maximum of which being shifted by 22 nm from the maximum calculated for the initial S_{holes} particle. This results clearly indicates that the chemical composition of the soot nanoparticle, modeled here by atoms with different types of polarizability tensors, may have a sufficiently strong influence on the MAC signals to allow detection of chemical differences by using spectroscopic measurements, especially in the spectral region of the resonance peak.

However, coming back to realistic nanoparticles (Fig. 5.6a) and regarding the MAC values at a given wavelength (and not only the position of the absorption peak at its maximum value), it clearly appears that the amplitudes of the differences calculated for different soot particles strongly depends on the spectral range. Indeed, Fig. 5.6a and values given in Table 5.1 for three different wavelengths clearly show that above about 350 nm, the MAC values are similar for the three S_{holes} nanoparticles which however differ by the size of their internal cavity, the number of carbon atoms and their ratio of isotropic to anisotropic carbons (i.e., their chemical composition). This indicates that, in this spectral region, differences in soot composition would not have any strongly visible influence on the MAC values. It should be noted however that differences in MAC values are evidenced between S_{holes} and S_{units} nanoparticles in this spectral range, without any clear and definite explanation for this results that may deserve more detailed investigations. S_{units} is indeed sligthly smaller than the other particles and it contains a very high proportion of graphite-type atoms (i.e., C atoms with 3 next neighbors). Anyway it does not correspond to any relaxed structure and, in that sense, this nanoparticle is certainly less realistic than the others.

These findings can be compared to the results issued from a compilation of various data indicating that, at 550 nm, there is a consistent mean value of 7.5 $\pm$ 1.2 m^2/g for the MAC of fresh light-absorbing carbon over a wide range of data available in the literature[17]. Interestingly, this value is not far from the one calculated here for the three S_{holes} nanoparticles (about 6.45 $\pm$ 0.5 m^2/g at 550 nm) whereas it is about twice that calculated for S_{units}.

Such a semi-quantitative agreement between these results based on an empirical modeling of soot nanoparticles and experimental or theoretical values obtained from other approaches reinforces the conclusion that, in this region of the spectrum, MAC values certainly do not significantly differ from one example of soot to another.

To summarize, the results obtained here indicate that MAC measurements could give information on the atomic details of soot nanoparticles only if they are performed in a well-suited wavelength range, i.e., at wavelengths

typically between 200 and 350 nm (when considering the nanoparticles modeled here).

5.4.3 Comparison with analytical approaches

To evaluate the improvement given by the PDI approach and the atomistic description of the primary soot nanoparticles, we have also compared the results obtained in the present work with those calculated by using analytical models based on classical macroscopic electromagnetic theory, following the ideas of Michel et al[20].

First, it should be noted that carbonaceous materials are strong absorbers of electromagnetic radiation and thus scattering is negliglible. As a consequence, the analytical approach can be restricted to extinction properties that can be characterized by the extinction per volume calculated, for a spherical particle made of carbonaceous continuum material without atomic structure, with a central empty void, as[66]

$$\eta_{ext} = 3k\mathrm{Im}\left[\frac{(1-\rho)(\epsilon_\perp u_+ - 1)(\epsilon_\perp u_- - 1)}{(\epsilon_\perp u_- - 1)(\epsilon_\perp u_+ + 2) - \rho(\epsilon_\perp u_+ - 1)(\epsilon_\perp u_- + 2)}\right] \tag{5.10}$$

where

$$u_\pm = \pm\frac{\sqrt{1 + 8\epsilon_{//}/\epsilon_\perp} \mp 1}{2}; \rho = \left(\frac{R_{in}}{R_{out}}\right)^{u_+ - u_-} \tag{5.11}$$

and $\epsilon_\perp$ and $\epsilon_{//}$ are the parallel and perpendicular components of the dielectric tensor of carbon atoms in graphite, following the convention used in the present paper (see Section 2). R_{in} is the radius of the internal void whereas R_{out} represents the radius of the entire nanoparticle.

Two types of spherical particles have been considered for comparison between PDI and analytical approaches, namely the primary soot nanoparticles S_{units} and S_{holes} on the one hand and, on the other hand, the corresponding bucky-onions of fullerene that have been used to build these nanoparticles. The analytical calculations have been performed by considering spherical particles characterized by internal (R_{in}) and external (R_{out}) radii similar to those of the S_{holes}, S_{units} and buckyonions considered for the comparison. Moreover, in the analytical model, we have taken a carbon density equal to one carbon atom per 1.8788 $Å^3$, similar to that of graphite.

As it can be seen on Fig. 5.7a, the PDI and analytical approaches give very similar results when considering bucky-onion fullerenes. This first conclusion not only clearly supports the accuracy of the PDI approach used here but also confirms that the analytical approach based on macroscopic electromagnetic theory could be safely used for modeling the optical answer of homogeneous spherical particules. In contrast, the MAC curves are significantly different when considering the more realistic S_{holes} and S_{units} primary soot nanoparticles, thus illustrating the role of the atomic defects in the structure of soot. Indeed, for these S_{holes} and S_{units} nanoparticles, both intensities and positions of the resonance peaks differ between the PDI and analytical approaches. More interestingly, for the S_{holes} nanoparticles (which are much less spherical than S_{units} due to the local rearrangement of the structure around defect sites upon optimization), MAC values at large wavelengths differ by almost a factor two between the two approaches, the values obtained using the PDI approach being much closer to the experimental measurements than the values given by the analytical approach.

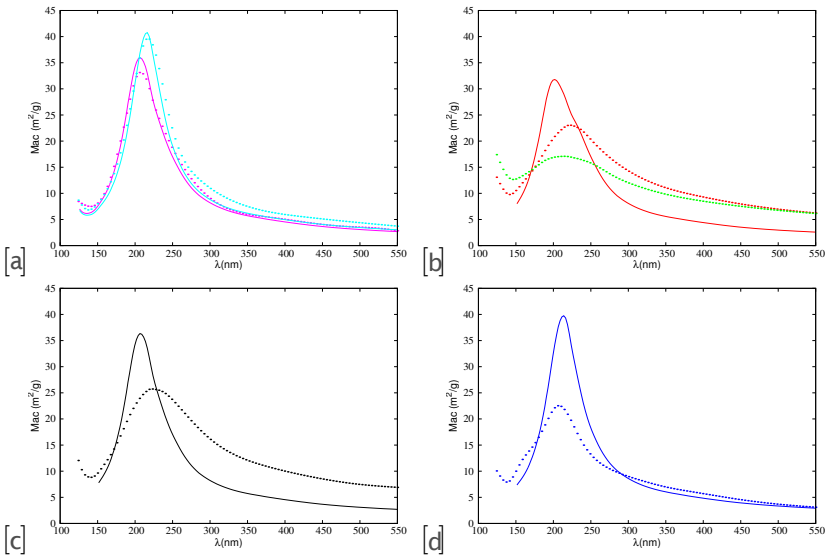


Figure 5.7: Comparison between the MAC curves (in m^2/g) computed as a function of wavelength (in nm) by using either analytical (full curves) or PDI approach (dotted curves) for various carbonaceous nanoparticles : (a) Buckyonion $C240@C540@C960@C1500$ corresponding to S_{holes} containing either 2207 or 2133 atoms (pink curves) and buckyonion $C540@C960@C1500@C2160$ corresponding to S_{holes} containing 3774 atoms (light blue curves). (b) S_{holes} containing 2207 and 2133 atoms (green and red curves, respectively), (c) S_{holes} containing 3774 atoms (black curve), and (d) S_{units} containing 2147 atoms (blue curve).

Such differences between the analytical and PDI approaches can be unambiguously related to the presence of defects in the atomistic structure of our soot models. They clearly emphasize the limits of the classical macroscopic electromagnetic theory for calculating the optical properties of defective structure that cannot be considered simply as homogeneous spherical particles.

Finally, it is interesting to note that such conclusions have already been reached in a previous work performed at Besancon [14] although they were based on the calculations of the total polarizability of the nanoparticles for three incident energies, only.

5.4.4 Influence of the internal structure

In the previous section, only onion-like particles of soot presenting an empty internal cavity have been considered, for instance, the S_{holes} cavity defined by the size of the smallest embedded fullerene. In reality, the central region of the onion can also be filled with carbon atoms characterized by more or less well-organized structures[63, 64, 65]. The influence of such carbon nanostructures located inside the inner cavity has been studied theoretically by Henrard et al. [66] and Michel et al. [20], for instance, by using analytical approaches. It has been proved to have an important effect on the optical properties of the soot nanoparticle, depending on the disordered vs. crystalline character of these carbons[20, 66].Thus, in this PhD work, I used the PDI approach to calculate the MAC of primary soot nanoparticles filled with various carbonaceous nanostructures, on the basis of an atomistic description of the corresponding particles.

For instance, I present here the results obtained when considering as initial structures the bukyonions $C540@C960@C1500$ and $C540@C960@C1500@C2160$ relaxed after removing 1157 and 1386 carbon atoms, respectively. The MAC of these two particles has thus been calculated before and after adding at their center a small piece of graphite or an identical number of carbon atoms distributed on small dehydrogenated Polycyclic Aromatic Hydrocarbons (d-PAHs) randomly arranged at the center of the particles, for comparison (*cf.* Fig. 5.8). Note that the final structure of the nanoparticles modeled this way was not relaxed because this would have re-organized the internal part of the particle. Thus, the non-relaxed particles modeled here have to be considered as ideal cases, only. An important feature to mention is that geometries for the nanostructures embedded at the center of the nanoparticles do not change the global ratio between anisotropic and isotropic C atoms (in other words, the ratio between C atoms having three next neighbors and the other C atoms).

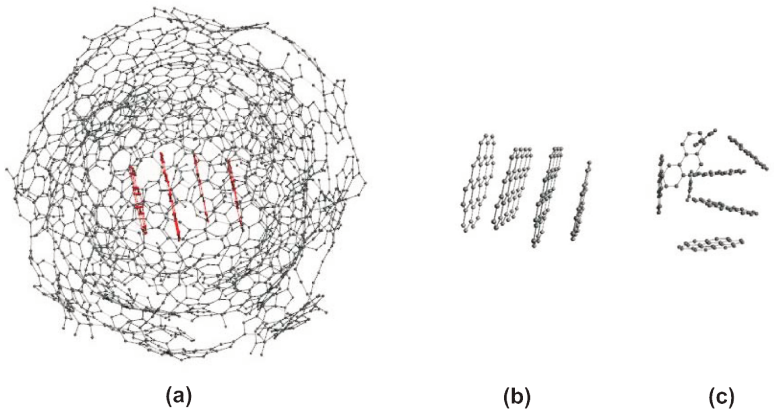


Figure 5.8: (a) Structure of the S_{holes} soot nanoparticle containing 1970 C atoms and including a small piece of graphite at its center (represented in red for clarity); (b) Example of a small piece of graphite that can been included at the center of the soot particles for the calculations of the MAC curves; (c) Example of randomly distributed small dehydrogenated Polycyclic Aromatic Hydrocarbons that can been included at the center of the soot particles for the calculations of the MAC curves.

The detailed information on these systems and the corresponding optical properties are given in Table 5.2 and their MAC curves are shown on Fig. 5.9. It is worth noting that the MAC curves calculated when considering well-ordered graphite and randomly scattered d-PAHs at the center of the nanoparticles do not exhibit any significant difference, and thus only the MAC curves corresponding to the latter case are given in the Figure.

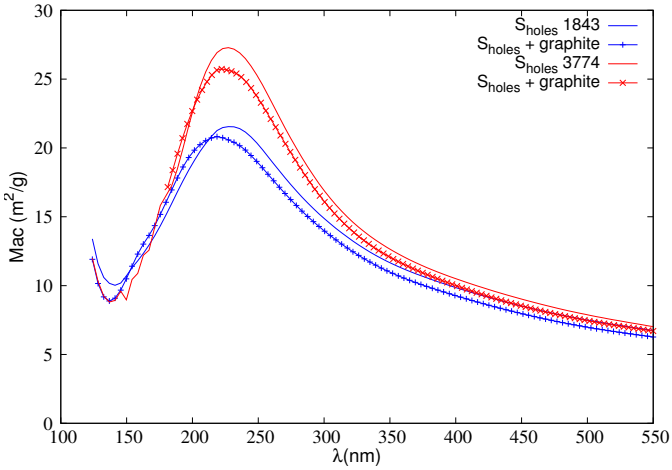


Figure 5.9: Comparison between the MAC curves (in m^2/g) computed as a function of wavelength (in nm) for two carbonaceous nanoparticles with (crosses) and without (solid lines) a small piece of graphite added at their center. Blue and red curves correspond to S_{holes} particles with 1843 and 3774 carbon atoms, respectively.

In contrast Fig.5.9 shows that including a carbonaceous nanostructure (graphite or d-PAHS) at the center of a primary soot nanoparticle leads to a shift to lower wavelengths (by 11 nm and 4 nm, respectively, for the two nanoparticles considered here) of the maximum of the MAC resonance peak. Lower MAC values are also calculated for the filled nanoparticles at high wavelengths (i.e., larger than about 220 nm). These conclusions are similar to those previously obtained, on the basis of analytical approaches, for the extinction curves of soot nanoparticles[20].

Considering that both the size and the ratio of isotropic *vs.* anisotropic carbons are the same for a given empty or filled nanoparticle, the shift and lowering of the MAC curves can be attributed to the filling of the inner part of the nanoparticles. The present results thus confirm that the characteristics of the inner region of the primary soot nanoparticles may significantly affect their optical properties. However, although the expected differences in the MAC curves might be used to discriminate between filled and empty particles, it appears that they cannot give unambiguous information on the structuration of the carbon atoms inside the soot nanoparticles. In that sense, using atomistic simulations based on realistic force field models such as the AIREBO potential[55] used here could be of great interest to discriminate between different models of internal structure of soot nanoparticles, based on their relative stability in the calculations.

structure	atoms	R_{in} (Å)	R_{out} (Å)	C_{iso}/C	peak position (nm)	Mac 250 nm m^2/g	Mac 405 nm m^2/g	Mac 550 nm m^2/g
	1843	9.5	22.58	0.34	229	19.97	9.73	6.74
	1970	–	22.58	0.34	218	18.68	9.14	6.27
S_{hole}	3774	8.2	23.50	0.18	226	25.30	10.29	7.02
	3888	–	23.50	0.19	222	23.41	10.12	6.70

Table 5.2: Morphological details of the soot nanoparticles considered in the calculations and the corresponding computed MAC values for 3 different wavelengths. R_{in} corresponds to the radius of the internal cavity defined by the inner layer of the nanoparticle whereas R_{out} represents the radius of the nanoparticle, defined by its outer layer Note that C_{iso}/C represent the proportion of C atoms represented by isotropic polarizabilities *vs.* the total number of C atoms in the nanoparticle.

5.5 Absorption and extinction curves of PAHs in the interstellar medium

Astronomical observations of the interstellar medium (ISM) indicate active carbon chemistry particularly involving large carbon species (tens to thousands of atoms) at the boundary between large molecules and small solid grains. Spectroscopic properties of these species in the middle infrared region (5-15 microns) indicate that polycyclic aromatic hydrocarbon molecules (PAHs) could be a good model for the study of interstellar species. Thus, in addition to the chemical reactivity and the health impact of these species (already mentioned in this manuscript), the absorption/extinction properties of PAHs gained much attention in astrophysics community, especially for tentative interpretations of the broad absorption band at 2175 Å.

Thus, in the astrophysics team at UTINAM laboratory, the evolution of PAHs and of their aggregates in the interstellar medium (ISM) is studied by Dr. Julien Montillaud, on the basis of numerical simulation tools. From the astrochemical point of view, an important goal is to predict the photostability of PAHs in the interstellar medium. A species can be considered as photostable as long as it can conserve some of its peripheral H-atoms. When a PAH looses all its H-atoms, one is left with a carbon cluster, which usually presents a wealth of isomers [56] whose spectra cannot account for the astronomical spectra.

In addition to the physicochemical properties of these species, J. Montillaud simulates the chemical kinetics of the formation of PAH aggregates in the ISM taking into account the specific physical conditions in this extremely dilute medium together with the high density of energetic photons (including far ultraviolet). Consideration of photodissociation events initiated by the multiple absorption of UV photons allows J. Montillaud to predict the spatial and temporal evolution of the charge and hydrogenation state of the PAH

species in the ISM, as well as to provide constraints on their size distribution. He has also shown that physicochemical properties of interstellar PAHs are consistent with the idea that they may be the precursors of interstellar fullerenes, recently identified in some regions of the ISM.

An important step of this research is the computation of how much energy can be absorbed independently by the PAHs. Then, an accurate value of their photochemical properties depends on the knowledge of each PAH's absorption cross section. However, although some cross section values are provided by databases like those of the Nasa Ames [57] and of Malloci [58], which are based on some experimental measurements, on the use of the DDA or of the TD-DFT methodologies, the corresponding studies are not an easy task. For that reason, a method like the PDI presented here, could be used to complement the calculations where more accurate methodologies starts to be computationally forbidden.

Thus, we decided first to test the validity of our PDI approach by considering the same systems as those previously studied by Duley et al. [59] who investigated the extinction related to small carbon particles consisting of aromatic rings similar to those of polycyclic aromatic hydrocarbon (PAH) molecules, but with varying degrees of hydrogenation, ionization, and amount of defects. In the work of Duley, extinction produced by various particles (see fig 5.10) were calculated using the DDA formalism with optical constants adapted from those of graphite to the considered species.

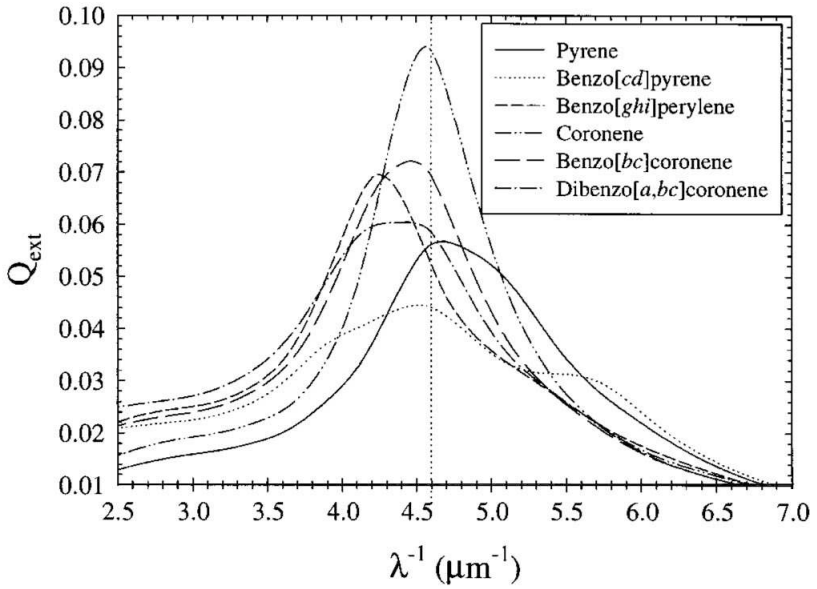


Figure 5.10: Extinction efficiencies of the dehydrogenated molecules [59].

Then, to perform the comparison between the results of the PDI and those of the DDA approaches, instead of the already discussed mass absorption coefficient (MAC) we rather compute a geometric cross section coefficient Q_{ext}, defined by the extension cross section C_{ext} normalized by a geometric factor, following the ideas presented in Ref. [59].

Our results, presented in Fig 5.11, show a qualitatively good agreement with the DDA results of Duley et al. (Fig 5.10) [59], especially when considering the position of the extinction peaks of the different species. The coronene curve is centered around the maximum position of the absorption feature (2175 Åor 4.59 λ^{-1}) and a small shift for the differents species is calculated, as a function of their geometry. Note that a quantitative comparison between our results and those of Duley would depend on the parameters used to derive the polarizability values of the carbon atoms and on the method chosen to compute the geometric cross section. Nevertheless, the qualitative agreement obtained here represents an encouraging indication on the accuracy of our PDI approach when applied to PAH properties.

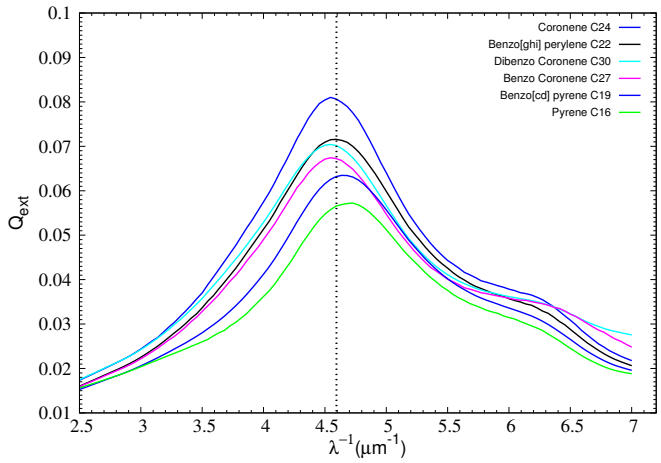


Figure 5.11: Extinction efficiencies of the dehydrogenated molecules

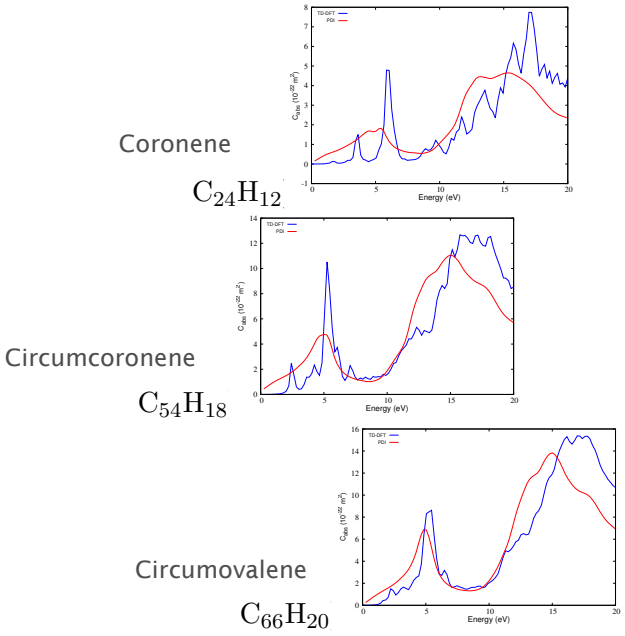


Figure 5.12: Computed absorption cross section (C_{abs} 10^{-22} m^2) obtained when using a PDI method (red curve) vs the results provided by Malloci et all obtained with TD-DFT.[58]

Thus, absorption cross sections for some PAH species have been calculated by using the PDI method (with carbon polarizabilities derived from graphite, considering all carbon atoms as anisotropic) and compared with the results provided by Malloci et al. ([58]) on the basis of TD-DFT calculations. The results of this comparison is given in fig 5.12.

As it is shown, the UV absorption spectrum provided by Malloci et all [58] on the basis of TD-DFT simulations (fig 5.12 a) are characterized by strong peaks that are connected to discrete $\pi - \pi^*$ transitions rather than by the broad giant resonance typical of the plasmon absorption in graphite. This can be easily understood by the fact that in hydrocarbons of finite size, collective excitations are not possible [60].

When compared to the TD-DFT results, the two absorption peaks calculated with the PDI method for the coronene molecule (fig 5.12 a) are significantly shifted to the low energy values. Moreover, as already emphasized in the previous sections, the parameters used in our PDI method cannot account for the discrete $\pi - \pi^*$ transitions because they are derived from graphite. However, as the molecule size increases, fig 5.12 (b,c) clearly shows a much better agreement between the curves obtained from the two methods (PDI and TD-DFT) and they even seem to converge for large systems, at least up to the energy region of 11 ev.

This result is consistent with the intuitive argument that, as well as the size of the carbonaceous cluster increases, the impact of the edge atoms onto the spectoscopical signal decreases and atomic polarizability values derived from graphite (and used in the PDI method) may become more suited for the corresponding systems.

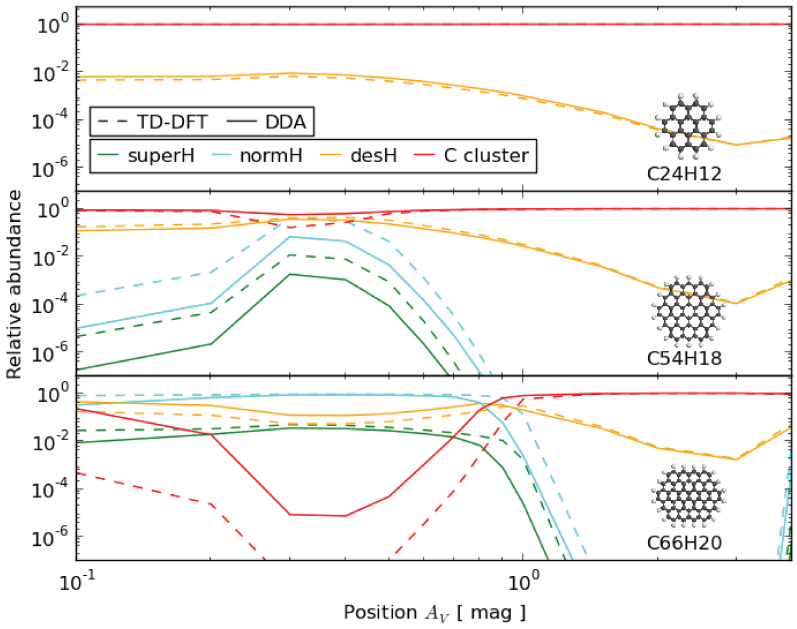


Figure 5.13: Relative abundance of different hydrogenation states for three PAHs as a function of their position in an interstellar cloud: comparaison between data coming from TD-DFT and DDA/PDI calculations.

Then, as mentioned before, a model was developped by Montillaud [61] which takes as an input, among other data, the UV absorption cross sections of PAHs, and computes, for a given PAH (C_nH_m), the abundance of each hydrogenation state (C_nH_p, $p = 0, m$).

Figure 5.13 presents the results of this model for three PAHs (coronene $C_{24}H_{12}$, circumcoronene $C_{54}H_{18}$, and circumovalene $C_{66}H_{20}$), as a function of their position in an interstellar cloud. The model was run using TD-DFT cross sections (dashed lines) coming from the database of Malloci and PDI cross sections (solid lines) calculated here. Taking into account that the important point for astrochemistry is to know which hydrogenation states is the most abundant one at a given position (because it is the one which contributes most to the observed infrared spectra at this position), it is worh

noting that the astrochemical model used by J. Montillaud predicts mostly the same species to dominate at a given position irrespective of the cross sections (TD-DFT or PDI) used. In other words, the differences between the TD-DFT and PDI cross sections lead to minor differences in the astrochemical calculations, only. This conclusion is very interesting for further work because it means that our PDI method can be a valuable alternative to quantum approaches for providing the astrochemical community with UV absorption cross sections. In addition, the efficiency of the PDI method makes it computationaly competitive to compute absorption cross sections for a large amount of species, especially large molecules like PAHs that are not included yet in the astronomical databases.

5.6 Conclusions

In this work, an atomistic approach to calculate the MAC curves of carbonaceous particles modeling primary soot nanoparticles and the extinction cross sections of PAH molecules has been used. The model is based on the knowledge of the atomic positions and polarizabilities inside the nanostructure under study. First, the fact that polarizability values coming from graphite data can be satisfactorily used to calculate the optical properties of round-shaped carbonaceous structures such as fulllerenes and carbon bucky-onions was confirmed. Then, various primary soot nanoparticles were built and used to compare their calculated MAC to study the influence of their atomistic characteristics on their optical properties.

The approach used here differs from the widely used implementations of the DDA method[22, 23] because it is based on the location of the atoms constituting the nanoparticles instead of on arbitrary chosen discretization volumes. This implies that the exact positions of the atoms inside the nanostructure and their atomic polarizability have to be known as input data of the calculations. But, it has the great advantage to give an exact route between these data and the optical characteristics of the nanoparticles considered. In other words, this method could be used to extract an atomistic information on such nanoparticles, from their optical characteristics.

These results clearly show that the chemical composition of the soot nanoparticle may have a sufficiently strong influence on the MAC curves to allow detection of chemical differences by using UV-visible spectroscopic measurements. However, MAC measurements could give information on the atomic details of the nanoparticles only if they are performed in a well-suited wavelength range, i.e., at wavelengths typically between 200 and 350 nm. In a more general way, the calculations show that MAC values as well as differences between MAC curves corresponding to different nanoparticles may

strongly vary with wavelength. In that sense, measurements at a given wavelength only is certainly not representative of the whole curves and thus should be considered with caution.

I have also compared the results obtained using the PDI approach to those deduced from classical macroscopic eletromagnetic theory. Significant differences have been evidenced between the PDI and analytical approaches as soon as defects are introduced in the atomistic structure of the primary nanoparticles of soot, that thus cannot be considered simply as homogeneous spherical particles.

Moreover, soot is made of aggregates rather than of isolated primary nanoparticles and, from an experimental point of view, the measured optical properties could also depend on the size, shape and fractal dimension of these aggregates. In addition, not only absorption but also extinction properties could be used to get more information on the characteristics of soot. Indeed, it has been recently shown, on the basis of comparison between experimental measurements and T-matrix calculations, that mass extinction cross sections (MEC) are much more sensitive to aggregate morphology than MAC measurements[69] although this conclusion is quite controversial because it appears contrary to recent modeling studies where both MAC and MEC displayed morphology dependence[68]. Using some additional approximations in the PDI model, the electric permittivities of soot aggregates were calculated, few years ago at Besançon, showing that the dominant effect governing permittivity variations with energy is the chemical composition of the primary particles rather than the fractal dimension of the aggregate[15]. The translation of this conclusion in terms of absorption and extinction properties of soot aggregates certainly deserves detailed investigations, in connection with the controversy mentioned above[68, 69]. Calculations of MAC and MEC curves for aggregates of primary particles are thus mandatory and will thus be one of the main immediate perspective of my PhD work.

It is worth mentioning that carbonaceous particles in the Troposphere can be rapidly surrounded by other species, especially water molecules, after their emission. Provided that the dynamic polarizability tensors of the adsorbed atoms/molecules are known, the PDI method presented here could be easily used to quantify the influence of aging on the soot optical characteristics.

Finally, I have also shown that polarizability values coming from graphite data can be satisfactorily used to calculate the extinction/absorption properties of large PAH molecules such as those encountered in the interstellar medium. Moreover, the results of the astrochemical model developped by J. Montillaud has been proved to be almost the same when including the cross sections issued from the PDI approach rather than those calculated by

more sophisticated TD-DFT methods. Thus, our PDI approach can interestingly complement quantum approaches for providing the astrochemical community with UV absorption cross sections of large PAHs, especially when considering those that are not yet included in the astronomical databases.

Bibliography

[1] Bohren CF, Huffman DR. Absorption and scattering of light by small particles. 1983. John Wiley and Sons, New York.

[2] Chung, SH, Seinfeld JH. Global Distribution and Climate Forcing of Carbonaceous Aerosols. J Geophys Res 2002;107:4407.

[3] Haywood J, Boucher O. Estimates of the direct and indirect radiative forcing due to tropospheric aerosols. A review. Rev Geophys 2000;38:513-43.

[4] Lohmann U, Feichter J. Global indirect aerosol effects: a review. Atmos Chem Phys 2005;5:715–37.

[5] Fuzzi S, Andreae MO, Huebert BJ, Kulmala M, Bond TC, Boy M, Doherty SJ, Guenther A, Kanakidou M, Kawamura K, Kerminen VM, Lohmann U, Russell LM, Pöschl U. Critical assessment of the current state of scientific knowledge, terminology, and research needs concerning the role of organic aerosols in the atmosphere, climate, and global change. Atmos Chem Phys 2006;6:2017–38.

[6] Chen Y, Penner JE. Uncertainty Analysis for Estimates of the First Indirect Aerosol Effect. Atmos Chem Phys 2005;5:2935-48.

[7] Combustion Generated Fine Carbonaceous Particles. Bockhorn H, D'Anna A, Sarofim AF, Wang H, editors. Karlsruhe: KIT Scientific Publishing; 2009.

[8] Demirdjian B, Ferry D, Suzanne J, Popovicheva OB, Persiantseva NM, Shonija NK. Heterogeneities in the Microstructure and Composition of Aircraft Engine Combustor Soot: Impact on the Water Uptake. J Atmos Chem 2007;56:83-103.

[9] Violi A. Modeling of Soot Particle Inception in Aromatic and Aliphatic Premixed Flames. Combust Flame 2004;139:279-87.

[10] Moulin F, Picaud S, Hoang PNM, Partay L, Jedlovszky P. A grand canonical Monte Carlo simulation study of water adsorption on a model soot particle. Mol Sim 2006;32:487-493.

[11] Moulin F, Picaud S, Hoang PNM, Partay LB, Jedlovszky P. A Grand Canonical Monte Carlo simulation of the aggregation of water molecules on chemically modified soot particles. Comp Lett 2008;4:105-16.

[12] Oubal M, Picaud S, Rayez MT, Rayez JC. Water adsorption on oxidized single atomic vacancies present at the surface of small carbonaceous nanoparticles modeling soot. Chem Phys Chem 2010;11:4088-96.

[13] Hantal G, Picaud S, Hoang PNM, Voloshin VP, Medvedev NN, Jedlovszky P. Water adsorption isotherms on porous onion-like carbonaceous particles. Simulations with the Grand Canonical Monte Carlo method. J Chem Phys 2010;133:144702.

[14] Moulin F, Devel M, Picaud S. Optical properties of soot nanoparticles. J. Quant. Spectrosc. Radiat. Transfer 2008;109:1791-1801.

[15] Langlet R, Vanacharla MR, Picaud S, Devel M. Bottum-up multi-step approach to study the relations between the structure and the optical properties of carbon soot nanoparticles. J. Quant. Spectrosc. Radiat. Transfer 2009;110:1615-27.

[16] Sorensen CM. Light scattering by fractal aggregates: A review. Aerosol Sci Technol 2001;35:648-87.

[17] Bond TC, Bergstrom R. Light absorption by carbonaceous particles: an investigative review. Aerosol Sci Technol 2006;40:27-67.

[18] Mie G. Beiträge zur Optik Trüber Medien, Speziell Kolloidaler Metallösungen. Annalen der Physik 1908;25:377-445.

[19] Keller D, Bustamante C. Theory of the interaction of light with large inhomogeneous molecular aggregates. I. Absorption. J Chem Phys 1986;84:2961-71.

[20] Michel B, Henning Th, Jäger, Kreibig U. Optical extinction by spherical carbonaceous particles. Carbon 1999;37:391-400.

[21] Michel B. Statistical method to calculate extinction by small irregularly shaped particles. J Opt Soc Am 1995;12:2471-81.

[22] Purcell EM, Pennypacker CR. Scattering and Absorption of Light by Nonspherical Dielectric Grains. Astrophys J 1973;186:705-14.

[23] Draine BT. The Discrete-Dipole Approximation and its Application to Interstellar Graphite Grains. Astrophys J 1988;333:848-72.

[24] Draine BT, Flatau PJ. Discrete dipole approximation for scattering calculations. J Opt Soc Am A 1994;11:1491-99.

[25] Mishchenko MI, Travis LD, Mackowski DW. T-matrix computations of light scattering by nonspherical particles: A review. J Quant Spectrosc Radiat Transfer 1996;55:535-75.

[26] Applequist J, Carl JR, Fung K-K. An Atom-Dipole Interaction Model for Molecular Polarizability, Application to Polyatomic Molecules and Determination of Atom Polarizabilities. J Am Chem Soc 1972;94:2952-60.

[27] McDonald J, Golden A, Jennings G. OpenDDA: a novel high-performance computational framework for the discrete dipole approximation. Int J High Perf Comp Appl 2009;23: 42–61

[28] Yurkin MA, Hoekstra AG. The discrete-dipole-approximation code ADDA: capabilities and known limitations. J. Quant. Spectrosc. Radiat. Transfer 2011;112: 2234–47.

[29] Choliy VY. The discrete dipole approximation code DDscat.C++: features, limitations and plans. Adv Astron Space Phys 2013;3:66–70.

[30] Jensen L, Åstrand PO, Mikkelsen KV. An Atomic Capacitance–Polarizability Model for the Calculation of Molecular Dipole Moments and Polarizabilities. International Journal of Quantum Chemistry. 2001;84:513–522.

[31] Malloci G, Joblin C, Mulas G. On-line database of the spectral properties of polycyclic aromatic hydrocarbons. Chemical Physics. 2007;332:353–359.

[32] Draine BT. Tabulated optical properties of graphite and silicate grains. The Astrophysical Journal Supplement Series. 1985;57:587-594.

[33] Devel M, Girard C, Joachim C. Computation of electrostatic fields in low-symmetry systems: application to STM configurations. Phys Rev B 1996;53:13159-68.

[34] Langlet L, Devel M, Lambin, Ph. Computation of the static polarizabilities of multi-wall carbon nanotubes and fullerites using a Gaussian regularized point dipole interaction model. Carbon 2006;44:2883-2895.

[35] Thole BT. Molecular Polarizabilities Calculated with a Modified Dipole Interaction. Chem. Phys. 1981;59:341-350.

[36] Mahanty J, Ninham BW. Dispersion forces, Academic Press (1976)

[37] Mayer A, Lambin P, Langlet R. Charge-dipole model to compute the polarization of fullerenes. Appl. Phys. lett. 2006;89:063117

[38] Senet P, Henrard L, Lambin P, Lucas AA. A one parameter model of the UV spectra of carbon. In: Kuzmany H, Fink J, Lehring M, Roth S, editors. Proceedings of the international winterschool on electronic properties of novel materials. Progress in fullerene research, vol. 393. Singapore: World Scientific; 1994.

[39] Andersen J, Bonderup E. Classical dielectric models of fullerenes and estimation of heat radiation. Eur Phys J D 2000;11:435-48.

[40] Draine BT, Lee HM. Optical properties of interstellar graphite and silicate grains. Astrophys J 1984;285:89-108.

[41] Laor A, Draine BT. Spectroscopic constraints on the properties of dust in active galactic nuclei. Astrophys J 1993;402:441-68.

[42] Draine BT. Scattering by interstellar dust grains. II. X-rays. Astrophys J 2003;598:1026-37.

[43] Djurisik A, Li EH. Optical properties of graphite. J Appl Phys 1999;85:7404-10.

[44] Mossotti, O. F. (1850). Mem. di mathem. e fisica in Modena. 24 11. p. 49.

[45] Clausius, R. (1879). Die mechanische Ugrmetheorie. 2. p. 62.

[46] Sohmen E, Fink J, Krätschmer W. Electron energy-loss spectroscopy studies on C_{60} and C_{70} fullerite. Z Phys B - Condensed Matter 1992;86:87-92.

[47] Kuzuo R, Terauchi M, Tanaka M, Saito Y, Shinohara H. Electron-energy-loss spectra of crystallite C_{84}. Phys Rev B 1994;49:5054-57.

[48] Saito S, Oshiyama A. Cohesive Mechanism and Energy Bands of Solid C_{60}. Phys Rev Lett 1991;66:2637-40.

[49] Smith AL. Comparison of the ultraviolet absorption cross section of C_{60} buckminsterfulleren in the gas phase and in hexane solutions. J Phys B 1996;29:4975-80.

[50] Berkowitz J. Sum rules and the photoabsorption cross sections of C_{60}. J Chem Phys 1999;111:1446-53.

[51] Iglesias-Groth S. Fullerenes and buckyonions in the interstellar medium. Astrophys J 2004;608:L37-L40.

[52] Mayer A, Lambin Ph, AAstrand PO. An electrostatic interaction model for frequency-dependent polarizability: methodology and applications to hydrocarbons and fullerenes. Nanotechnology 2008;19:025203.

[53] Andreae MO, Gelencsér A. Black carbon or brown carbon? The nature of light-absorbing carbonaceous aerosols. Atmos Chem Phys 2006;6:3131-48.

[54] Shaddix CR, Williams TC. Soot structure and dimensionless extinction coefficient in diffusion flames: implications for index of refraction. In Bockhorn H, D'Anna A, Sarofim AF and Wang H, editors. Combustion Generated Fine Carbonaceous Particles. KIT Scientific Publishing; 2009: pp. 17-33.

[55] Stuart SJ, Tutein AB, Harrison JA. A reactive potential for hydrocarbons with intermolecular interactions. J Chem Phys 2000;112:6472-6486.

[56] P. R. C. Kent, M. D. Towler, R. J. Needs, and G. Rajagopal. Carbon clusters near the crossover to fullerene stability. Phys. Rev. B 62, pag 15394, 2000.

[57] Boersma et al., Astrophysical Journal Supplement Series, 211:8 (12pp), 2014.

[58] G. Malloci, C. Joblin, G. Mulas. On-line database of the spectral properties of polycyclic aromatic hydrocarbons, Chem. Phys. 332, 353-359 (2007)

[59] W. W. Duley,S. Seahra. Graphite, Polycyclic Aromatic Hydrocarbons, and the 2175 Åextinction feature.The Astrophysical Journal, November 10; 507 : 874-888, 1998.

[60] W. W. Duley. A plasmon resonance in dehidrogenated coronene (C24Hx) and its cationsand the origin of the interestellar axtintion band at 217.5 nm.The Astrophysical Journal, March 10, 639:L59–L62, 2006.

[61] J. Montillaud, C. Joblin, and D. Toublanc.Evolution of polycyclic aromatic hydrocarbons in photodissociation regions Hydrogenation and charge states. Astronomy and Astrophysics. 552, A15, 2013.

[62] Grieco WJ, Howard JB, Rainey LC, Van der Sande JB. Fullerenic carbon in combustion-generated soot. Carbon 2000;38:597-614.

[63] de Heer WA, Ugarte D. Carbon onions produced by heat treatment of carbon soot and their relation to the 217.5 nm interstellar absorption feature. Chem Phys Lett 1993;207:480-86.

[64] Banhart F, Ajayan PM. Carbon onions as nanoscopic pressure cells for diamond formation. Nature 1996;382:433-35.

[65] Popovicheva OB, Persiantseva NM, Kuznetsov BV, Rakhmanova TA, Shonija NK, Suzanne J, Ferry D. Microstructure and water absorbability of aircraft combustor soots and kerosene flame soots: toward an aircraft-generated soot laboratory surrogate. J Phys Chem A 2003;107:10046-54.

[66] Henrard L, Lucas A, Lambin P. On the 2175 Å absorption band of hollow onion-like carbon particles. Astrophys J 1993;406:92-96.

[67] Liu L, Mishchenko MI, Arnott WP. A study of radiative properties of fractal soot aggregates using the superposition T-matrix method. J Quant Spectrosc Radiat Transfer 2008;109:2656-63.

[68] Scarnato BV, Vahidinia S, Richard DT, Kirchstetter TW. Effects of internal mixing and aggregate morphology on optical properties of black carbon using a discrete dipole approximation model. Atmos Chem Phys 2013;13:5089-101.

[69] Radney JG, You R, Ma X, Conny J, Hodges JT, Zachariah MR, Zangmeister CD. Dependence of Soot Optical Properties on Particle Morphology: Measurements and Model Comparisons. Environ Sci Technol 2014;48:3169-76.

[70] Prasanna S, Rivière Ph, Soufiani A. Effect of fractal parameters on absorption properties of soot in the infrared region. J Quant Spectrosc Radiat Transfer 2014;148:141-55.

Chapter 6

Conclusions and perspectives

In this thesis, I have presented a series of theoretical studies aiming at characterizing, at a molecular level, chemical and optical properties of soot model nanoparticles which are abundant in the atmosphere and which represent a major source of uncertainties in the current climate models.

The *in situ* study of these soot particles are particularly complex, leaving the laboratory studies as a necessary step to understand the phenomena involved in the influence of soot on the atmosphere. In particular, modeling the soot particles and their interactions with surrounding molecules represents an essential path to improve our knowledge on these systems. Modeling soot also relates to their optical response before and after ageing in the atmosphere.

Thus, in a first steep, I simulated reactivity processes between various carbonaceous surfaces and some chemical species present in the atmosphere by using different levels of theory (*ab initio*, DFT, and semi-empirical methods) and by using the commercial computational chemistry code Gaussian09. The aim of this first part of my work was to complement information previously obtained on the ageing of soot in contact with atmospheric oxidants by considering here the interaction with the nitrated and chlorinated species that are also present in various environments, such as, for instance, fire emissions. This work was carried out in the framework of a collaborative project developed with Prof. Jean-Claude Rayez and Dr. Marie-Thérèse Rayez of the Molecular Science Institute of Bordeaux.

Then, because of the importance of the atmospheric species depletion by adsorption on carbonaceous surfaces, my first work was focused on the interaction between NO and HCl with carbonaceous clusters (C_nH_m) modeling the surfaces that are likely present in soot nanoparticles. Differents

quantum approaches were thus used to investigate the NO-C_nH_m and HCl-C_nH_m systems showing that the interaction energy of these molecules is quite small, equal to a few kJ/mol (calculated at 0 K), and corresponds to a physisorption process. As a consequence, these species would not be efficiently trapped on such perfect surfaces in atmospheric conditions. However, the situation is completely different when a dangling bond is created at the surface by leaving an unsaturated C atom at the edge of the carbonaceous cluster or when there is a carbon monovacancy site in this cluster. Indeed, in this situation, the results of my calculations evidenced a strong interaction between the adsorbed species and the surface, leading to a chemisorption process and the possible dissociation of the adsorbed molecule. Such a situation is likely occurring in real soot nanoparticles, and the corresponding defect sites formed, for instance, during the recombination of soot precursors, are thus expected to be efficient trapping sites for different molecules in the troposphere.

Then, I determined the optical properties of model soot nanoparticles by using the Point Dipole Interaction (PDI) method based on an atomistic description of the target. The corresponding numerical simulations were conducted by using the Polarscat code developed by Prof. Michel Devel in Besançon (FEMTO-st Institute). In the framework of this second axis of research, my results clearly show that polarizability values coming from graphite data can be satisfactorily used to calculate the optical properties of round-shaped carbonaceous structures such as fullerenes and carbon bucky-onions. Also, my PhD work shows that chemical composition of the soot nanoparticle may have a sufficiently strong influence on the MAC curves to allow detection of chemical differences on soot by using UV-visible spectroscopic measurements. However, MAC measurements could give information on the atomic details of the nanoparticles only if they are performed in a well-suited wavelength range, i.e., at wavelengths typically between 200 and 350 nm. In addition, significant differences have been evidenced between the PDI and analytical approaches as soon as defects are introduced in the atomistic structure of the primary nanoparticles of soot, that thus cannot be considered simply as homogeneous spherical particles as in many atmospheric models. On the basis of the examples of nanoparticles simulated in this work, we may infer that spectroscopic signals strongly depend on the details of the atomistic structure of the nanoparticles investigated, at least in a suitable range of wavelengths. Then, it appears mandatory to take into account an atomistic description of these nanoparticles when calculating their electromagnetic properties, as it is done in the PDI method used in Besançon. Such a theoretical approach, coupled to experimental investigations, could thus be very useful to better characterize the morphological details of the primary soot nanoparticles.

Finally, I have also shown that the polarizability values coming from graphite data can be satisfactorily used to calculate the extinction/absorption properties of large PAH molecules such as those encountered in the interstellar medium. Moreover, the results of the astrochemical model developed by J. Montillaud has been proved to be almost the same when including the cross sections issued from the PDI approach instead of those calculated by more sophisticated TD-DFT methods. Thus, our PDI approach can also interestingly complement quantum approaches for providing the astrochemical community with UV absorption cross sections of large PAHs, especially when considering those that are not yet included in the astronomical databases.

In the literature, there is a series of papers devoted to the study of the effect of surface roughness on the scattering of wavelength-scale particles. For instance, Li et al. [1] applied a finite-difference time-domain (FDTD) method for spheres with surface roughness in a form of positive and negative Gaussian spikes, whereas Nousiainen et al. [2] used the DDA method for similar systems. In addition, Zubko et al. [3] used DDA to study the dependence of scattered intensity and linear polarization on a shallow layer of surface roughness on irregular, wavelength-scale Gaussian particles. Nevertheless, none of these methods takes into account the exact positions of the atoms in the system under consideration. Thus, among the perspectives of this work, the most immediate seems to take advantage of the fact that PDI method do not make any approximation on the particle shape (because it considers the exact atomic positions) to investigate the impact of surface roughness on scattering properties of different primary soot nanoparticles. It should be noted, that in the last $15th$ Electromagnetic and Light Scattering Conference, a series of contributions on this topics pointed out the importance of developing research works in this direction.

Similarly, the Polarscat code allows the calculations of the phase angles and of the polarization degrees. This information could be very useful to discriminate between different nanoparticles morphologies and it is often used in experiments for *in situ* characterization. However, preliminary numerical tests have shown that the present version of our code is strongly limited with respect to the size of the nanoparticles that can be considered. Indeed, because of the atomistic description, the computational time is very high and it appears that only a few thousands of atoms can be reasonably included in the present calculations. This corresponds typically to particles of size less than 5 nm. Unfortunately, it seems that such very small particles are very difficult to characterize in laboratory experiments and discussions with J.B. Renard have been started on this topics, in the framework of a collaborative projet granted by the CNRS-LEFE program. To summarize, from the theoretical point of view, the perspective of my work will be to increase the size of the particles that can be considered (certainly by modifying the

corresponding algorithms), whereas from the experimental point of view, it is to decrease their size !

As mentioned in the chapter dedicated to the optical properties of soot nanoparticles, recent experimental measurements and T-matrix calculations [4] have shown, that only the mass extinction cross sections (MEC) presents sensitivity to the aggregate morphology. Nevertheless, this conclusion is quite controversial because it appears contrary to other recent modeling studies [5] where both MAC and MEC displayed morphology dependence. Then, even if our PDI method have some constraint with respect to the simulation of large particules, we are confident in its possible extension to larger systems like the soot aggregates. Indeed, some modifications of the Polarscat code have been already tested in the preliminary work of Langlet et al [6] devoted to the calculation of the polarizability of aggregates of S_{units} primary particles. The next step will be now to modify this code to solve the scattering problem. Nevertheless, because our PDI method is a DDA based code, we do not expect significant differences with respect to the previously published results using DDA, mainly because the absorption properties are suspected to depend on the structure of the primary particles and not on the morphology of the aggregates. Anyway, as mentioned before, other experimental observables like the polarization degree and the phase angles could be used to discriminate between different nanoparticles morphologies and thus, developing the PDI method for the corresponding calculations would be very useful.

Finally, it is important to recall here that one of the initial goal of this PhD was to characterize the effect of ageing on the electromagnetic properties of soot primary particles. It is thus important to modify our models of primary soot nanoparticles by including chemical elements other than C that are issued from various adsorption processes. However, in the framework of the PDI approach, the complex dynamical polarizabilities of such atoms have to be known. Unfortunately, we are not aware of the availability of such parameteres in the literature, which means that they have to be calculated or fitted from experimental measurements, which is certainly not an easy task. From a theoretical point of view, various approaches can be undertaken on this way, mainly based on quantum chemistry calculations. However, when considering the oxygen atom which is certainly one of the most abundant species in soot besides C and H, the dynamical polarizability should not be calculated only for an isolated oxygen atom, but rather for an O atom included in various chemical groups that may be present on soot, such as hydroxyl, carbonyl, acid ... Moreover, both real and imaginary parts of the polarizability have to be computed. But, the Gaussian code for instance, only gives the real part of these polarizabilities, and although it

is always possible to recalculate the imaginary part by using the Kramers-Kronig relations, the calculations of the real part should be done on a very large (theoretically, infinite) range of frequencies which appears as a very tedious task. Moreover, even for simple molecules such as small PAHs, preliminary tests performed in collaboration with J.-C. Rayez and M.-T. Rayez evidenced some convergence problems in the calculations of polarizabilities with Gaussian, especially near resonances. Another possibility will be thus to use TD-DFT approaches, but again, such methods have to be tested on various types of oxygenated species before any inclusions of the results in our PDI code. Nonetheless, considering that all these polarizability parameters are known, simulation could be carried out to reproduce some experimental results, correlating the position of the absorption peaks with the amount of oxygen atoms adsorbed on the system.

Finally, as explained in Chapter 2, the knowledge of the optical index and of the electrical suceptibility is mandatory to make theoretical predictions on the influence of carbonaceous particles on the changes in the atmospheric radiative transfer. However, at the current state of the PDI code, the calculations of these variables requires the use of the Clausius Mossoti relation (see appendix B) to obtain the relative permititvity ϵ_r (or the optical index m), from the computed polarizability α for the studied system. For that reason, only symmetric systems like the previously described fcc crystal of C_{60} could be computed at present. For systems of arbitrary shape, the keypoint is in fact to find a theoretical solution for computing the macroscopic field of the soot nanoparticle, which cannot be approximated as the arithmetic average of the local fields felt by each atom as evidenced by preliminary tests performed in the last weeks of my PhD work.

Bibliography

[1] Li C, Kattawar GW, Yang P. Effects of surface roughness on light scattering by small particles. JQSRT 2004;89:123-31.

[2] Timo Nousiainen, Karri Muinonen. Surface-roughness effects on single-scattering properties of wavelength-scale particles. Journal of Quantitative Spectroscopy and Radiative Transfer 106 (2007) 389–397

[3] Zubko E, Muinonen K, Nousiainen T, Shkuratov Y, Videen G. Influence of surface roughness on scattering properties of wavelength-size particles simulating regolith grains. In: Vernadsky Institute-Brown University Microsymposium 42 on Comparative Planetology; Vernadsky Institute, Moscow, Russia, October 10–12, 2005. p. 2 contribution m42 71.

[4] Radney JG, You R, Ma X, Conny J, Hodges JT, Zachariah MR, Zangmeister CD. Dependence of Soot Optical Properties on Particle Morphology: Measurements and Model Comparisons. Environ Sci Technol 2014;48:3169-76.

[5] Scarnato BV, Vahidinia S, Richard DT, Kirchstetter TW. Effects of internal mixing and aggregate morphology on optical properties of black carbon using a discrete dipole approximation model. Atmos Chem Phys 2013;13:5089-101.

[6] Langlet R, Vanacharla MR, Picaud S, Devel M. Bottum-up multi-step approach to study the relations between the structure and the optical properties of carbon soot nanoparticles. J. Quant. Spectrosc. Radiat. Transfer 2009;110:1615-27.

Appendix A

Appendix A

As mentioned in section 4.4.2, an interesting question concerns the energy of the reactions: $C_{24}H_{12}$ + Cl and $C_{24}H_{11}$ + HCl when using the large basis set 6-311G^{++}(d,p) and the BHandHLYP functional. Then, for the σ and π final states of the product $C_{24}H_{12}Cl$, we saw that the surface reaction with HCl was more exoergic than that involving only Cl.

$C_{24}H_{12}$ + Cl = σ: -5.5 Kcal/mol	$C_{24}H_{12}$ + Cl = π : -7.1 Kcal/mol
$C_{24}H_{11}$ + HCl = σ:-22.0 Kcal/mol	$C_{24}H_{11}$ + HCl = π : -23.7 Kcal/mol

Then, let us try to interpret these energy differences comparing these results with experimental and theoretical data of the similar processes but involving benzene instead of coronene. The choice of this simple model is due to the disponibility of experimental values for this small cluster. In addition, like the chimisorbtion processes have a local character, the use of such a system seems not compromise the physical reality of the concerned phenomenon.

To do that, we will use thermodynamics tables coupled to a reliable theoretical evaluation of heats of formation from the AM1 method proposed by Dewar. The AM1 methodology as a reference for heat of formation at 298K is justified by the good quality generally provided for this kind of information. A situation somewhat natural since this semi-empirical approach has been built for this purpose. However, the following analyze will only consider the σ state because it was not possible to describe the C_6H_6Cl π structure with the AM1 methodology, by using only electron valence shell.

$\Delta H^0_{f,298}$	experimental (Kcal/mol)	AM1-ROHF(Kcal/mol)	AM1-ROHF 1/2 e (Kcal/mol)
H	52.1	-	-
Cl	28.99	-	-
HCl	-22.1	-24.6	-
C_6H_6	19.8	-22.0	-
C_6H_5	80.7	76.3	79.5
C_6H_6Cl	-	33.1	34.1

Table A.1: Required data to analyze the two reactions mentioned above and for the similar reactions involving benzene insteade of coronene (ROHF: Restricted open shell Hartree-Fock;ROHF 1/2 electron: ROHF minus the self repulsion of the two half electrons on the highest molecular orbital).

Indeed, the ΔE_{ads} were computed combining the experimental and theoretical (when there was not experimental data) values from table A.1 :

ΔE_{ads} = C_6H_6Cl + C_6H_6 + CL = -14.7 Kcal/mol
ΔE_{ads} = C_6H_6Cl + C_6H_5 + HCL = -24.5 Kcal/mol

Although the comparison is not inmediate since DFT provides results at 0K without any ZPE correction whereas AM1 and experimental values are enthalpies at 298K, for this simple model also remain an energy difference. Then, it is clear that reactions between C_nH_{m-1} + HCl are always more exoergic than C_nH_m + Cl, the difference liying around 10 Kcal/mol in average.

Appendix B

Appendix B

A cornerstone in any DDA code results from the choice of the polarizability values that are used to calculate the dipoles (physical and theoretical problem). Similarly, in the PDI approach, an atomic polarizability must be defined for each atomic dipole either from the complex refractive index $m = n + ik$; $m^2 = \epsilon$ or from fits of *ab initio* molecular polarizabilities.

In physics, the Clausius-Mossotti relation [1, 2] connects the relative permittivity ϵ_r of a dielectric (perfect, homogeneous and isotropic) material to the polarizability α of the atoms or molecules constituting the dielectric. The relative permittivity is a bulk (macroscopic) property and polarizability is a microscopic property of matter; hence this relation bridges the gap between a directly-observable macroscopic property and a microscopic molecular property.

It might be simply assumed that the field experienced by a dipole is just the average macroscopic electric field. However, at a microscopic level we would clearly expect the electric field to vary with position, so an actual dipole within the material may well experience a rather different electric field. Then, we should improve the model to get a more reliable connection between macroscopic measurements and microscopic models by taking into account the 'local field effects'.

We assume that the actual E-field seen by a dipole, i.e., its local field, $\vec{E}_{local}$ is given by the sum

$$\vec{E}_{local} = \vec{E}_{macro} + \vec{E}_{lor} + \vec{E}_{sph}, \tag{B.1}$$

where $\vec{E}_{macro}$ is the average macroscopic field, $\vec{E}_{lor}$ is the so-called "Lorentz" field due to polarization charge on the surface of a ficticious spherical cavity

within the material and centred on the considered dipole, and $\vec{E}_{sph}$ is the contribution from material inside the "removed" sphere but excluding the central dipole (on the assumption that the field of the central dipole does not act on itself).

Then, if the cavity is sufficiently large that there is a macroscopically smooth polarization charge density on its surface, the resultant field at the center can be straightforwardly evaluated and the results is:

$$\vec{E}_{lor} = \frac{\vec{P}}{3\epsilon_0}. \tag{B.2}$$

Furthermore, *for a cubic system* because of the high symmetry, all dipoles on opposite sides within the sphere can be paired off to give a net zero field at the center of the cavity $\vec{E}_{sph} = 0$ (see e.g. Kittel for a detailed argument) and thus:

$$\vec{E}_{local} = \vec{E}_{macro} + \frac{\vec{P}}{3\epsilon_0}. \tag{B.3}$$

Then, if we employ the standard form, $\vec{P} = \epsilon_0 \chi \vec{E}_{macro}$, the expression for the local field becomes

$$\vec{E}_{local} = \vec{E}_{macro} + \frac{\epsilon_0 \chi \vec{E}_{macro}}{3\epsilon_0} = \vec{E}_{macro}(1 + \frac{\chi}{3}), \tag{B.4}$$

where $\chi = \epsilon_r - 1$ is the electric susceptibility. As a consequence, we can write

$$\vec{E}_{local} = \frac{(\epsilon_r + 2)}{3} \vec{E}_{macro}. \tag{B.5}$$

Now, inserting this definition of $\vec{E}_{local}$ and the atomic polarizability α via $\vec{p} = \alpha \vec{E}_{loc}$ in

$$\vec{P} = \sum_i N_i \vec{p}_i = \sum_i N_i \alpha_i \vec{E}_{local} = \epsilon_0 \chi \vec{E}_{macro}, \tag{B.6}$$

where N_i represent the number of constituent elements n_i by volume unit, we end up with that is known as Clausius-Mossotti relationship between the material dielectric constant ϵ and the total polarizability α of its constituent:

$$\sum_i N_i \alpha_i = \frac{3\epsilon_0(\epsilon_r - 1)}{\epsilon_r + 2} \tag{B.7}$$

note that $1/N_i \approx 8,788\mathring{A}^3$ by atom for graphite and $1/N_i \approx 703,34\mathring{A}^3$ by molecule in a cubic face center (cfc) cristal of C_{60}. Furthemore, it should be mentioned that for the more complex anisotropic case, depolarization factors could be computed, as shown by P. Senet [3] and confirmed by Andersen and Bonderup for graphite [4].

Bibliography

[1] Mossotti, O. F. (1850). Mem. di mathem. e fisica in Modena. 24 11. p. 49.

[2] Clausius, R. (1879). Die mechanische Ugrmetheorie. 2. p. 62.

[3] Senet P, Henrard L, Lambin P, Lucas AA. A one parameter model of the UV spectra of carbon. In: Kuzmany H, Fink J, Lehring M, Roth S, editors. Proceedings of the international winterschool on electronic properties of novel materials. Progress in fullerene research, vol. 393. Singapore: World Scientific; 1994.

[4] Andersen J, Bonderup E. Classical dielectric models of fullerenes and estimation of heat radiation. Eur Phys J D **2000**, 11, 435-48.

Modélisation de la réponse optique des particules de suie émises dans la Troposphère

Ce travail concerne la modélisation, à l'échelle moléculaire, de l'interaction entre des nanoparticules carbonées et le rayonnement électromagnétique. Le but est d'aider à la compréhension des propriétés optiques des particules de suie afin de mieux quantifier l'influence des suies sur l'atmosphère et le climat. L'étude de l'interaction rayonnement/particules de suie fraîche a été effectuée par la méthode PDI ; il a été montré que : i) le coefficient d'absorption massique (MAC) des particules de suie dépend de la répartition des atomes dans la particule et de leurs liaisons, en particulier entre 200 et 350 nm ; ii) le MAC diffère selon que le cœur de la particule carbonée est occupé ou non par des plans graphitiques ; iii) un modèle analytique n'est pas adapté pour calculer le MAC d'une nanoparticule carbonée présentant des défauts structuraux. De plus, des méthodes de chimie quantique ont été utilisées pour caractériser le vieillissement des suies. Les résultats montrent que : i) NO, Cl, et HCl sont physisorbées sur une surface carbonée parfaite alors que sur une surface défective, ces espèces sont chimisorbées et conduisent à une modification de la surface ; ii) la présence de Cl conduit à un piégeage fort des molécules d'eau supérieur à celui obtenu lorsqu'un site oxygéné est présent sur la surface carbonée, expliquant ainsi le caractère hydrophile des suies émises lors d'incendies dans des milieux industriels. Enfin, la méthode PDI a été appliquée au calcul de la polarisabilité de HAP afin d'interpréter des spectres d'absorption des grains carbonés du milieu interstellaire, en incluant des molécules pour lesquelles aucune donnée n'était actuellement disponible.

Mots clés:

Suie, propriétés optiques à l'échelle nanométrique, coefficient d'absorption massique (MAC), PDI (Point Dipole Interaction), DDA (Discrete Dipole Approximation), Espèces chlorées, Adsorption, Modélisation

Modeling Optical Properties of Combustion Soot emitted in the Troposphere

This work concerns the modeling, at the molecular level, of the interaction between carbonaceous particles of nanometric size and the electromagnetic radiation. The goal is to improve our understanding of the optical properties of soot particles, to better quantify the influence of soot on the atmosphere and on climate change. The study of the interaction between radiation and fresh soot particles was carried out using the point dipole interaction method; it has been shown that: i) the mass absorption coefficient (MAC) of these soot nanoparticles may significantly depend on their atomistic details, especially between 200 and 350 nm; ii) the MAC depends on whether the heart of the carbonaceous particle is occupied or not by graphite planes; iii) an analytical model is not suitable for calculating the MAC of carbonaceous nanoparticles having structural defects. In addition, quantum chemical methods have been used to characterize the ageing of soot. The results obtained are i) NO, Cl, and HCl are physisorbed on a perfect carbonaceous surface whereas on a defective surface, these species are chemisorbed and lead to a modification of the surface; ii) on a carbonaceous surface, the presence of adsorbed Cl atoms leads to a strong trapping of the surrounding water molecules. This may be related to the highly hydrophilic nature of soot emitted during fires in industrial environments. Finally, the PDI method was applied to calculate the polarizability of PAHs to help at interpreting the absorption spectra of carbonaceous grains in the interstellar medium, including molecules for which no data was currently available.

Keywords:

Soot, Optical properties at the nanometer scale, Mass Absorption Coefficient (MAC), PDI (Point Dipole Interaction), DDA (Discrete Dipole Approximation), Chlorinated species, Adsorption, Modeling